Fe-N-C electrocatalysts from waste biomass for the oxygen reduction reaction

Doctoral Dissertation
Doctoral Program in Chemical Engineering (34th Cycle)

Fe-N-C electrocatalysts from waste biomass for the oxygen reduction reaction

By

Stefano Zago

****

Supervisor:
Prof. Stefania Specchia

Doctoral Examination Commitee:
Dr. V. Baglio, Referee, CNR-ITAE, Istituto di Tecnologie Avanzate per l'Energia "Nicola Giordano", Messina, Italy
Dr. A. Lavacchi, Referee, ICCOM-CNR, Sesto Fiorentino (FI), Italy
Prof. M. Piana, Referee, Institute of Technical Electrochemistry, Technische Universitat Munchen, Garching, Germany
Prof. A. D'Epifanio, Referee, Department of Chemical Science and Technologies, University of Rome Tor Vergata, Rome, Italy
Prof. M. Armandi, Referee, Dipartimento di Scienza Applicata e Tecnologia, Politecnico di Torino, Italy

Politecnico di Torino
2022

Declaration

I hereby declare that, the contents and organization of this dissertation constitute my own original work and does not compromise in any way the rights of third parties, including those relating to the security of personal data.

Stefano Zago

Torino, Gennaio 2022

* This dissertation is presented in partial fulfillment of the requirements for **Ph.D. degree** in the Graduate School of Politecnico di Torino (ScuDo).

I would like to dedicate this thesis to my loving family and all my friends

Abstract

Fuel cells are devices able to convert chemical energy from a redox reaction to electric energy with low pollutants emission. They are a green alternative to current power sources, as they can be powered with energy from renewable sources and have potential application in the field of electronic devices as well as transportation. Their marketability is limited because of the high cost of catalysts needed to make the reaction happen and their low durability. For this reason, research is going on in both understanding the mechanism of oxygen reduction reaction, which is quite sluggish and is currently the limiting step of the reaction, as well as developing new electrocatalysts that can satisfy the requirements in performances, costs, and durability.

This work involved the synthesis of PGM-free (Platinum group metal free) electrocatalysts, namely Fe-N-C, which make use of non-noble metals coordinated by nitrogen atoms and supported on conductive carbon structure. The purpose is getting close to the performance of commercial Pt electrocatalyst and even surpass them to some extent. For the supporting carbon scaffold, biomass derived biochar has been selected and further engineered by chemical treatments, in order to obtain high value materials from common waste and create thus a circular economy giving some sort of new life to normally discarded wastes. Specifically, the biomass chosen is commercial tea leaves, thermally and chemically treated while the iron functionality is introduced by ball milling for 90 minutes. The structures obtained, widely characterized, show the porous and graphitic structure of the carbon, as well as the presence of iron. Electrochemical tests confirm the activity, stability and durability of these materials. It’s clear that for ORR in alkaline environment, the biomass derived materials can outperform platinum in the long-term performance. The straightforward approach used for the synthesis is easy to replicate and scale up, and it is also possible to use it for other types of biomasses.

Graphical Abstract

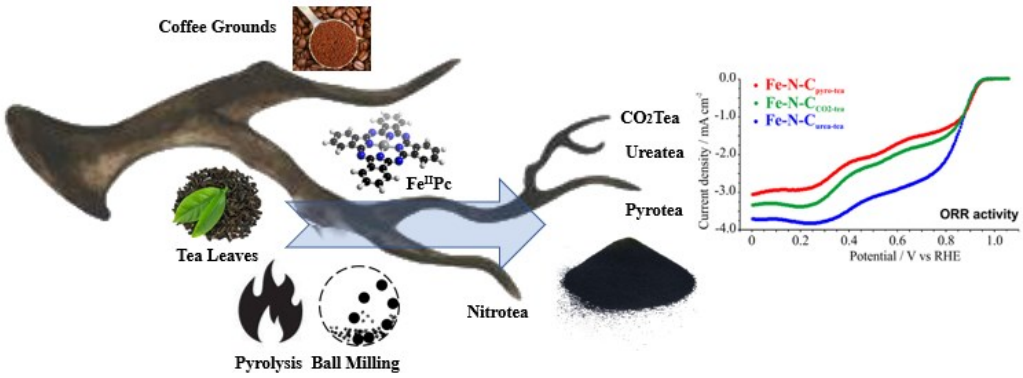

Contents

List of Figures

List of Tables

Chapter 1

Introduction on Fuel Cells

1.1 Generic Principles

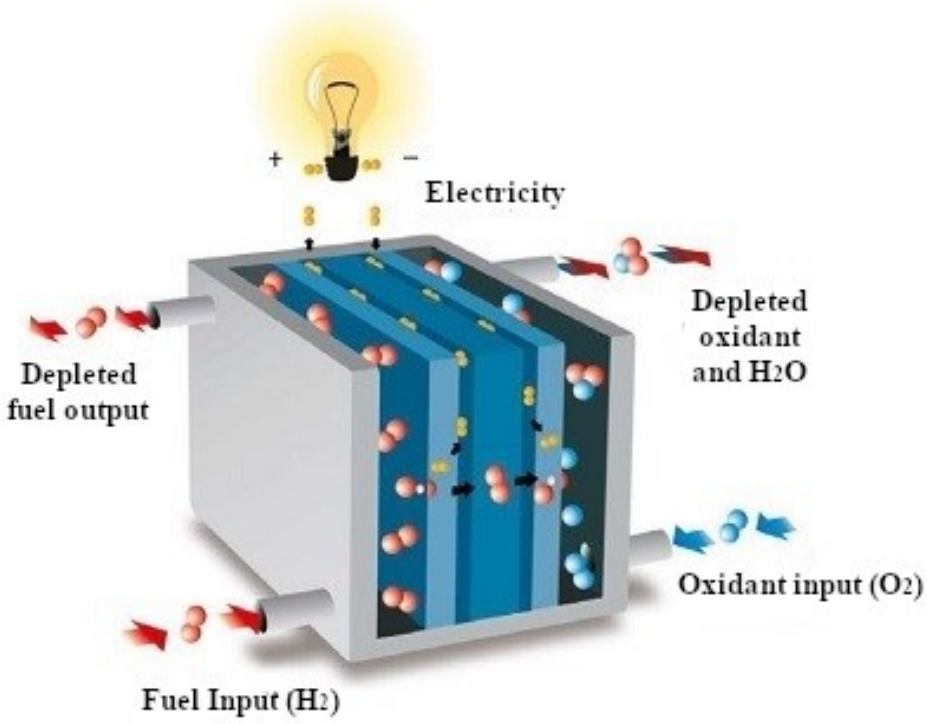

Figure 1: PEMFC working mechanism (Source: massflow-online.com)

A fuel cell is a electrochemical device able to convert chemical energy from a fuel, like hydrogen or different types of alcohols, to electrical energy thanks to a redox reaction.[1] Such devices are very promising for green energy production, in fact energy harvested in this way is clean because for hydrogen fuel cells there is basically no waste other than water, which can be freely released in the environment. Hydrogen is extremely versatile as a fuel, albeit caution needs to be exercised when handling it, and has the potential to power anything, ranging from small devices like electronics, up to automotive vehicles.[2] Historically speaking, between the first funding of fuel cells there was space application for NASA in projects such as Apollo and Gemini. It is interesting to note that in space a fuel cell can act as both energy provider and water generator. More recent developments are the extension of this technology to different devices, a very groundbreaking prospect is represented by hydrogen powered vehicles: cars but also buses, trains or ships, that are powered with a stack of fuel cells fed with hydrogen. Fuel cell technology is catching on in lots of countries, the main investors being Japan, Canada, USA and Germany. Of course having such a wide market available with lots of competitor, it is important to set targets and benchmarks. [3]

Figure 2: Hydrogen powered car. (Source: nrel.gov)

Fuel cells offer a more efficient and sustainable alternative to internal combustion engines as a means of harnessing energy. With the ongoing developments in renewable energy production and the hydrogen economy, the demand for fuel cells could see a large rise in the near future. Various applications have been proposed for fuel cells and the results are already being observed in the automotive industry due to their remarkable efficiency, low-temperature operation and fast fuelling times. However, one of the major drawbacks to the technoeconomic viability of fuel cells is their large capital costs. Catalysts account for almost half of the total fuel cell stack production costs primarily due to the need for precious metal electrocatalysts such as platinum to achieve good ORR activities.

The U.S. Department of Energy set for PEMFC the 2020 target of 300 A cm^{-3} at a voltage of 0.8 V for PGM-free electrocatalysts in membrane electrode assembly (MEA) testing. However, PGM-free catalysts will eventually need to meet the standards and targets set for platinum catalysts across all categories such as ORR activity and durability in order to be considered industrially viable. While RDE testing is an effective way to screen electrocatalysts and investigate their electrochemical properties, MEA testing is integral to truly determine the feasibility of electrocatalyst materials

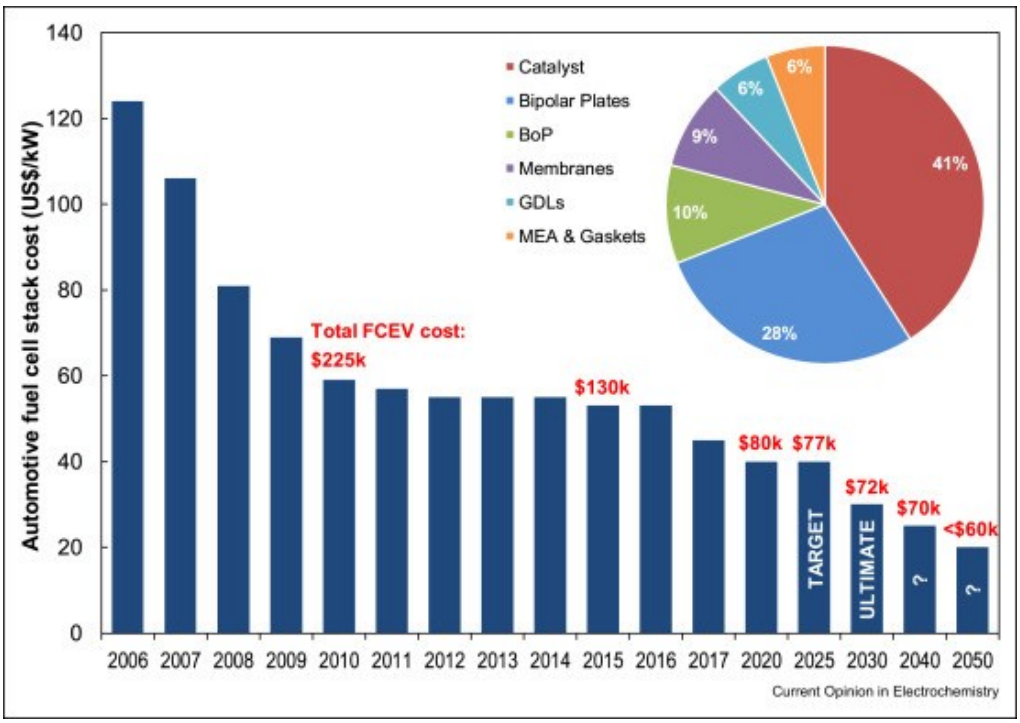

Figure 3: Evolution of cost of Fuel Cell Electric Vehicles and set targets for next decades.[2]

In order to make the reaction available and achieve an efficient conversion of energy, catalysts are needed. At the moment commercial catalysts make use of platinum supported on carbon conductive material, although this type of catalyst needs to be reduced for a lot of reasons.

A fuel cell is built out of a MEA (membrane electrode assembly) which include both the electrodes – anode and cathode - the solid electrolyte and the gas diffusion layers. and their construction is extremely compact. However, the high cost of the

electrocatalyst is still one of the main drawbacks as well as the difficulty to find a suitable membrane except for Nafion (which can be used only in PEMFC).

1.2 The Platinum problem

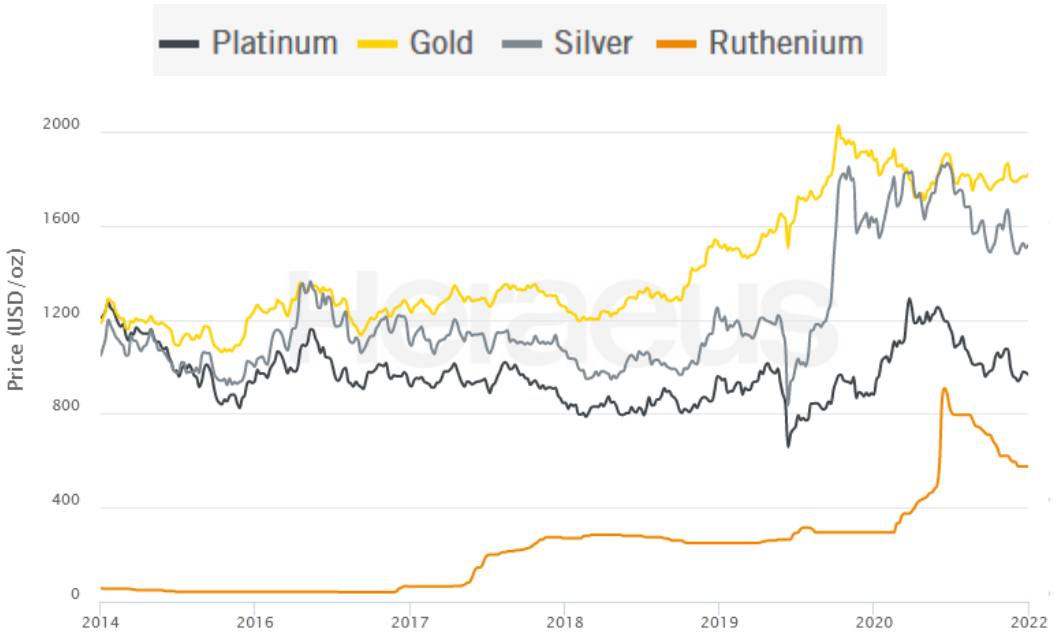

Figure 4: Price variation of Platinum, Gold, Silver, Ruthenium from 2015 to 2022. Source: heraeus.com

Platinum is the most common electrocatalyst for ORR reactions, because as a noble metal, it guarantees enhanced performance and high energy output, although it faces a number of big problems that needs to be addressed in future studies.[4] First of all, in strictly economical terms, platinum is expensive: it's quoted in the stock exchange market, like gold or silver, and in general it has a very high cost per units of energy produced, therefore different studies have the purpose of diminish the loading of platinum in the catalyst (usually at the cost of lower performance) in order to make the technology affordable for large scale application. There is also a political problem: platinum is available only in a few countries that could control the market in case fuel cells became the most used energy devices. In the case of Russia, this is undesired as it's already a very strong and powerful country and it's known for their leadership in natural gas. Other countries, such as South Africa and Zimbabwe, are more likely to not retain the leadership for themselves but get

manipulated by third parties, leading to a scenario not easy to predict but surely not pleasant to live in. Other than the monopoly problem, there is also the human condition of workers that are not protected by the laws in certain countries.

The tolerance for methanol or other alcohols is very low, meaning that a small amount of fuel reaching the catalyst layer can hinder its performance. In general, Pt electrocatalysts tend to suffer loss of catalytic activity over time, leading to loss of performance in a fuel cell. This is attributed to different phenomena, first of all the particle aggregation that decreases the electrochemical accessible surface area over time. There is also the easy poisoning, both carbon monoxide and alcohols can lead to loss of activity or selectivity when they are able to reach the catalyst; for this reason it's important to develop electrocatalyst that can endure both repetitive cycling but also avoid poisoning from such species. Also repeated cycling and prolonged usage are detrimental, because of corrosion of Pt particles which become covered with oxide and lose in performance unless it is regenerated. Of course, regeneration implies an even higher cost.

Many of strategies have been developed in this sense, for example alloying Pt with other metals, or fine control of particle size and distribution to obtain electrocatalysts with higher electrochemically surface area (ECSA) [5]

For all of these reasons, it's important for any researcher approaching the fuel cell technology to know that at the moment the most common trend of research is solving these problems, engineering electrocatalyst with very low loading of platinum without a big loss in performance, or either catalyst without platinum or other noble metals. The last category of electrocatalysts goes by the name of PGM-free as well as non-noble and will be the object of this thesis. They will be analyzed in detail in the next paragraphs but it's worth noting they mainly take advantage of transition metals like iron or cobalt and are able to reach similar value of performance to Pt catalyst in alkaline environment and sometimes even in acidic environment.

1.3 AEMFC and DMFC

The focus of this work is on Anion exchange membrane fuel cells (AEMFC), the viability of which has grown in recent years due to the development of highly conductive membranes which can facilitate anion exchange. AEMFC are a particular type of cells working in alkaline environment. The change of pH brings

a change in the mechanism, analyzed by different research groups, and leads to the possibility of running the ORR reaction at the cathode without the need of noble metals like platinum. Therefore, it is possible to replace precious catalyst with transition metals like iron, cobalt, or other metals.

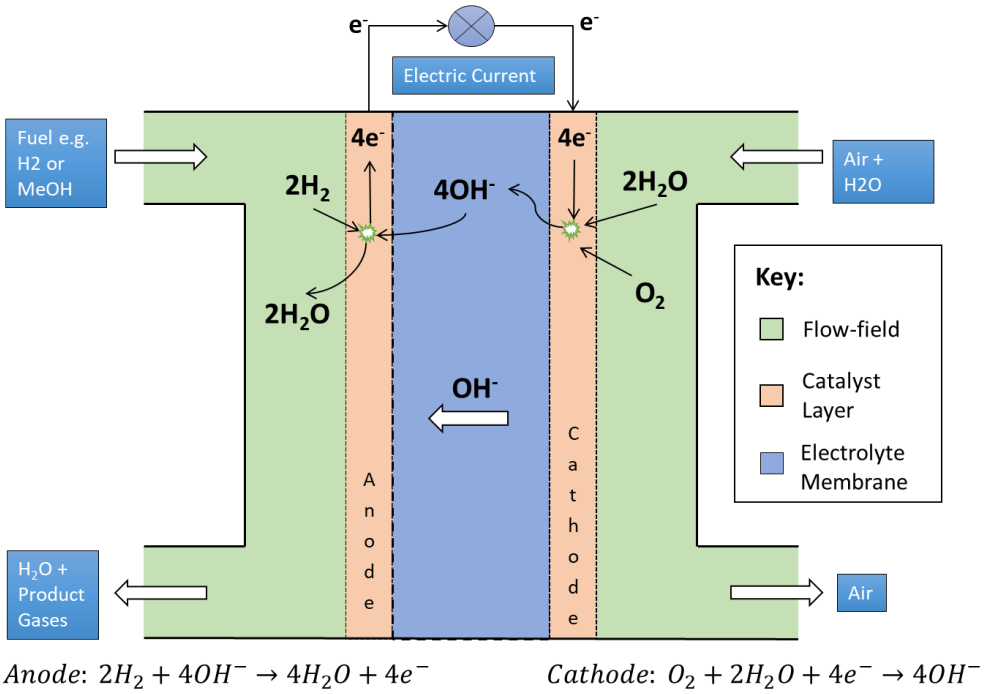

Figure 5: Schematic Mechanism of AEMFC.

These are gaining attention nowadays because of the low cost and different mechanism involved in the catalysis, leading to the research of different properties of the support, for example the pore distribution which affects the mass transport. In alkaline operating conditions, usually the electrocatalyst is more durable as well as less costly, meaning there is the potential of overcoming two of the main drawbacks of PEMFCs and noble metal electrocatalysts. The two technologies share some similarities such as the geometry of the stack and the main reaction product of water, but the reaction differs in each case. Figure 5 shows the anodic and cathodic reactions as they take place in an AEMFC: *at the anode,* fuel (typically an alcohol or H_2) is supplied and undergoes oxidation to produce water and electrons which flow through an external circuit to produce electrical work; if

the fuel is an alcohol CO_2 is also produced which is problematic not only because it's not desirable for the environment but also leads to the formation of an acidic product and therefore, more alkaline electrolyte has to be fed to maintain pH ; *at the cathode,* oxygen undergoes reduction with water at the catalyst layer to produce OH^- ions which migrate through the electrolyte membrane to complete the circuit[6]

Their distinct advantages include increased activity of non-noble catalysts for the ORR and a less aggressive environment when compared with Proton Exchange Membrane Fuel Cells (PEMFCs). The alkaline medium also displays enhanced alcohol oxidation reaction kinetics, making this type of device convenient for fuels different than hydrogen. On the other side, if using hydrogen as a fuel the activity loss at the anode is consistent (two orders of magnitude) and this leads to need of noble metals like Pt or Pd.

As a result of the enhanced kinetics regarding ORR for non-noble materials, there has been much research into the development of PGM-free electrocatalysts in alkaline conditions. Various catalysts have been investigated such as tungsten carbide, transition metal oxides and metal-organic frameworks. By far the most effective electrocatalysts which have been documented in the literature are composed of transition metals bond to nitrogen on a carbon support (M-N-C). Still, developing a good electrocatalyst for applications in AEMFCs is not easy as there are a number of required properties to consider. The high activity towards ORR is the obvious main requirement and in order to fulfill that, evaluation of the mechanism is needed, especially to favor the $4e^-$ transfer mechanism which is preferred. It is also important to have a porous carbon structure to minimize mass transport limitation and this usually is related to the specific surface area of the support. A porous structure has two advantages: first the electrochemically accessible area is expected to be higher, and this would help the catalyst to convert most of the fuel injected; second, a higher specific surface area also permits a reduced catalyst layer thickness which results in lower resistances. Also porosity is desired (usually it came with high surface area but it's not guaranteed) because of water management: for fuel cell stack performance high porosity arising from mesopores (as opposed to micropores) is preferred to avoid flooding.[7] These considerations will be discussed in more detail in the following section.

Direct methanol fuel cells (DMFC) is a primary subject of fuel cell research for portable applications, and many researchers showed it's an interesting alternative to recheargeable battery technology as well as PEM fuel cells.[8,9] The main feature is the use of a liquid fuel, namely methanol (although similar setups can be used for

ethanol, hydrazine, or other liquid fuels). Nowadays for most lithium-based devices, the major source of power is a rechargeable battery, but this presents a disadvantage as batteries need an external electrical power source in order to charge, meaning there is a strong limit to the portability of the device that requires an existing electrical source, and shows limited battery capacity. This is particularly relevant in remote area where no electric power grid is available, making extremely problematic to run a device on portable batteries. Nonetheless, there is an issue regarding the production of electricity since most power plants still make use of fossil fuel, not very environmentally friendly. The disadvantages of rechargeable batteries lead many research groups to seek alternative power sources, demonstrating the possibilities of DMFCs as a suitable power source for portable energy applications. Among their advantages, DMFCs can operate at low working temperatures, have no need to recharge with electricity, have a fast refueling system and are usually designed for longer cell lifetime, and make use of methanol which is considered a renewable and environmentally friendly source of energy: even if CO_2 is produced in the combustion process, the overall well-to-wheel emission level (meaning the total production of CO_2 involving stocking transport and usage) is among the lowest available. Making use of a liquid fuel, DMFC also benefits of higher energy density compared to Li-ion batteries and gas fuels, as well as easy storage and transport which is needed for portable applications.[10]

Although the DMFCs have been shown as an appropriate alternative to rechargeable battery technology, many problems still need to be addressed before large scale commercialization. Other than cost and performance requirements, common to any type of fuel cell, DMFC suffer from the undesired methanol crossover phenomena, which happens when methanol molecules diffuse through the membrane and are oxidized at the catalyst surface on the positive electrode. This phenomena can severely reduce both current density and cell voltage, as well as fuel utilization, and in general, cell performance. In terms of percentage, less than 30% of chemical energy in methanol can be utilized as electricity, while the rest is converted to heat as result of methanol crossover and irreversibility of electrode reactions particularly at the anode. Luckily methanol possess a high value of energy density (about 1.8 kWh kg^{-1} or 1.7 kWh L^{-1}), but it needs to be diluted to reduce methanol crossover. Cell stacks dimensions must be proportionally increased as a consequence. The effect can be mitigated by selection of proper membranes and oxygen tolerant cathodes, for example Fe-N-C catalysts.

Overcoming their problems, DMFC appear to be one of the solutions for the future of portable application. Durability is amongst their best feature as it has been

proven that a similar device can reach lifetime values of 20,000 hours providing 7 kW of power.[11]

1.4 The Oxygen Reduction Reaction

1.4.1 – ORR mechanism

Developing a mechanistic understanding of the ORR is fundamental for research on PGM-free electrocatalysts. This is the most active area of research as the reaction is very complex with several intermediate stages and a variety of pathways depending on a number of factors: pH, solvation characteristics of the electrolyte and the structure and composition of the catalyst.

The Oxygen Reduction Reaction (ORR) represent the cathodic reaction for a generic fuel cell, converting oxygen into water in a complex process that releases energy. Although the mechanism is still unclear, we know that involves the transfer of electrons, such as all the redox reaction, in a number that can be up to four (but in certain undesired circumstances, it's closer to two). Different models are developed for the reaction, and it strongly depends on the nature of the electrode surface as well as the media where it happens. For aqueous media, the reaction usually take a inner sphere mechanism with direct contact with active sites and gas molecules, but in strongly alkaline solutions, the reaction can undergo a outer sphere reaction involving one electron to give superoxide O2-. For the inner sphere a temporary bond is formed between the oxygen molecule and the active sites. The model developed by Wroblowa is the most generally accepted and simplifies the reaction steps into two main pathways: one is a four-electron process and the other is the two-electrons process which has a peroxide intermediate. [12]

The following are the main reaction pathways for ORR [13,14]

direct 4-electron pathway

$O_2 + 4H^+ + 4e^- \rightarrow 2\ H_2O$ Eo = 1.229 V (1)

2-electron peroxide pathway

$O_2 + 2H^+ + 2e^- \rightarrow 2\ H_2O_2$ Eo = 0.695 V (2)

which can be followed by accepting further 2 electrons

$H_2O_2 + 2H^+ + 2e^- \rightarrow 2\ H_2O$ Eo = 1.776 V (3)

or by the decomposition reaction

$2\ H_2O_2 \rightarrow 2\ H_2O + O_2$ (4)

As illustrated in the reaction scheme, oxygen can be directly converted into water in the first process (direct four-electron reduction) or can be reduced in two steps: a first reduction into hydrogen peroxide (two-electron reduction) and eventually peroxide can undergo further reaction although different pathways are possible, like the chemical decomposition to O_2 adsorbed on the electrode surface, or desorption into the solution. Kinetic studies demonstrated that the favored pathway is the one forming the peroxide intermediate, although this is undesired in fuel cell environment because it negatively affects the stability of electrode and membranes. Therefore, the best electrocatalysts are expected to promote the four-electron mechanism[15] as it releases the most energy. The 2-electron reduction of O_2 releases less energy and produces hydrogen peroxide and it is undesirable in a fuel cell. Further, this substance can attack cell components, so it is an undesired product of the reaction.

The electron-transfer mechanism can occur in either the inner or outer Helmholtz plane. The inner-sphere mechanism involves a strong chemisorption of molecular oxygen to the metal surface and is generally believed to be the most effective for the complete $4e^-$ reduction of oxygen. This reaction mechanism is known as the direct $4e^-$ transfer pathway, alternatively, the reaction can proceed via the two-step $2e^-$ reduction pathway in the outer-sphere in which a peroxide intermediate is formed

In this mechanism, an adsorbed hydroxyl species interacts with a solvated oxygen molecule, stabilizing it and promoting the $2e^-$ transfer to the peroxide anion (depicted by (b) in Figure 6). The next step can either be further reduction or disproportionation.

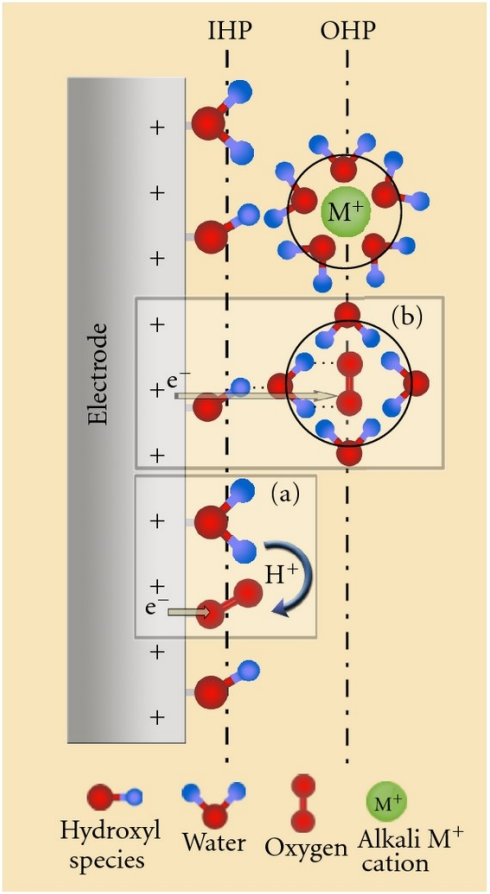

Figure 6: Schematic illustration of inner sphere (below) and outer sphere (above) mechanisms[16]

The two-step $2e^-$ transfer pathway can occur at the same site or in some cases the peroxide ion is believed to migrate to a separate site before undergoing reduction to hydroxide ions [16]

Cyclic voltammetry and linear sweep voltammetry (LSV) are the most used techniques for investigation of the ORR kinetics, using rotating disk electrodes. The first technique involves the measuring of potential-intensity curve in a potential range and allows the observation of oxidation and reduction peaks typical of the material. The curves obtained by LSV at low potential scan rate are fitted to the Koutecky-Levich model for kinetic information, which will be discussed in detail in chapter 3. For now, let's note that the number of transferred electrons (n) can be obtained from the slope of the K–L plots at different potentials. The use of rotating ring disk electrodes provides a method for directly measuring the peroxide

formation using the equation, as the ring around the disk serves as a peroxide amperometric sensor and is set at a constant potential (independent of the disk potential) at which peroxide oxidation is under mass transport control.[12]

State-of-the-art Pt-based electrocatalysts promote mainly the four-electron transfer process, allowing only a small amount of peroxide (≈1%) to be produced. As a general rule, the closer the electron transfer number is to 4, the better the catalyst is since the 4-e reduction of O_2 delivers more energy compared to the 2-e reduction in a fuel cell.

ORR is one of the most studied reactions because of the extremely sluggish kinetics at the cathode in low-temperature fuel cells. Even highly loaded Pt catalyst still can't reach the possible rates of the anode reaction, namely the hydrogen oxidation, which have 5 times higher exchange currents. Therefore, the ORR represent the bottle neck in the fuel cell performance, other than the aforementioned problem with the two possible pathways.

Porous structure is extremely important in developing efficient catalytic surfaces. In particular materials presenting mesopores, facilitate the diffusion of chemical species through the catalyst layer, thus the importance of porous carbon materials, which also show a good electrical conductivity[17].

A pioneering work was conducted in 1964 by Jasinski [18] in terms of synthesis of non-noble electrocatalysts for fuel cell cathodes. He developed metal nitrides which were the first type of material proposed as alternative to noble metals. In 2009 Gong pioneered the use of metal-free electrocatalyst by presenting N-doped carbon nanotubes with performance close to Pt/C in alkaline media. This lead the research towards nitrogen-doped carbon structure which have been considered the best starting point for next generation of catalysts [19]

In order to reach similar performances for platinum and non-precious electrocatalyst, alkaline conditions are required, while it is very difficult to reach the activity observed for platinum in acid media. In alkaline media the adsorption energy to the active sites is lower and there is a different mechanism that involves water molecules coordinated with metal ions, instead of the metal particles[16]. Nitrogen doping is an effective and interesting strategy because the incorporation into the sp^2 carbon structure increases the electrochemical activity and the electron-donor properties. In alkaline environment the reduced adsorption energy favors the ORR more than in acidic media that allows the use of PGM free electrocatalyst [20].

1.4.2 Nature of active sites

The precise nature of the active sites in M-N-C materials and their role in the catalysis of the ORR is still under much debate among researchers. This is a consequence of the significant scale of disorder of the catalyst structure introduced by the intense heat-treatment during synthesis.[21–23]

The chemical identity of the nitrogen functionalities is one area which has been studied extensively. Research has shown that quaternary nitrogen centres are the main source of activity with pyrindic and pyrrolic nitrogen contributing slightly. In fact, some researchers suggest the nitrogen-carbon moieties are the main source of the active sites in M-N-C electrocatalysts.[24] In this school of thought it is reasoned that the transition metal atoms are responsible for the formation of these moieties during heat-treatment but play no role in the catalysis

However, it is widely accepted that catalysts containing M-N_4 moieties – where a metal (M) atom is coordinated to 4 nitrogen molecules – are very active for the full $4e^-$ reduction of oxygen. Zúñiga et al. carried out a study to verify if the iron centres were involved in the inner-sphere ORR by poisoning the active sites with cyanide. The results showed decreased overall activity but the same onset potential for peroxide ion production in both poisoned and non-poisoned iron sites. This indicates that the nitrogen groups on the surface of the graphitic carbon are responsible for the production of peroxide. This implies that the metallic centres give rise to the highly active $4e^-$ transfer in M-N-C materials.

Activity can be modulated by tailoring the incorporation of nitrogen into the sp^2 carbon structure. The nature of catalytic sites is still under debate as well as the reason for the higher activity of N-doped carbon materials. One explanation is that the doping with nitrogen leads to a stronger interaction of C atoms with oxygen because of different charge distribution in the carbon structure, which is different because of the higher electronegativity of nitrogen. This brings the adjacent C atoms to gain a more positive charge, permitting an enhanced interaction with oxygen molecules in the process of dissociative adsorption.[25]

Four types of N-bonding are identified by the deconvolution of N 1s peak in XPS spectra, and it has been widely accepted that the bonding highly affects the ORR activity. Pyridinic-N (at ≈398.3 eV) refers to edge sites: N atoms bond to two carbon atoms and donate one p-electron to the π-system. Pyrrolic-N refers to a five-membered ring where N atoms are bound to two C atoms. Their contribution to the π-system is of two p-electrons thus have higher binding energy (at ≈400.1 eV).

Quaternary-N or graphitic-N (at ≈400.9 eV) refers to a bond to three adjacent C atoms after a replacement of a C atom with a N atom occurs. Compared to pyridinic-N, pyridinic-N-oxide bonds to two carbon atoms and one oxygen and it's identified with a shift in binding energy of +5 eV (at ≈403.5 eV) [26].

Because of the dependence on the electronegativity, not all bonding configurations have the same effect, and also the structure of graphitic carbon network affects the ORR activity. Even if some researchers did not find a correlation [27] most researchers assume that the nitrogen content improves ORR activity.[28] Also, the type of functionalities is important and there are studies reporting the activity enhancement by pyridinic-N and graphitic-N and also both functionalities.[29,30]

Another common strategy is the doping of the material with heteroatoms such as halogens, boron (B), sulfur (S), phosphorous(P) and silicon (Si). Different groups reported the doping with heteroatoms to induce synergistic effects correlated mainly to their different sizes and electronegativity ocompared to carbon, which leads to polarization of the adjacent carbon atoms therefore facilitating oxygen adsorption and dissociation[31,32].

The recent progress achieved for PGM-free electrocatalysts as well as doped porous carbon materials obtained from different chemicals and methods is reported in multiple reviews.[33–37]

While many catalysts involve a metal-free synthesis, claiming their activity to be related to porosity and heteroatoms doped into the material structure, lots of catalyst instead make full use of the presence of metal, either introduced in the synthesis or already present in the starting biomass. The most common choice is iron, not only because it's cheap and easy to introduce but it's also the most studied between non noble metals.

In 2009 it was claimed by Jaouen group that the main pathway for ORR was a direct 4 electron route with minor H_2O_2 formation and disproportionation. Their catalyst was obtained by impregnation of a carbon black support with aqueous solution of iron II acetate and the nitrogen was introduced in a subsequent pyrolysis with NH_3. Observations were made based on electrochemical measurements of produced H_2O_2. [22]

New techniques available in the following years allowed for a more precise study of the materials as well as the reaction, with in situ analysis becoming prominent in the clarification of the electrocatalyst mechanism.

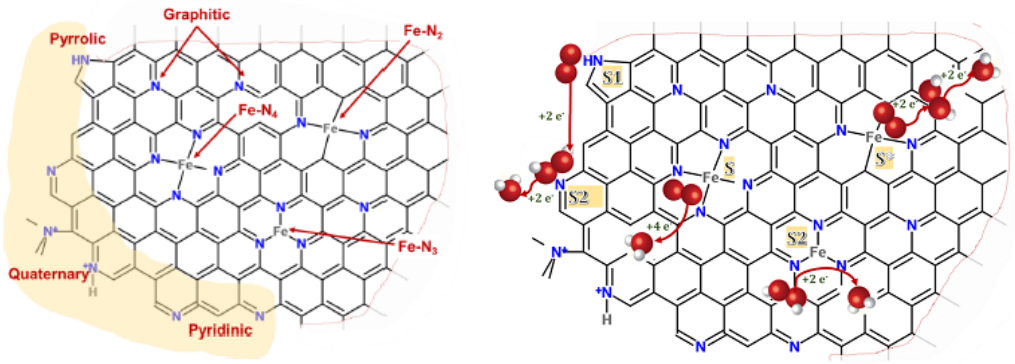

Figure 7: Different active sites and reactions in a Fe-N-C catalyst [38]

Different sites for ORR activity have been identified by studying a large number of published electrocatalysts. The characterization involved both metal and metal free sites and its main objective was the comparison of the selectivity towards 4 electrons and 2+2 electrons process.[38] Comparative ORR activity analysis on several Fe-N-C catalysts showed close range of onset potentials, and similar Tafel slopes in range of 56-63 mV suggesting common rate-limiting steps, involving one-electron transfer (albeit this is still a rudimentary interpretation and need to consider the high loading of catalyst)

Nitrogen and iron−nitrogen functionalities investigated consist of in-plane defects in the carbon structure such as graphitic nitrogen or iron atoms coordinated to 3 or 4 N atoms, or different edge sites like pyridinic, pyrrolic or quaternary nitrogen and Fe-N_2/Fe-Nx sites. Basically, for a Fe-N-C electrocatalyst, it's worth analyzing both the metal sites but also the N only sites to distinguish it from a metal free material.

There are two main hypotheses: one claiming a direct responsibility of nitrogen sites in carbon support for ORR activity, the other suggesting metal ions are the actual reactive centers while the role of nitrogen is to act as a coordinating environment for those ions.

By theoretical calculations, incorporation of nitrogen atoms in the carbon matrix is confirmed to enhance its electronic properties, but nitrogen atoms are not catalytically active toward the direct reduction of oxygen. In fact, mechanistic studies of ORR claims that only the first step of ORR ($O_2 \rightarrow H_2O_2$) is occurring without metal. With a combination of density functional theory calculations and microkinetics simulations, the Fe-N_4 moieties have been identified as a very

effective source of activity enhancement in non-noble catalysts. More noticeable, the edge sites in graphitic and graphenic planes can originate a unique tilted Fe-N_4 configuration with interesting ORR catalytic properties. A shift in onset potential has been observed compared to the non-tilted configuration. Theoretical calculations confirm the energetic advantage of the binding of metal site with O_2 and dissociation with side-on binding (two oxygen atoms bound to the same Fe ion). The conclusion of the study was that the tilted FeN_4 configuration can be at zigzag or armchair edges of graphene, the first can shift the onset potential for the associative reduction mechanism (0.13 V), the other has high onset potential for the dissociative reduction mechanism (0.26 V higher than a not-tilted configuration).

Integration of Fe-Nx sites in a π -conjugate carbon plane, like graphite or graphene, favors the alteration of electron withdrawing and donating capability for the carbon layer, leading to improved ORR activity. This was proved by Atanassov and coworkers using iron porphyrins and using a combination of in situ X-ray spectroscopy as well as electrochemical analysis. There are actually two mechanisms proposed for alkaline and acidic media. In alkaline environment the single site 2e x 2e mechanism is prominent while in acid media the dual site 2e x 2e mechanism take place instead and the surface bound Fe/FeO nanoparticles have a significant role as secondary active sites. [39]

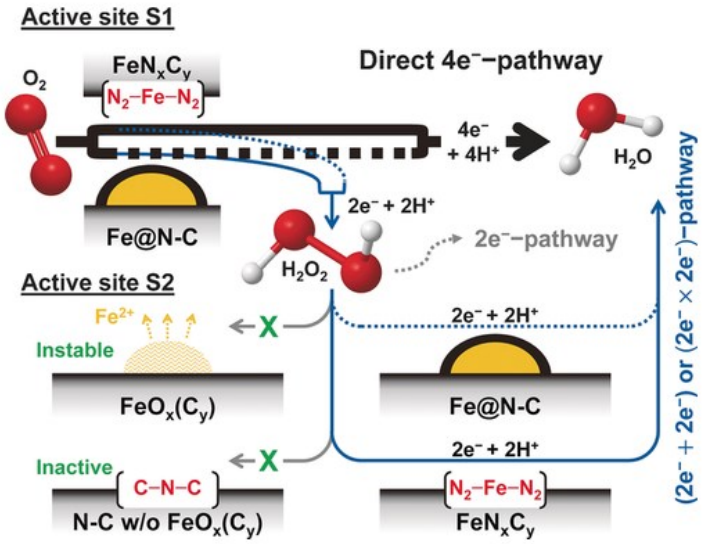

Figure 8: Different pathways for ORR in the environment of a Fe nanoparticle [38]

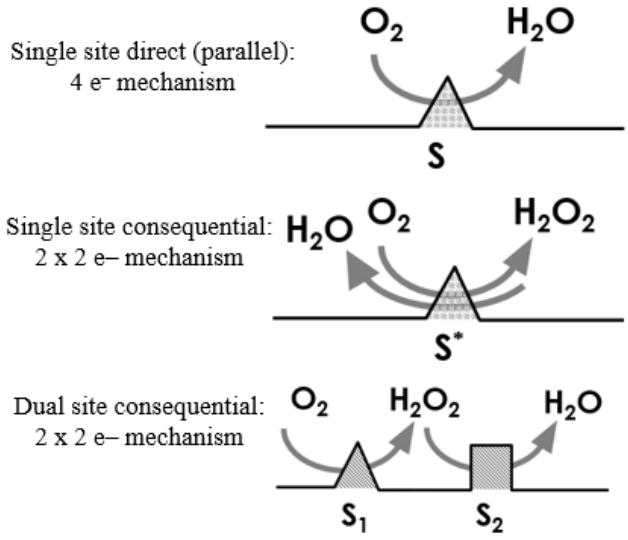

Figure 9: Difference between single and dual site[21]

Alkaline: Fe-N-C converts O_2 to water because it stabilizes the peroxide anion intermediate on the Fe-N coordinate site, entire $4e^-$ reduction occurring as single site process on the metal-N center.

Acid: Fe^{2+}-N is still responsible for initiation and reduction to peroxide, there is need for secondary active centers adjacent due to poor H_2O_2 molecular intermediate stabilization

Proofs of these assertions are in electrochemical and physical tests: electrochemical analysis confirms the presence of a $Fe^{2+/3+}$ redox and proves the role of iron in initiating the reactions, while XANES results confirm presence of Fe-N_4 moieties and direct involvement in mechanism similar to heme for not pyrolyzed materials. Microscopic fine techniques, like high-angle annular dark-field scanning transmission electron microscopy (HAADF-STEM) and high-resolution transmission electron microscopy (HRTEM) showed the dispersion of Fe atoms around the edge of graphitic pores, in the mesopore range (4 to 10 nm)

Porous structure is also crucial in the catalytic activity, especially when moving from the RDE environment to the actual fuel cell. Tunability of the pores is achieved using appropriate starting materials and dopants and optimized methods

of synthesis leading to a hierarchically structure with micro-meso-macro pores. Such a structure can be achieved for example using metal organic frameworks (MOFs), which are by definition a hierarchically porous structure which can lead to a homogenous distribution of active sites when metal functionalities are introduced.[40]

M-N-C electrocatalysts can be prepared from a variety of precursors such as metal salts or metal macrocycles. Since the pioneering study on a cobalt-based phthalocyanine catalyst by Jasinski in 1964, much research has been conducted on transition metal catalysts from macrocycle precursors. It is interesting to note that formation of Fe-N_4 moieties upon pyrolysis has been observed even for non N_4 materials, suggesting a stabilization of the structure.

As for the nanoparticles, they can stay intact after several acid washing, attributed to presence of protective graphene like layers which are responsible for stability and durability of these materials.[41]

Several methods of synthesis have been explored such as the doping of graphene or the sacrificial support method which can result in very high specific surface areas. The common goal of synthesis is to produce active sites on a highly porous, graphitized carbon. The process of heat-treatment through pyrolysis is fairly standard for catalyst preparation. However, it is possible to produce electrocatalysts with ORR activity without the need for heat-treatment of precursors.

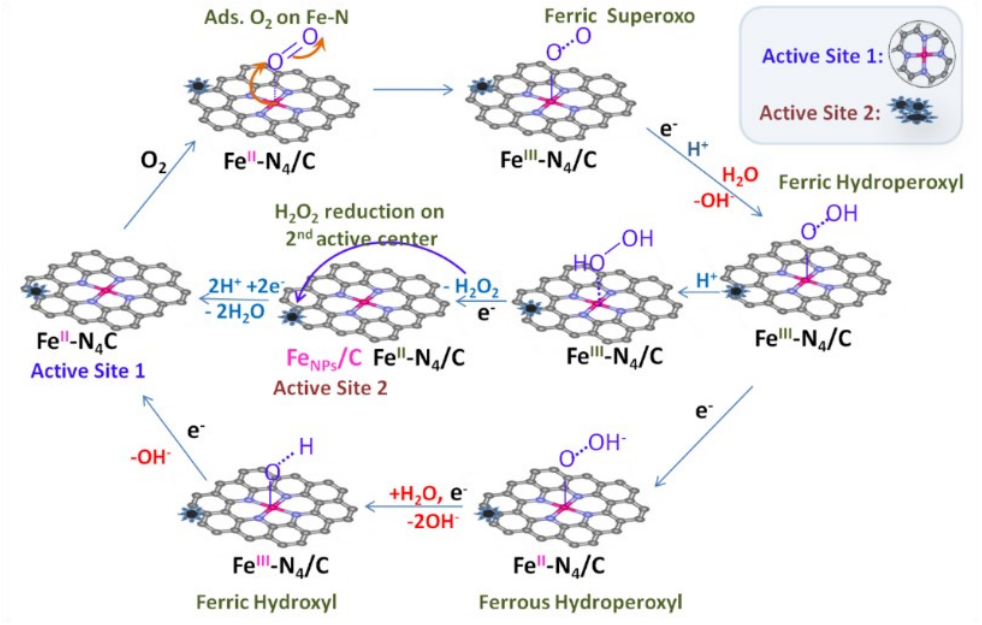

Figure 10: Proposed mechanism of ORR with Iron active centre[42]

Chapter 3

Biomass as catalyst precursor for ORR

2.1 Aim of the work

The focus of this project is the development of platinum-free catalysts to be used as cathode material for alkaline exchange membrane fuel cells. Because of the sustainable and efficient method of energy production of the fuel cells, it is our interest to join the research in the field of Fe-N-C catalyst to overcome the Pt dependence and obtain a new efficient catalyst at low cost. Chapter 1 already gave an overall description of fuel cell mechanism of function, advantages, and problems to overcome. The role of metal and the reason for focus on ORR reaction is explained, and that will justify our choice for the synthesis of Fe-N-C compounds where iron and nitrogen are supported on a porous carbon.

The choice of porous carbon in fact is where we want to differentiate our research from common studies presenting a mix of iron salts and commercial carbon with good activity. Albeit that is definitely worth recycling and interesting to develop, our focus is also on terms of waste recycling and circular economy development, for that reason we reviewed different case of biomass-derived materials studied for ORR application that will be presented in the next paragraphs. The European Union has recently set several long-term targets regarding landfilling and recycling, as a part of the new Circular Economy Package, launched in 2020. A binding target is that by 2030 it is expected less than 10% of municipal waste may go to landfill in EU countries. Furthermore, new laws should include a total ban on the landfilling of waste already separated and sorted for recycling. On top of that, it's expected in Europe for both recycling and re-use of civil waste to reach the value of 65% by the year 2030, with an expected goal of 75% regarding the recycle of packaging waste. Although specific targets involving resource efficiency as well as plastics and food waste were not directly mentioned, it's still desired to meet the global Sustainable Development Goal of halving food waste by 2030 and

for this reason the EU still reiterated its commitment in the cause. These goals of course would need a large change in the current EU waste management, because presently recycle interests only 40% of municipal waste, while more than 30% is landfilled. Therefore, a number of supporting measures were announced, in order to promote a circular economy approach for each step of the value chain – which ranges from production to consumption, repair and remanufacturing, waste management, and feeding back of secondary raw materials. These activities are going to be supported with financial aids from the European Regional Development Fund.[43–45] Circular economy is one of the most challenging but also more rewarding opportunity of the next decades, as it will require a huge change in the production and consumption system but the desired outcome is extremely appealing, with billions of dollars as a potential reward for an economy that find its starting materials in its own wastes.[46–48] In fact, the most relevant obstacle in the passage to this kind of system is not the conversion of existing production methods but instead the acceptance from the consumers, meaning that it's not enough to engineer the perfect factory to recycle paper or glass if the people is not willing to differentiate their waste. But on the other hand, education on the advantages of the approach could lead to an even easier transition. It's interesting to note that the forma mentis of recycling waste into new value-added material is useful in every situation, for example during the COVID-19 pandemic situation, an enormous amount of chirurgical masks were thrown away after use meaning waste, but with a circular economy approach, finding a usage for that material is possible, and in fact it was studied by a group in Milan University.[49,50]

Our work started with this consideration. There are already different ways to recycle waste material or at least burn it to provide thermal or electric energy but there are few hypotheses on giving new life to waste materials as catalyst for fuel cells. It's sure an interesting challenge because it's not expected in the short term to reach very high performances compared to commercial catalyst, but a systematic and high-throughput survey on different types of materials and procedure could lead to a new potential application for biomass derived waste, which as we already mention, include wastes from agricultural crops, animal residues and even sewage from cities, meaning that a part of the now unrecycled wastes could find a new application instead of remaining in the landfill.

As a test material, we decided to focus on two specific plants: tea and coffee. They both are very common to grow in different environments and their products are usually consumed during meals, and especially in Italy there is a growing culture of preparation and serving of coffee and tea. For this reason, we can assume waste

recovery, may it be from domestic waste or from factory refuse, to be at practically zero cost, therefore only the chemical treatment needed to enhance activity would be the cost of the synthetized catalyst. Therefore, we claim the choice of carbon support from biomass is done for two reasons: one of economical origin because of the low cost, and the other of sustainability, because we sought to transform a common thrown away waste (although not a polluting one) to a high value material with applications in one we think may be a crucial technology in the future, namely the fuel cells.

The properties of biochar are known and analyzed in literature by different groups: pyrolysis of biomass leads to a highly conductive graphitized carbon structure arising from the high temperature pyrolysis. All the catalyst will be prepared by ball-milling iron (ii) phthalocyanine with a carbon support derived from pyrolyzed biomass. The performance will be evaluated in rotating ring disk electrode and electrochemical properties will be compared to state-of-the-art catalyst and justified in terms of physical and chemical properties. In order to compete with commercial porous carbons, the support must be durable and have good electrochemical performance. These properties are largely dependent on composition and structural features such as specific surface area and pore-size distribution – this will be discussed in more detail in Chapter 3

The main goal of this investigation was to evaluate and explain the effects of different pyrolysis conditions and chemical treatments on the biomass-derived carbon support. Between the many physical techniques employed to analyze the samples, great importance is considered for BET analysis to investigate the porosity and specific surface area, and microscopy techniques like FESEM and TEM that allows us to get a clear vision of the sample to nanometric level. The experimental aim of this project is to compare the effectiveness of a variety of different catalysts derived from the same precursors that have underwent different synthesis procedures. Namely, varying the pyrolysis conditions or type of chemical treatments applied to the catalysts. A commercial 20% wt. platinum on carbon-black (Pt-C) catalyst is also analyzed to benchmark the catalysts. The target, however, will be a catalyst similar to that synthesized in a previous work in the organisation using FePc with carbon Vulcan. This allows for a fair comparison of a tea-derived Fe-N-C catalysts with a well-established mesoporous carbon.

2.2 What is biomass

Biomass resources, as already pointed out, are abundant, cheap and renewable[51–54] Therefore, thanks to these advantages conversion of biomass derived material into active electrochemical species has drawn the attention of various research groups in the last decade[55,56]. Different materials have been tested either for supercapacitors or batteries [57,58] as well as hydrogen evolution reaction, oxygen evolution reaction [59] CO_2 capture[60,61]. The conversion of biowastes into active electrochemical catalysts has become a real and attractive possibility in order to obtain carbon nanostructures and high performance catalysis. In order to become commercially available, it is crucial to consider different variables such as the cost of the electrode, particularly the cathode. There are many ways to categorize the biomass resources, one is shown in figure 11.

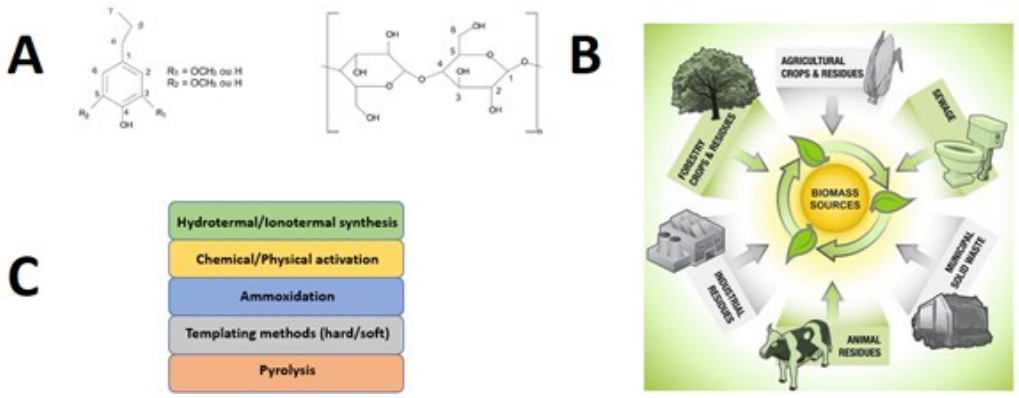

Figure 11: Chemical formula of Lignin and Cellulose (A); Different sources of biomass material (B); Different process available for the conversion of biomass wastes into catalysts (C) [62]

One possible categorization is based on the origin of the waste, which can derive from plants (natural forest or agricultural crops) or animals but also from industrial residues or sewage. Plant biomass derives from the biological photosynthesis and includes all types of vegetal residues, including but not limiting to, grass, trees, fruits, seeds and leaves. Animal biomass includes waste of animal origins like bones, horns, feathers, blood, cells as well as manure and human waste; these resources are composed mainly by proteins and minerals and their composition can be exploited when developing a doped catalyst. Biomass can either be harvested directly from the source or can be obtained from human waste after the biomass has been used before. For our purpose, the interest lies in biomass not used for its

primary scope, meaning the focus is more on the wasted residues than the direct harvest of the biomass.

In the case of plant biomass, the main constituent of cell walls is lignocellulose, which is made by a combination of cellulose, hemicellulose, and lignin. Cellulose is a polysaccharide formed by repeated units of glucopyranose, with β-1,4 glycosidic bonds and intermolecular hydrogen bonds within the matrix resulting in a orientation and degree of polymerization. It forms, surrounded by hemicellulose and lignin, the skeleton of the cell wall[63]. The structure is packed thanks to both hydrogen forces and weak van der Waals interactions, obtaining a crystalline structure constituted by long cellulose chains (micro fibrils).

Isolated cellulose mainly includes cellulose nanofibers (CNFs) and cellulose nanocrystals (CNCs). Typically, nanofibers are in the range of 4-20 nm, and length in the range of micrometers. It is possible to isolate these from bleached pulp fibers using high pressure and velocity impact grinding, homogenization, or micro fluidization. In contrast, nanocrystals are shorter, the range is 100–1000 nm, and can be obtained by acid hydrolysis, constituted by crystalline and rigid particles[64].

Another type of cellulose is the bacterial cellulose (BC), chemically identical to plant cellulose but with higher crystallinity and mechanical properties. The three dimensional network of nanofibers has higher purity because it does not contain lignin or hemicellulose [65].

Lignin is a 3-D complex amorphous organic polymer composed of aromatic units that differ in substituents, connected by oxygen bridging bonds and C-C bonds. It serves to connect cellulose, hemicellulose and pectin giving rigidity and mechanical resistance to the cell wall, together with impermeability and antimicrobial properties. Lignin is obtained in the form of black liquor, produced in cellulosic pulp mills and burned for cogeneration and chemical recovery. Therefore, the main source of lignin is paper industry, but is consumed as a fuel[66]. Hemicellulose is a heteropolysaccharide, with varying composition depending on the sources, mainly xylans and glucomannans. Usually the polymerization grade is lower than 200, only amorphous phase is present and acetylation in the chains is possible.

There are other polysaccharides that have been studied as precursor for catalyst. For example, starch: it is a glucan, its main components are amylopectin and amylose, held together by glycosidic bonds. Another example is chitin which has a similar fibrillar structure to cellulose and is the main component of cell walls in fish scales and fungi as well as exoskeletons of arthropods [67]. After deacetylation chitin can be converted in chitosan, a copolymer of N-acetylglucosamine and glucosamine. In

neutral pH, chitosan is insoluble in aqueous solutions but it is possible, in lowly acidic PH, to protonate the aminic groups and obtain dissolution[68].

Biomass main source are bacteria, fungi, marine algae or plants, agriculture wastes, human wastes, industrial wastes (which is usually contaminate) and animal-based wastes. Most of the worldwide available biomass is commonly used in Africa and India for heating and cooking, uses that are not efficient and not renewable. More advanced applications are in paper and pulp industry and building and power industry. Green nanocomposites and ionic conductors are prepared from biopolymers, and there is also energetic applications in biofuels, but this is only slightly better than fossil fuel because the lower pollution is compensated by side effects on food availability and bio-diversity [69]. A recent interesting application is the production of syngas starting with both plastic (HDPE) and biomass waste, obtaining both the H_2-rich gas mixture but also carbon nano tubes with possible development as electrocatalyst support.[70]

The choice of the synthesis is crucial to obtain the most performing material, with high surface area and the correct porosity and with accessible and stable reactive sites. Among various synthesis strategies conducted for biomass resources, the most common are hydrothermal carbonization, chemical or physical activation, ammoxidation, templating methods (hard or soft templating), carbonization and pyrolysis with leaving reagents. Both single step processes and combination of the process have been studied, and it is common to use a nitrogen or heteroatom-containing precursors, as well as transition metals, all of these atoms have been proved to improve the catalytic properties of the final electrocatalyst.

Hydrothermal carbonization involves dehydration, condensation, polymerization and aromatization to obtain a carbon material from a biomass resource, it is normally performed at temperatures below 200 °C, and under self-generated pressures[71,72]. Thanks to the mild conditions of synthesis, HTC-derived carbons show quite low surface areas (possible to see values lower than 10 m^2g^{-1}) and poor electron conductivity, therefore further treatments are needed for example activation or graphitization. In ionothermal carbonization (ITC), instead of water ionic liquids (ILs) are used because of thermal stability, stabilization of the mixture ability and low volatility [73].

Chemical activation usually involves impregnation of the biomass with dehydrating reagents, examples are KOH, NaOH, H_2PO_4, $ZnCl_2$, followed by a pyrolysis step above 300 °C [74]. As for physical activation, there are two steps involved: a

preliminary carbonization in inert atmosphere at temperatures above 500 °C followed by the actual activation obtained with either steam or carbon dioxide at high temperatures (around 1000 °C) [75]. High surface area is obtainable with ammonia treatment, a process called ammoxidation[61] , which involves the formation of nitrogen radicals and attack on carbon fragments by atomic nitrogen and hydrogen is possible to form the N-containing electroactive sites [76].

In the hard-templating method, a sacrificial scaffold is used, for example mesoporous silica, clay, or zeolites. The purpose is to guide the formation of desired pores during the pyrolysis. Soft templating method instead involves a cooperative assembly between templating agents and carbon precursor to direct the organic structure, for example surfactants in solution or polymer. Another option to avoid templating or chemical activation is the use of highly porous carbon aerogels, which are obtained from polysaccharides such as starch, chitosan/chitin, and cellulose. The synthetic strategy typically involves the formation of a hydrogel, followed by solvent exchange with a lower-surface-tension liquid, and subsequent free drying followed by final carbonization [77].

For all the aforementioned methods, it is quite common to have pyrolysis or carbonization as unavoidable step. Temperatures in the range of 700–1000 °C are the most common one although it's possible to go above to obtain high value materials. The process is needed to eliminate volatile compounds such as CO_2, CH_4, CO, and some organics, leaving only a carbon-based solid material. A recently trending strategy is pyrolysis with leaving reagents taking advantage of inorganic elements which biomass naturally contains, useful to assist the formation of pores during heat treatment; they are subsequently removed by mild acidic solutions [78].

2.3 Biomass Examples

Cellulose nanofibrils (CNFs) have been used by Mulyadi et al. [79] to obtain a very good electrocatalyst active towards both ORR and HER. The strategy used is the combination of a N,S doped nanofiber network and a N,P-doped nanoparticles coating. The synthetic steps involve three passages: first a solvothermal process at 245 °C, then a lyophilization step and lastly a pyrolysis at 900 °C. Albeit not exactly straightforward, synthesis is still easy to realize and the produced material exhibit activity towards both the ORR and the HER. This is a result of the integration of the more exposed highly active N,P-doped carbon, allowing an accelerated electron transport through N,S-doped carbon nanofibers as good conductivity channels promoting better charge transfer, thus enhancing the activity.

A common component of food or vegetable waste is starch, which is studied by Yao et al in a process involving hydrothermal carbonization with iron ions and annealing in NH_3 atmosphere. The active sites derive from the metal ions while the ammonia is not only used as nitrogen source but also to etch the carbon providing a porous structure. The resulting ORR electrocatalyst is constituted of N-doped spheres with a nano porous structure and has been proposed as substitute for commercial catalyst in zinc-air batteries due to good electroactivity in acidic and alkaline environment.[80]

Borghei et al. developed a catalyst from coconut shells obtaining a highly porous N, P doped carbon structure after activation of the biomass with urea and phosphoric acid at mild temperature (550 °C), followed by functionalization and 1000 °C pyrolysis. 7 Because of high density, high content in carbon and lignin (50%) as well as low ash content, coconut shells are a good starting material. Carbon structure can endure the pyrolysis without shrinking thanks to the binding of phosphate and phosphate ester to the lignocellulose. Specific surface area obtained is 1216 m^2g^{-1} and is speculated that a prior functionalization treatment aimed at forming oxygen group in the surface could improve the N content thanks to a better anchoring of urea. [81]

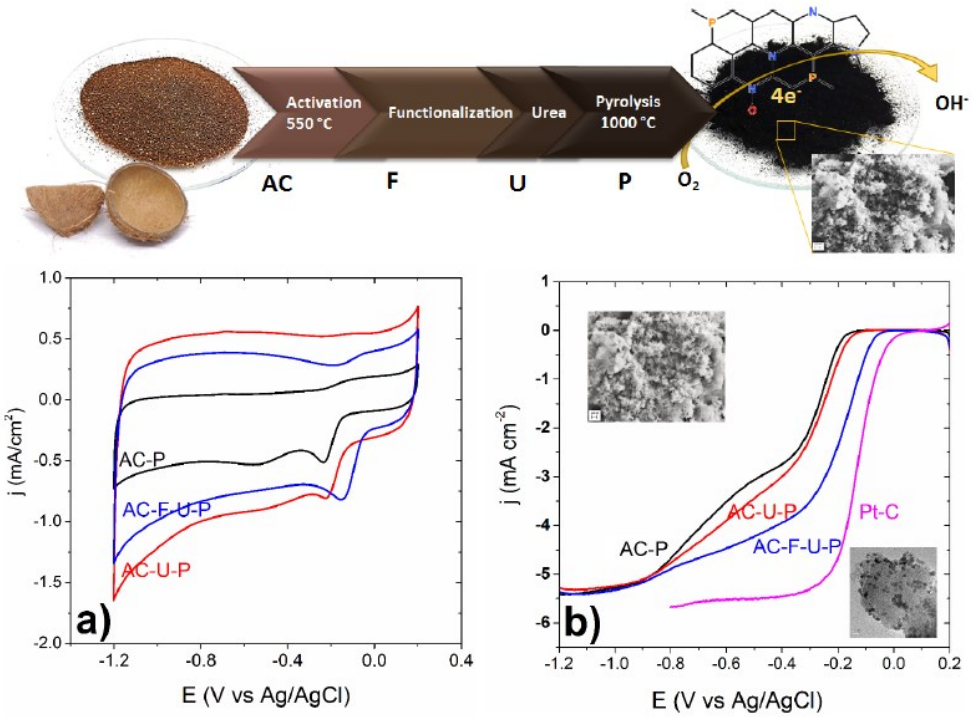

Figure 12: Coconut derived catalyst: CV and LSV plots[82]

Coconut shell were also used by Schonvogel et al.[83] to obtain a Pt support for fuel cell application. The process involves a hydrothermal carbonization, and the obtained catalyst has similar activity (slightly lower) than commercial Pt/C. This type of application is different than most of the electrocatalyst presented in this work, as the biomass role is limited as support and the catalyst is still considered a noble metal catalyst because of Pt inclusion, nonetheless it is reported as an alternative approach for alternative biomass use in electrocatalysts.

A catalyst with good electroactivity and stability towards fuel crossover and continuous cycling was synthetized by Gao et al. [84] from bamboo fungus, a type of fungus with high protein content and little medical value. Because of the source, the material is already N enriched without further doping. The synthesis involved hydrothermal treatment and heat treatment, and the product has ultra-high surface area (1895.5 m^2g^{-1}). The approach appears to be quite straightforward for different types of starting biomass without need of adding reactants.

A N,F-doped porous carbon from tea residue (tea leaves after brewing) was obtained by a one-step pyrolysis without activation or any post treatment. The synthesis is very straightforward and the material shows interesting electroactivity and durability; there is also a very sharp preference for the 4 electrons pathway that can be assigned to the synergy between the dopants, especially fluorine that, although not a common choice as doping atom, allows a more relevant charge distribution because of high electronegativity [85].

Hao et al.[86] reported a series of defective carbon catalysts prepared with a so-called N-doping-removal process using seaweed biomass and sodium alginate, a polymer with tunable viscosity, as precursor. The process involves doping and early removal of nitrogen atoms, obtaining an almost 100% carbon structure but with defects left in the position previously occupied by nitrogen. The double pyrolysis at high temperature guarantees the stability of the structure. It is possible to obtain a fine tuning of the defects, as well and porosity characteristic and conductivity by manipulating the pyrolysis temperature and viscosity of sodium alginate, and it's been demonstrated that all of these parameters significantly affect the ORR performance. The optimized porous carbon catalysts show abundant ORR-active defects, as well as a hierarchical porosity, good conductivity and a very high specific surface area value of 1377 m^2g^{-1}. The catalyst demonstrated very good ORR activity as well as selectivity in alkaline environment, comparable to the commercial Pt/C catalyst but with much better stability and methanol tolerance. In acidic environment, namely 0.5 M H_2SO_4, it was still observed a considerable ORR

activity for the D-PC-1-900 which was deemed the best material. The activity in acidic environment is among the highest reported for defective carbons.

Eggplant was used by Zhou et al.[87] as a carbon source to synthetize doped N doped graphene to outperform Pt/C on alkaline media. High surface area (1969 m^2g^{-1}) graphene structure was obtained by two steps: first KOH activation at 800 °C and then ammonia oxidation process with a stream at 1000 °C. The natural eggplant possesses a unique porous plate like structure that absorb the KOH solution helping the formation of ultrathin layers. Measured ORR activity appears to be close to that of Pt/C in alkaline condition, and in acidic condition although onset potential is lower, stability and methanol tolerance is still higher. It is suggested that the combination of large surface area, high conductivity typical of graphene and efficient nitrogen content are the main reasons for the performance.

Spent coffee grounds have been studied as starting material: they were converted with a simple carbonization into a porous structure doped with N and P, from melamine and triphenyl phosphine were used as sources for N and P doping, respectively. The dual doped material had been compared to Pt/C and showed superior electrocatalytic performance and resistance to CO poisoning. Mass activity at 0.70 V is reported to be 34.53 mA g^{-1}. The porous network and the charge delocalization offered by the dopants is considered the reason of this behavior, together with the higher number of edge sites and degree of disorder mainly caused by P, which can in fact be considered active sites for the ORR. Microscopical analysis confirms the change in structure of the starting materials after the synthetic step, including an increase in surface area [88]

Animal proteins can be used as a source of amino acids, for example sheep horn, a common biomass waste has been used by Amiinu et al. [89] to obtain N,S doped graphene by a synthesis involving the pyrolysis of the biomass which is mostly composed of keratin. After heat treatment the horn material is disintegrated leaving a solid carbon residue with the doping of N and S, and releasing volatile species such as NH_3, H_2S and positive charge ions. It is interesting to observe that the thermochemical reaction taking place between functional groups and graphene oxide allows *in situ* generation of reactive N and S species, inducing the graphene layers to a trimodal 3D porous assembly reorganization. Due to this peculiar characteristics, the obtained material exhibit in both alkaline and acid condition ORR and OER performance comparable to platinum and superior to similar materials[89]

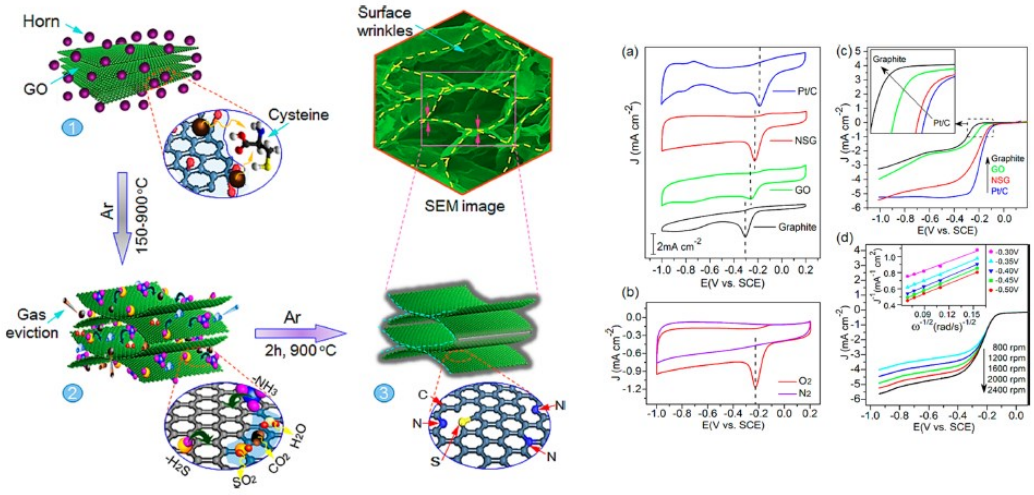

Figure 13: Sheep horn derived catalyst: synthesis and electrochemical curves [90]

Bamboo is a widely spread, fast growing plant already studied for pollutant absorption, it is known for a porous and conductive structure of its charcoal. Kim and co-workers obtained a hierarchically porous S,N-co-doped carbon electrocatalyst derived from bamboo treated with an ecological steam activation and further doping with thiourea, followed by pyrolysis. The synthesis allowed for control of mesoporous ratio, necessary for mass transport in fuel cell environment, while the co-doping with S and N enhanced the activity towards ORR allowing the catalyst to reach half wave potential of 0.85 V in alkaline and 0.47 V in acidic condition, both very similar to noble catalyst. The material is one of the few catalysts that reached the step of AEM fuel cell testing : a single cell test of the AEMFC was conducted under H_2/O_2 conditions at 60 °C and the best catalyst reached a value of 217 mW cm–1,. It has also be tested for Zn-air battery [91].

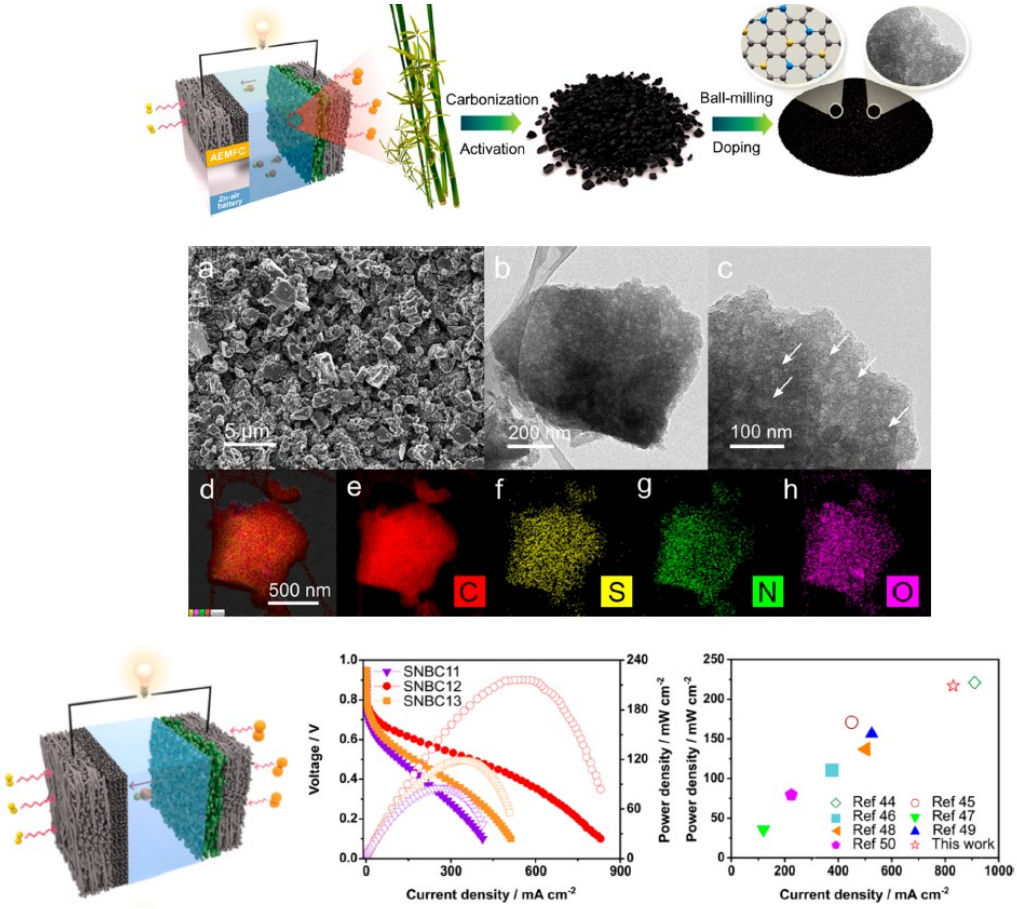

Figure 14: Catalyst from bamboo, SEM/TEM images and fuel cell tests [91]

Peat-derived carbons (PDC) were synthesized in a study of Jager and coworkers, using various carbonization protocols, leading to different surface morphologies, elemental compositions, porosities, and oxygen reduction reaction (ORR) activities. Five different carbon materials were studied as supports to synthesize Co-N/PDC catalysts, and five different ORR catalysts were obtained and tested. It is shown by the physical characterization combined with electrochemical data, that higher surface area, more surface oxide defects, and higher nitrogen content leads to higher ORR activity. In particular, the choice of carbonization method affects both the surface properties and electrochemical performance, showing a change of 740 mV between the worst and the best catalyst (E onset = 0,80 V)

The best catalyst was synthesized from $ZnCl_2$-activated and pyrolyzed peat and was tested in both rotating disk electrode and PEM fuel cell, reaching a value of

maximum power density value of 210 mW cm^2. The main value of this study, other than being one of the few papers reporting PEMFC test for biomass derived material, is the possibility of application of decomposed peat which is at the moment a resource unused because it cannot be used in agriculture or heating.[92]

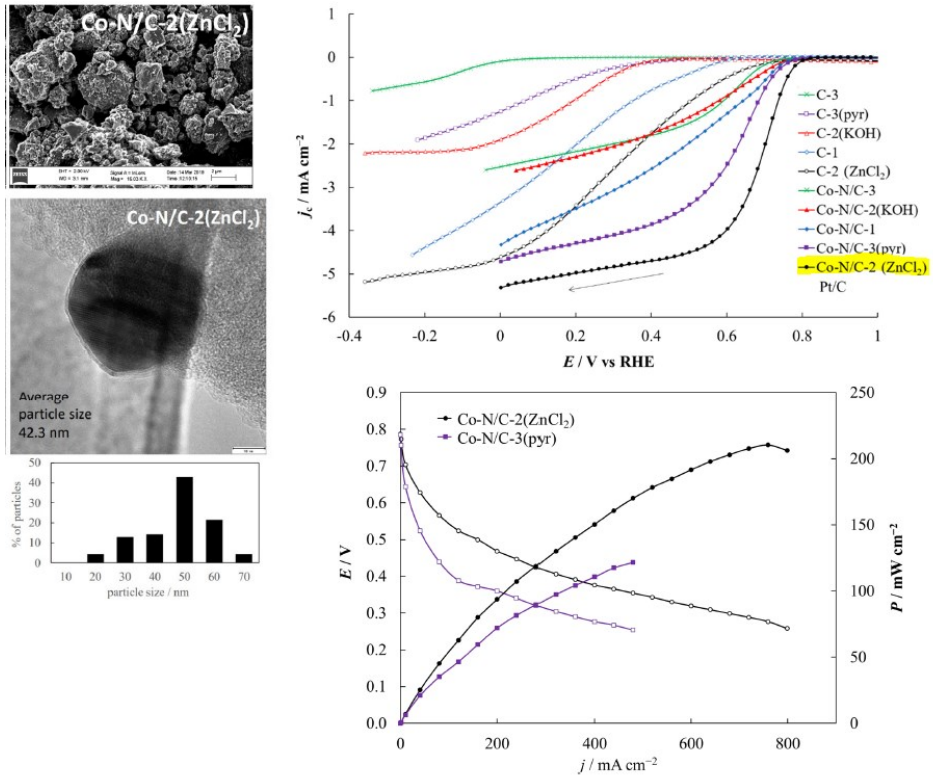

Figure 15: Peat derived catalyst, RDE tests and Fuel cell tests[92]

An environment-friendly strategy for scalable synthesis was proposed by Liu and coworkers using water lettuce as carbon precursor. Three-dimensional hierarchical porous structure was obtained, with a surface area of 823 m^2 g^{-1} for the best sample and uniform N-doping. The synthesis involved a first carbonization of Water Lettuce at 500 °C followed by annealing in N_2 or NH_3 at different temperatures followed by acid washing. The best catalyst is obtained with 800 °C treatment in NH_3 and show good electrocatalytic properties towards ORR which are retained at different values of pH. The material was tested in three home-made energy devices: a Zn-air alkaline fuel cell, a direct methanol fuel cell and a

microbial fuel cell. The Zn air battery exhibit a maximum power density of 240 mW cm^{-2}, the microbial fuel cell generated an average current of 2.37 A m^{-2} and power density of 1122.13 mW m^{-2} for the best catalyst. The Direct Methanol fuel cell exhibit a current density of 15.51 Am^{-2}. All these values surpass the commercial Pt/C catalyst that was used as a comparison. [93]

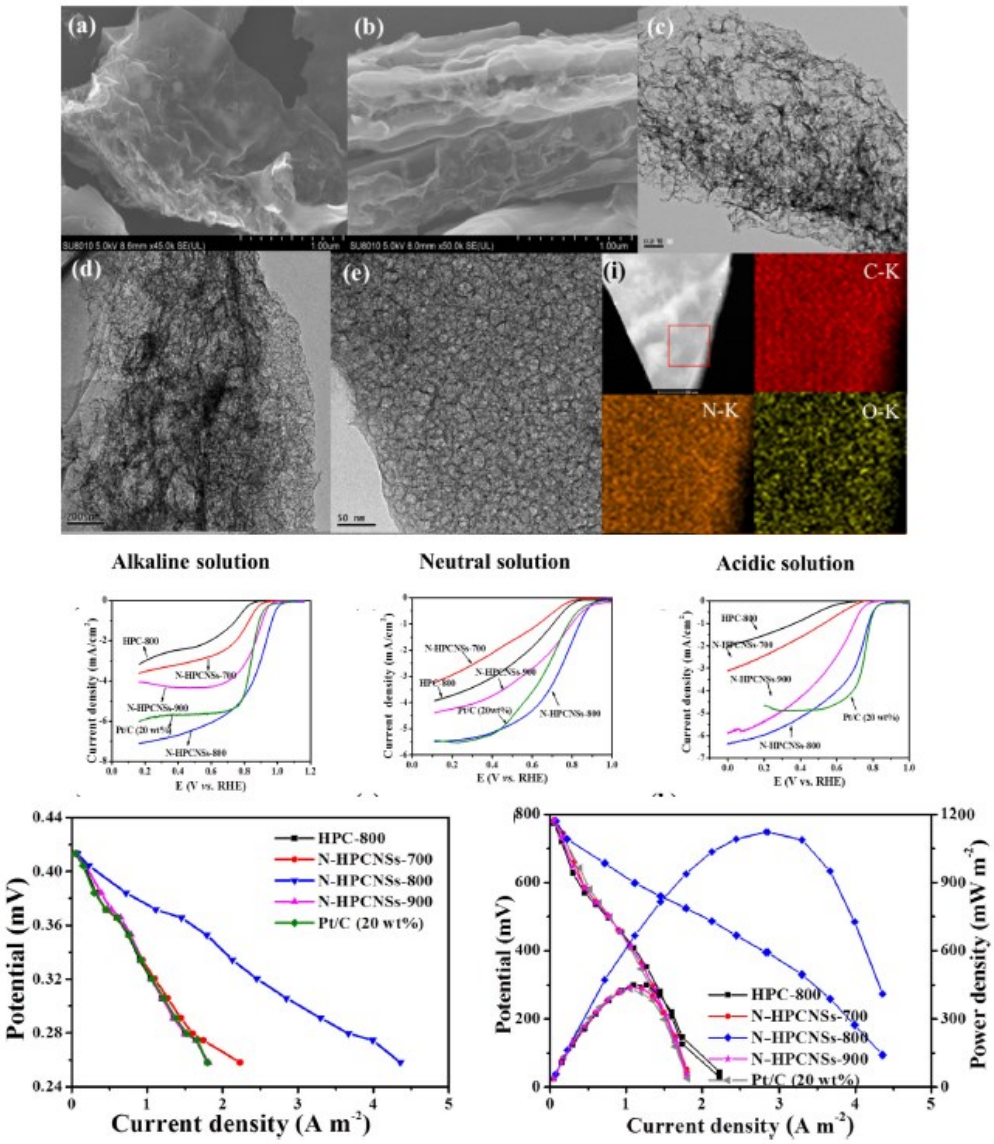

Figure 16: Catalyst from lettuce, SEM images and fuel cell tests [93]

Chapter 3

Materials and Methods

3.1 Ball Milling

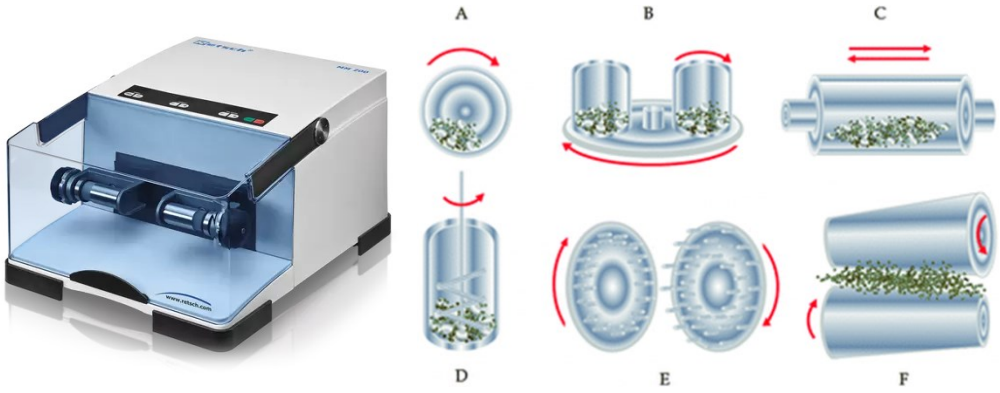

Figure 17: Picture of the ball milling machine employed in the present work and various mechanism of grinding (source: retsch.com)

Ball milling is a process, in which moving balls in a jar vibrates at high frequencies applying their kinetic energy to the material in the jar, usually a mixture of different solids, breaking chemical bonding and producing fresh surfaces by fracturing material particles. Ball-milling process is nowadays considered an efficient method for homogenizing a mixture as well as decreasing particle size for the synthesis of different catalyst. Usually employed before or after pyrolysis and in general, as an intermediate step in complex multi-step synthesis. There are reports of some studies that have prepared catalysts using only the ball-milling process for incorporation of desired Fe-N_4 moieties into the carbon scaffold. Previous work of our group obtained a good quality catalyst using iron (ii) phthalocyanine and carbon Vulcan using only ball-milling, outperforming the same material after pyrolysis and acid leeching. It is widely believed that local

temperature spikes due to the inelastic collisions can transfer sufficient energy to create active Fe-N-C sites. It's indeed testified by different studies that high energy ball-milling can create local temperatures in excess of 1000°C[94]

Mechanochemistry is often considered as a separate branch of chemistry because of the different mechanism in mechanical work reactions and heat reactions. This is not totally correct, and it is possible to obtain similar results like mechanical alloying or solid-state reactions with mechanochemistry. The temperature increase of milling balls was studied with calorimetric measurements. Measure is difficult because the need of a sacrificial mean of measuring (usually a thermo couple) and even this way, it's not entirely sure that measure is correct because of the punctual nature of temperature increase. Therefore, although 100 °C and 200 °C are commonly measured temperatures is suggested that oblique collisions and frictions lead to higher temperatures.[95] Ball temperatures over 600 °C are measured after 20 min of milling and this was coherent with model prediction It is also possible for impulsive temperature to reach 50-300 °C more leading to a highest local temperature closer to 1000 °C. Calorimetric measures are therefore probably inadequate to measure effective temperature and other methods need to be considered. During a mechanochemical process up to 80% of mechanic energy is dispersed as heat. Side reaction or heat sensitive products need to be taken into consideration, as well as liquefaction of organic substrates. In PBM (planetary ball mill) temperatures from 60 to 600 °C are measured depending on both the mill and the milling. Lamaty group obtained a mathematical model for the prediction of the milling walls temperature (although in balls, it can be even higher) and parameters affecting are the ball diameter, the filling degree, beaker size, the grinding stock filling degree, and the material properties of the stock. Frequency is also a fundamental parameter leading to higher difference when frequency is higher between the temperatures in ball and in walls. Strength can also benefit of long milling times, reaching up to 12 hours, it is possible to see in SEM the difference in structure for carbon nano tubes. It is worth noting that after 6 h performance starts to decrease.

Mechanochemistry has been employed in the synthesis of organic polymers, metal alloys and also metal-organic frameworks (MOF). It has been proved mechanochemical activation for carbon materials can produce hydrophilic surfaces leading to multifunctional carbon nanomaterial with different potential applications [96]. Graphite as a carbon source, can be milled with various chemicals such as melamine (solid) and carbon dioxide (gas) to introduce nitrogen sites at the surface or edge of the carbon material as well as carboxylic functional group, due to solid-

solid and solid -gas reactions. As another metal example, it was demonstrated that the ball milling process might increase the specific surface area, diminish the crystallite and particle size, and produce a reduction of the crystallinity of β-$Ni(OH)_2$, providing enhancement of the electrochemical performance of nickel hydroxide powder.[97] The electrochemical activity for pasted nickel electrodes obtained from ball-milled nickel hydroxide was tested. Therefore, a comparison between milled and un-milled nickel hydroxide electrodes was made, showing the different physical properties and enhancement of the electrochemical performances, confirming the possibility to use ball milling as a method to alter the physical properties to enhance performance for the active material.

Ball-milling is considered an efficient and straightforward method used for composite materials production. In the last decades, it has found application in the synthesis of doped carbon materials for ORR reaction catalysis, either alone or combined with heat treatment. Ball-milling has been proved to effectively increase the presence of catalytic sites in doped carbons. High-speed ball-milling process is used to obtain good blending of macrocyclic complexes and carbon supports and may also produce enhanced molecule–support interactions. On the other hand, because of the low-temperature of the process (even considering hotspots) it is possible to avoid the complete destruction of the Me–N coordination structure. Ball-milling was also combined with pyrolysis in order to obtain even higher surface area as well as porosity of the resulting materials. The effects of the ball milling on both performance and morphology of the catalysts may vary depending on different parameters such as temperature, rotation or vibration rate, milling time, and ratio of catalyst to carbon. For this reason, it's possible to modulate not only the assembling behaviors of FePc molecules during the process, but also the electrocatalytic performance of the produced materials, using different types of carbon nanomaterials, for example graphene nanosheets or carbon-black nanoparticles. This can produce molecular architectures of FePc ranging from uniform thin shells to nanorods, and the materials may exhibit in alkaline solution ORR activity values comparable or even higher than the state-of-the-art catalysts, namely Pt supported on carbon. [98].

Biomass applications are also possible: activated carbons derived from walnut shells were obtained by chemical activation with KOH and tested as electrode material for electrical double layer capacitors (EDLCs). The samples were ball milled for 8 h and characterized before and after the process to analyze their electrochemical performances as electrodes for EDLCs. BET analysis demonstrated surface areas of the samples decreased to approximately 10% of their

original value after ball milling process. However, it was also observed an increase in capacitances values and an improvement in other electrochemical properties such a charge/discharge stability and impedance. An investigation on pore size distribution revealed that while most of the micropores were destroyed, the amount of mesopores in the size range of 2–10 nm were increased, reasonably formed during ball milling treatment. X-ray photoelectron spectroscopy (XPS) analysis demonstrated an increase of 10% in the graphite content after milling. In terms of application to activated carbon from biomass, it is reported by Rajendiran group a synthesis of multifunctional material derived from Korean lotus root, inheriting heteroatoms N and S from the starting material and ball milled with activation agent K_2CO_3 following by thermal treatment[99]. The produced material is highly porous, has high gravimetric capacitance and good ORR electrocatalytic properties.

A work from University of Rome focused on the synthesis of FePc-N-C catalysts obtained by anchoring iron phtalocyanine on nanostructured carbon black pearls using a four-step process: substrate activation, dry impregnation, ball-milling and pyrolysis.[100] It is known that both ball-milling and pyrolysis can affect electrochemical surface area(ECSA), as well as catalytic performance and stability, therefore an optimization was made for both ball-milling and pyrolysis parameters in order to enhance ORR activity. Specifically, the aim was to improve the interaction between the FeN_4 macrocycle and the nanostructured carbon scaffold. High ORR activity was demonstrated in neutral media, certifying these materials as promising for bioelectrochemical systema. As expected, comparing the material to Fe-N-C samples produced without ball-milling treatment, the use of ball-milling produced an increase for the ECSA, ORR peak potential and peak current density. It was also observed that in certain cases pyrolysis after ball-milling shows detrimental effect on ECSA and other parameters, especially for samples obtained with higher ball-milling time. It is speculated this was caused by the formation of metal iron and iron oxide in the samples after the long treatment, both of these iron sites being less active for ORR for ORR compared to nitrogen-coordinated iron.

Carbide derived carbons (CDCs) were studied as it is possible to synthesize these materials with differing degrees of graphitization, thus being easy to either modify or increasing resistance to corrosive processes. It has been proven that high-performance ORR catalysts can be obtained by ball-milling treatment of a mixture of CDC, 1,10-phenanthroline and iron(II) acetate. The addition and ball milling of the phenantroline as a pore filler however was shown to decrease the CDC surface area of a significant value, even more than 50% in some cases. Therefore, a study was conducted in order to observe the effects of both the ball milling conditions and

the pore filler to the surface area, the porosity and particle size of derived CDC material, also correlating this modification to ORR activity. Different synthetic strategies was also adopted to alleviate the loss of porosity during the synthesis, while retaining the positive effects from the ball-milling and doping procedure.[101]

It is also important to note that not all carbon supports benefits of a ball milling procedures: a study of Proietti and coworkers demonstrated that the same procedure applied to commercial carbons Black Pearls 2000 (BP2000), commercial N234 or N650 leads to ORR performance improvements for the BP2000 but not for the other two carbon supports.[102]

3.2 Materials

Tea leaves and coffee residues were recovered after preparation of the beverage. Before the pyrolysis, they were dried at 105 °C for 72 h. Urea (>99%), potassium hydroxide (KOH, 99.0% purity) ethanol (≥99.8% purity), acetone (≥99.8% purity), Nafion®5 wt.% hydroalcoholic solution, and iron (II) phthalocyanine C32H16N8Fe (Fe-Pc, 90% purity) were purchased from Sigma-Aldrich. Nitrogen and oxygen gases were supplied in cylinders by SIAD with 99.999% purity. Ultrapure deionized water obtained from a Millipore Milli-Q system (resistivity >18 MΩ cm) was used for the experiments. All reagents were used as received without further purification. As a noble metal comparison, 20 wt.% Pt/C (HiSPECTM3000, Pt 20 wt.% on carbon black, Johnson Matthey) was purchased from AlfaAesar.

3.3 Synthesis of the catalysts

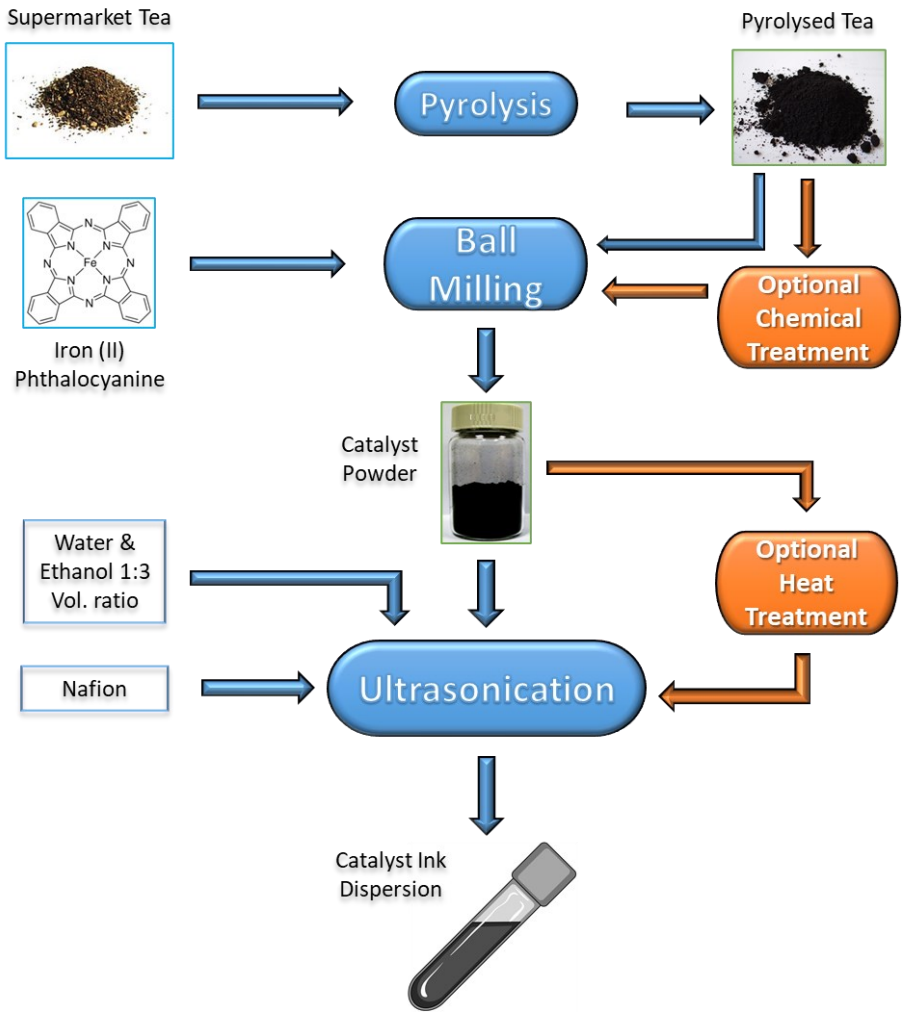

Figure 18: Schematic preparation of the Fe-N-C catalyst from starting materials to the ink deposition

Synthesis of the catalyst was done in two phases, first is the synthesis of the carbon-based support from the biomass, the second is the iron incorporation. Exhausted tea leaves (100 g) were pyrolyzed using a vertical furnace and a quartz reactor, heating rate of 15 C° min^{-1}, and kept at 400 °C for 30 min in a nitrogen atmosphere according to procedure developed by Noori et al. [103]. A further thermal annealing was run accordingly with previous described procedures, this was needed considering the parameters of the two different furnace employed [104,105]. Tea-derived biochar was treated by using a vacuum electric furnace (Pro.Ba., Cambiano, Italy) in an argon atmosphere, at a controlled pressure of 550 mbar, using a heating

rate of 150 °C h^{-1}. Once the target temperature (1500 °C) was reached, it was kept constant for 30 min. Subsequently, the furnace was cooled at room temperature with the same thermal gradient used for heating. The so-produced tea-derived biochar was labelled $C_{pyro\text{-}tea}$. Same procedure was repeated for coffee and sample will be labelled as $C_{pyro\text{-}coffee}$

The first treatment for $C_{pyro\text{-}tea}$ was with nitric acid: a sample of starting material was added to a solution of 5 M HNO_3 and heated to 60 °C for 30 minutes. Recovered sample was filtered, washed with water and labeled as $C_{nitro\text{-}tea}$ to be used without further treatment.

Afterwards, a sample of $C_{pyro\text{-}tea}$ was mixed in a ceramic mortar with urea with a 1:1 weight ratio and placed into a pre-heated tubular furnace (Carbolite TZF 12/65/550), where it was kept at 800 °C for 30 min in argon atmosphere. The sample recovered was labelled $C_{urea\text{-}tea}$ and used without any further treatment. Similarly, a sample of $C_{pyro\text{-}tea}$ was placed into a pre-heated in a tubular furnace (Carbolite TZF 12/65/550) and there kept at 800 °C for 30 min in CO_2 atmosphere (10 mL min^{-1}). The sample recovered was named $C_{CO2\text{-}tea}$ and used without any further treatment.

The different Fe-N-C catalysts were prepared via ball milling using pyrolyzed commercial tea and Fe-Pc as precursors, with the Fe-Pc as a unique source of both Fe and N. The Fe-N-C catalysts were obtained by high energy ball milling treatment using three stainless steel balls, each 8 mm in diameter, in a jar of 25 ml volume that vibrates at a frequency of 20 Hz for 99 minutes in a translational Mixer Mill MM 400 by Retsch. We introduced in the jar a 1:2 weight ratio mixture of Fe-Pc and the carbon supports derived by the pyrolysis of biomass, after verifying that this was the combination which provided the best performance in terms of ORR onset potential. Further considerations on this procedure will be explained in the next chapter.

The catalysts synthetized by ball milling were labelled Fe-N-$C_{pyro\text{-}tea}$, Fe-N-$C_{nitro\text{-}tea}$, Fe-N-$C_{CO2\text{-}tea}$ and Fe-N-$C_{urea\text{-}tea}$, respectively. There was no further treatment for the catalysts.

3.4 Physical Characterization

The morphology of the catalysts was investigated using a Field Emission Scanning Electrical microscope (FE-SEM, Zeis SupraTM 40) equipped with an energy dispersive X-Ray analyzer (EDX, Oxford Inca Energy450).

TEM investigations were performed at the Microscopy Platform of the University of Milano-Bicocca (Italy) using a JEOL JEM 2100P operating at 200 kV, equipped with a LaB6 source, and exhibiting a nominal point resolution of 2.4 Å. The images were then recorded with a Gatan RIO CMOS camera. The synthesized samples were dispersed in a solvent and transferred via drop casting onto a Cu grid, covered with a thin (3-4 nm) amorphous Carbon membrane. Images were taken at room temperature at different magnifications, with the TEM operated in bright-field parallel imaging mode, and adopting an in-gap objective aperture. Chemical analysis was performed using an Oxford Energy Dispersive X-Ray (EDX) detector while the microscope was operated in Bright-Field (BF) and High Angle Annular Dark-Field (HAADF) Scanning TEM (STEM) mode.

XPS spectra were recorded by using a PHI 50 0 0 Versaprobe (Physical Electronics, Chanhassen, MN, USA) scanning X-ray photoelectron spectrometer (monochromatic Al K-alpha X-ray source with 1486.6 eV energy, 15 kV voltage, and 1 mA anode current). Origin software was used to deconvolute the narrow spectra and determine the relative Fe-, N-, O-, and C-type atomic composition, using Gauss line shape with a Shirley background.

Raman spectra were collected using a Renishaw inVia (H43662 model, Gloucestershire, UK) equipped with a green laser line (514 nm) with a 50× objective. Raman spectra were recorded in the range from 250 to 3,500 cm^{-1}.

XRD of powdered samples was conducted using Rigaku Miniflex 600 equipped with a copper source. Analysis was performed in the 2θ range of 10-90° with a step of 0.020° while the scanning speed was 1.000 °/min.

The specific surface area of the samples was measured by means of N_2 adsorption/desorption at –196 °C on a Micrometrics ASAP 2020 Plus version 1.03 instrument (Micromeritics Instrument Corporation, USA). Before the analysis, the samples were degassed under vacuum for 3 h at 150 °C. The Brunauer–Emmett–Teller (BET) model was applied for data analysis. The volume of the micropores, along with the differential surface area distribution, was obtained using a Non-Local Density Functional Theory (NLDFT) model calculation included in the Micromeritics instrument software.

The iron weight percentage in the Fe-N-C catalysts was determined by inductively coupled plasma optical emission spectroscopy (ICP-OES) with a ICP-OES Optima 7000 DV PerkinElmer instrument. Prior to analysis, 20 mg of each

powder were acidified in a 4 ml of HNO_3 and 1 ml of H_2O_2 and digested in two steps at 1000 W each, 20 + 30 min each (220 °C).

3.5 Electrochemical Characterization

3.5.1 Cyclic Voltammetry

Cyclic voltammetry is a potentiodynamic technique commonly used in electrochemistry to analyze and investigate the nature of redox reactions. The technique involves the use of a potentiostat to first oxidize and then reduce an electrode at a linear scan rate measuring at the same time the corresponding current. A rotating disk electrode can be used to ensure a well-mixed environment, albeit measures are usually conducted without rotation. Without rotation, mass transport of the analyte to the electrode surface occurs by diffusion alone meaning diffusion coefficient, distance from the electrode, and concentration of reactant are important(Fick's Law). In a stirred solution, a narrow diffusion layer lies adjacent to electrode surface surrounded by turbulent flow region containing the bulk solution. Because of this, the reacting analytes cannot diffuse into the bulk solution and a Nernstian equilibrium is maintained.

The scan rate is an important consideration for the CV: faster scan rates lead to smaller diffusion layers and higher currents. The curve obtained from the measurement is known as a cyclic voltammogram (also denoted by CV). CV measurements can be used to determine the presence of particular chemical species due to characteristic peaks on the resulting CV indicating oxidation or reduction reactions. In the case of a platinum catalyst, the curve can be integrated to determine the electrochemical surface area[106,107]

For non-noble catalysts, the CV is used visually to indicate the presence of key components such as iron. In order to obtain useful information about the activity of the catalyst, staircase cyclic voltammetry must be performed. It is also possible to use the CV curve to obtain capacitance and ECSA values by integration of the area of the plot.

3.5.2 Staircase Voltammetry and the RDE Polarization Curve

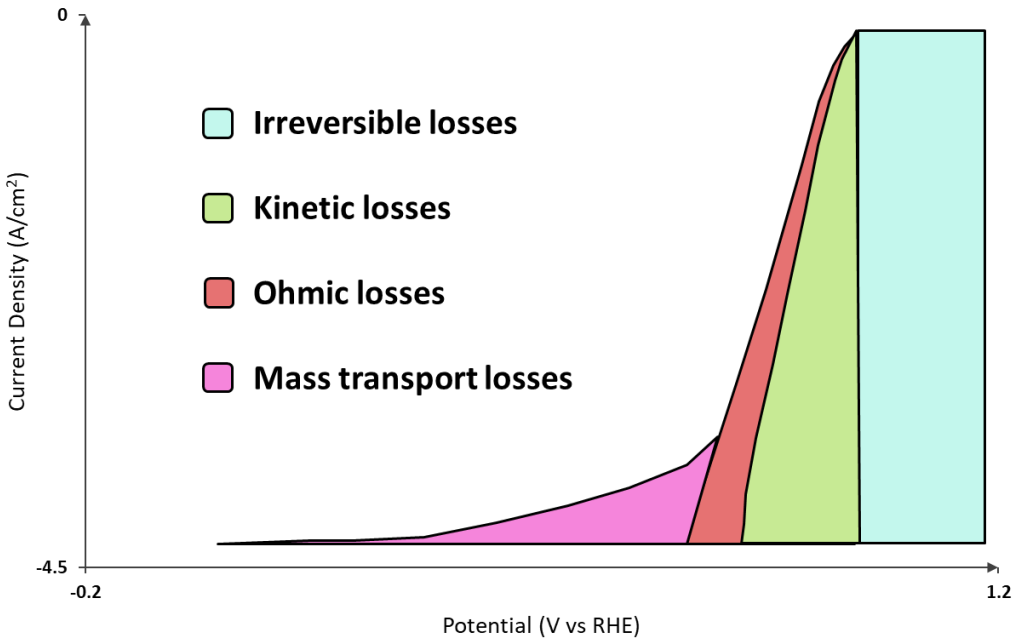

Figure 19: Different current losses in a RDE polarization curve

The staircase voltammetry is an alternative to usually employed linear sweep voltammetry, and they both perform the same type of measure which is a gradual increase in potential while measuring the corresponding current. While LSV employs a linear increase (as suggested by the name), SV measurement is performed by a stepwise increase in potential followed by a relaxation time where the system is allowed to equilibrate before the actual measure of the current. Unlike linear sweep voltammetry – where there is no relaxation period – the SV technique can account for capacitive effects and give more accurate information about the overpotentials in the system. The overpotential is a measure of how an electrochemical process deviates from the ideal conditions because of different limitations such as kinetics, mass transport and internal resistances. Figure 19 shows the polarization curve for a Pt-C catalyst obtained through staircase voltammetry analysis in a rotating disk electrode system with the aforementioned contributions highlighted. The IUPAC convention is used in this work meaning the reduction corresponds to a negative current.

The potential measured in a RDE system is the result of the equilibrium between species undergoing oxidation and reduction at an electrode surface. The

open circuit voltage of a fuel cell system – i.e. potential when no current is flowing – is lower than theoretical voltage due to irreversible losses arising from species crossover and internal currents as well as kinetic losses. As the current density increases in magnitude, the voltage drops further due to a combination of losses from a range of sources – these overpotentials can be minimized through appropriate selection of materials and operating conditions. At low current densities, the kinetic losses dominate; this is the result of the activation energy required to initiate the chemical reaction at the electrode surface. This is the main area of interest for this report and will be discussed in more detail in the next section.

Increasing the current density results in ohmic losses which are caused by the intrinsic charge transport resistances in conductors, albeit for RDE analysis usually these losses are minor compared to others. These losses can be either electrical or ionic. As ion transport is inherently more difficult, this is usually the greater source of ohmic losses in a fuel cell system. Lastly, at high current densities, mass transport limitations begin to take effect due to concentration polarization at the catalyst surface.

In our measure, in order to quantify and compare the ORR activity we adopt two commonly used parameters, namely the onset potential (E_{on}) and the half-wave potential ($E_{1/2}$). E_{on} has been defined in some relevant literature works as the potential required to generate a current density of 0.1 mA cm^{-2} in a steady-state RDE experiment, and that definition will be the one assumed in this work [108]. $E_{1/2}$ is usually defined as the potential where half the maximum current density in the polarization curve is measured.

Moving to a fuel cell system, these considerations change considerably as the current density is higher. Considering no real fuel cell tests were conducted on this study, the analysis will be limited to RRDE tests.

3.5.3 Butler-Volmer Kinetics and the Tafel Approximation

Butler-Volmer kinetics relates the current density (j) to the activation overpotential (η) arising from the charge transfer energy barrier in an electrochemical reaction. The Butler-Volmer equation is shown below (equation 5):

$$j = j_0\left(\frac{C_R^*}{C_R^o} e^{\left(\frac{\alpha n F \eta}{RT}\right)} - \frac{C_P^*}{C_P^o} e^{-\left((1-\alpha)\frac{nF\eta}{RT}\right)}\right) \quad (5)$$

where j_0 is the exchange current density which indicates how readily the reaction takes place; α is the charge transfer coefficient which varies depending on the activation barrier symmetry; C^* denotes a surface concentration; C^o denotes a bulk concentration; subscripts R and P refer to reactant and products respectively.

$$\eta = -\frac{RT}{\alpha nF} ln\, j_0 + \frac{RT}{\alpha nF} \ln j \tag{6}$$

The Tafel equation is a useful approximation of the Butler-Volmer equation at high overpotentials. Firstly, it is assumed that the net reaction rate has no effect on the concentration of products and reactants at the electrode. As the overpotential increases, the term on the right will tend towards zero which results in the following expression (equation 7) after simplifying:

The Tafel plot can be attained by plotting η vs $\log_{10}$ (j) in the form of

$$\eta = a + b \log j \tag{7}$$

where a is the intercept which is related to j_0 and b is the Tafel slope, an important parameter - related to α – which can give meaningful information about the reaction mechanism. Reaction conditions such as the potential can cause a significant change in electrode surface morphology and intermediate concentrations resulting in a change in mechanism; the change in Tafel slope provides a good indicator for a switch in mechanism and hence rate-determining step (RDS). For the ORR, a Tafel gradient of -60 mV/dec indicates that a pseudo $2e^-$ reaction is the RDS. A steeper gradient of -120 mV/dec corresponds to the first-electron reduction of oxygen as the RDS [22].

3.5.4 RRDE instrumentation and methods

The catalysts were electrochemically characterized in a three electrode cells. The cell was equipped with a with (i) a glassy carbon disk (and platinum ring) working electrode (disk diameter 4 mm, ring outer and inner diameters 7 and 5 mm, respectively), which was mounted on a rotating disk electrode (RDE) equipment (model RRDE-3A ALS, Japan), (ii) a saturated calomel electrode (SCE) for RRDE measurements, or a saturated Ag/AgCl reference electrode for RDE durability measurements, (iii) a gold wire counter electrode. For the electrochemical tests, the

potential of the working electrode was controlled by a potentiostat (Bio-Logic SP-150, France). The electrolyte was a 0.1 M KOH aqueous solution, pH = 13.

All measured potentials were corrected and converted to potential versus reversible hydrogen electrode (RHE) according to the following equation

$$E_{RHE} = E_{ref} + 0.059 \cdot pH + E^0_{ref} \quad (8)$$

where E_{ref} is the measured working potential versus the reference electrode, E^0_{ref} is the potential of the reference electrode respect to the standard hydrogen electrode at 25 °C (0.197 V for Ag/AgCl, 0.241 V for SCE). The electrodes were calibrated just once against reversible hydrogen electrode (RHE) before carring all the tests obtaining the aforementioned values. All of the current densities were thus normalized per geometric area of the electrode. The inks deposited onto the working electrode disk were prepared with a slightly modified version of a previously used method [109,110]. The inks were obtained by mixing 10 mg of catalyst powder with 33 µl of Nafion 5 wt.% solution (achieving a 0.1456 ratio of mg Nafion / mg sample) and 750 µl of a mixture of water and ethanol in a 1:3 rate, resulting in a catalyst density of in the ink equal to 0.0127 mg μl^{-1}. The ink was sonicated at 130 W for 30 min to achieve a good dispersion and 4 µl was pipetted on the glassy carbon electrode (area 0.1256 cm^2) obtaining a catalyst loading on the electrode of 400 µg cm^{-2}. For the benchmarking tests using platinum, the amount of water-ethanol solutions was adjusted in order to reach a loading of 30 µg Pt cm^{-2} as suggested by the literature [111]. Before starting the tests, each catalyst was subjected to 20 cyclic voltammetry (CV) between 0.0 and 1.2 V vs. RHE at 100 mV s^{-1} under N_2-saturated electrolyte to obtain a clean and stable catalyst surface. Then, a CV at 10 mV s^{-1} under N_2-saturated electrolyte was recorded.

Capacitance was obtained by integrating the area of the CV curve in the faradic zone, where the current was positive. The equation used is the following, as reported in literature[100,112]:

$$C_s(Fcm^{-2}) = \frac{\int_{E1}^{E2} j dV}{v\,(E1-E2)} \quad (9)$$

Integration was obtained with the trapezoid method adding consecutive area of small trapezoids where the two bases are the values of y_1 and y_2 while the height was the step between x_1 and x_2 repeated for all the available data points.

The ORR polarization curves were measured performing a series of linear sweep voltammetry (LSV) at variable rotating speed of the RRDE (from 300 to 2,000 rpm). The electrolyte was purged with O_2 for at least 30 minutes before the experiments for facilitating the saturation of the liquid solution. The potential was scanned from 1.2 to 0 V vs RHE. For the evaluation of the hydrogen peroxide yields and the calculation of the number of electrons, the rotation speed of the electrode was set to 900 rpm, and the potential of the ring was fixed at 1.2 V vs RHE along with the experiments. The current generated by the disk (I_d) and by the ring (I_r) were recorded, where the collection efficiency (N) was 38%. I_d and I_r were used to calculate the hydrogen peroxide produced ($\%H_2O_2$) (eq. 1) and the number of electrons transferred (n) (eq. 2) following the equations:

$$H_2O_2 = \frac{200 \cdot I_r/N}{I_d + I_r/N} \ [\%] \tag{10}$$

$$n = \frac{4 \cdot I_d}{I_d + I_r/N} \ [nr] \tag{11}$$

To quantify and compare the ORR activity we use two commonly used parameters, namely the onset potential (E_{on}), usually defined as the potential required to generate a current density of 0.1 mA cm^{-2} in a steady-state RDE experiment [108], and the half-wave potential ($E_{1/2}$), typically defined as the potential where half the maximum current density in the polarization curve is measured. As a term of comparison for ORR activity, we also used the mass activity of the catalysts, calculated at 0.9 V vs RHE using the kinetic current J_k, to avoid the effects of the mass transport limitations [113]:

$$M.A. = -\frac{J_{k(0.9)}}{m_{cat}} \ [A \cdot g^{-1}] \tag{12}$$

$$J_{k(0.9)} = -\frac{J_{lim} \cdot J_{(0.9)}}{J_{lim} - J_{(0.9)}} \ [A \cdot cm^{-2}] \tag{13}$$

where m_{cat} is the catalyst loading on the RDE, $J_{k(0.9)}$ is the mass transport-corrected current density at the selected voltage, J_{lim} is the diffusion limiting current density measured in the plateau region of the polarization curve at high overpotential, and $J_{(0.9)}$ is the measured current density at the selected voltage.

The methanol tolerance of the catalysts was evaluated in an O_2-saturated 0.1 KOH M solution, adding methanol to the solution from 0.001 to 2 M. LSV

measurements were performed at each MeOH concentration, with an RDE speed of 900 rpm at 5 mV s^{-1} scan rate, room temperature.

A series of dynamic tests was performed to check the stability of the catalyst to potential cycling. The tests followed two different protocols derived from a test proposed during the Fuel Cell Commercialization Conference of Japan (FCCCJ) in 2011 [114], one involving a repeated cycling between 0.4 and 1.0 V vs. RHE (scan rate 500 mV s^{-1}) and the other involving repeated cycling between 0.4 and 1.0 V vs. RHE with a faster scan rate (1,000 mV s^{-1}) and 3 s hold at these two potentials. The cycling was performed under O_2-saturated electrolyte conditions [115], instead of N_2-saturated electrolyte conditions [114]. ORR steady-state polarization curves were recorded at the beginning of the test, after 1,500 cycles, and at the end of the test (4,500 cycles) to monitor the degradation of the activity of the catalysts, performing a staircase voltammetry (SV) with a potential step of 10 mV and a holding time of 30 s in O_2-saturated electrolyte, at room temperature. A third protocol to evaluate the stability of the catalysts was performed through a chronoamperometry test performed in an O_2-saturated 0.1 KOH M solution keeping the potential fixed at 0.6 V vs RHE for 5,000 seconds.

Chapter 4

Preliminary testing

4.1 Electrochemical Characterization: RDE tests

As a first screening, tea and coffee were both selected for testing. After revising literature, it was our opinion that the synthesis we wanted to carry was a combination of pyrolysis and ball milling. First tests showed coffee to be not enough active compared to tea and for that reason was set aside for the rest of the work, focusing only on optimization and characterization of tea derived materials.

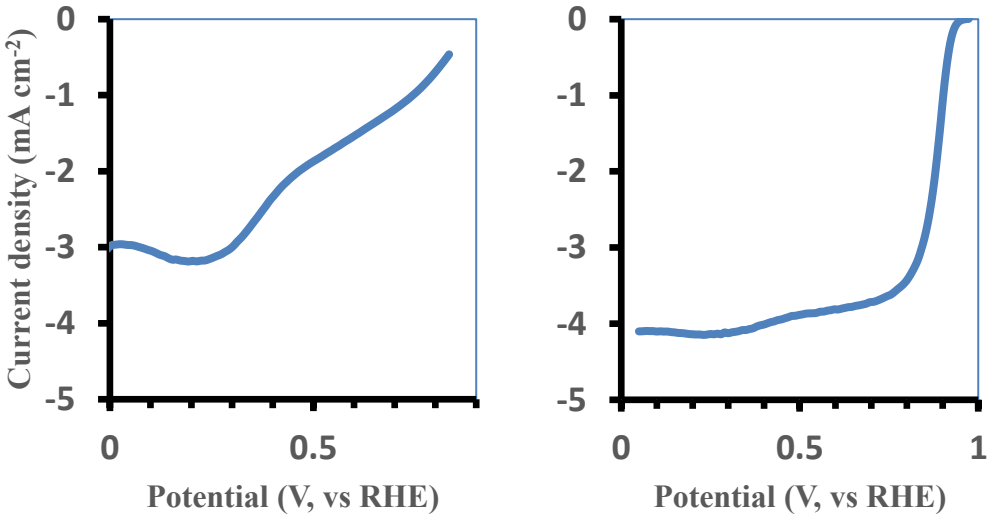

Figure 20: SCV in KOH 0,1 M, scan rate 1 mV s^{-1}; loading 0,4 mg cm^{-2} of sample Fe-N-$C_{pyrocoffee}$ (left) and Fe-N-$C_{pyrotea}$ (right), rotation speed 900 rpm

The electrochemical activity of the Fe-N-C catalysts synthetized from pyrolized tea leaves and various treatments was tested in both alkaline and acidic medium but only the alkaline results are discussed because the low activity showed in acidic medium is considered a proof of impossible application for

proton exchange membrane FC and any further consideration would only lead to a dead end.

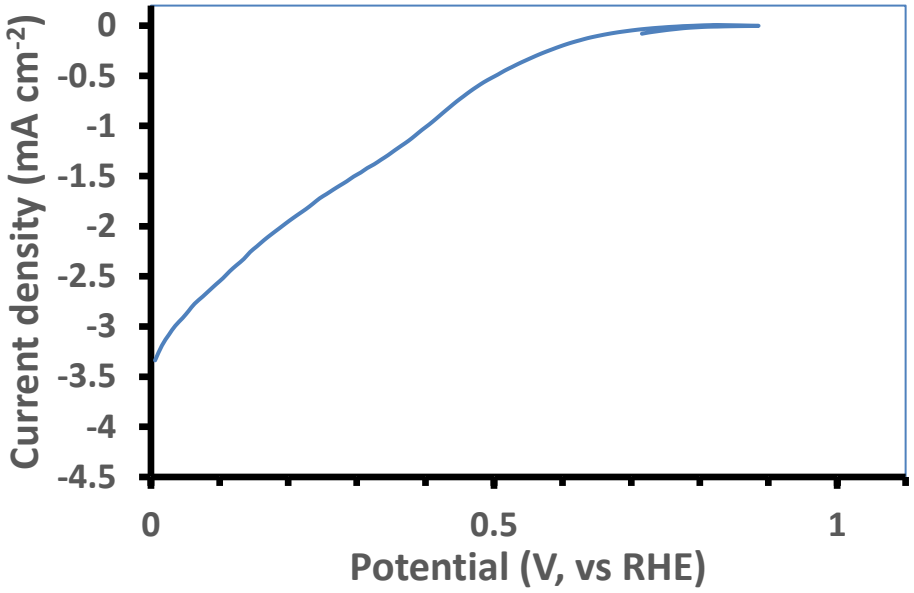

Figure 21: SCV plot of Fe-N-$C_{pyrotea}$ in $HClO_4$ 0.1 M, scan rate 1 mV s^{-1}; loading 0.400 mg cm^{-2}, rotation speed 900 rpm

Activity of the starting precursors was tested and is shown in figure 22. As expected, the $C_{pyro\text{-}tea}$ has practically no ORR activity, while the Fe-Pc has very limited ORR activity. Both tests were still necessary because of the high number of works published with claims that metal free catalyst and iron complex possess intrinsic ORR catalytic activity, while in our tests it was clear that the activity did not derive from starting materials only but from the combinations and synergy of them.

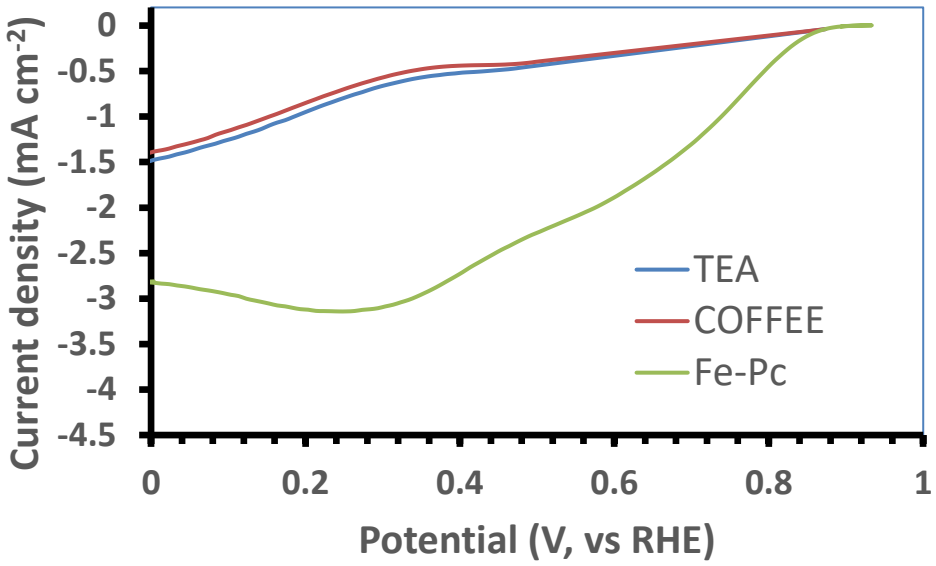

Figure 22: SCV plot of starting materials in KOH 0.1 M, scan rate 1 mV s^{-1}; loading 0.400 mg cm^{-2}, rotation speed 900 rpm

Optimization of the synthetic procedure of the Fe-N-C catalysts in terms of ratio of carbon-to-iron in Fe-N-C catalyst was done by performing different tests for $C_{pyrotea}$ with different rates of FePc : Carbon support. Three $C_{pyro\text{-}tea}$-to-Fe-Pc (4:1; 3:1; 2:1) was tried, and the best option was the weight ratio 2:1 (**Figure 23**).

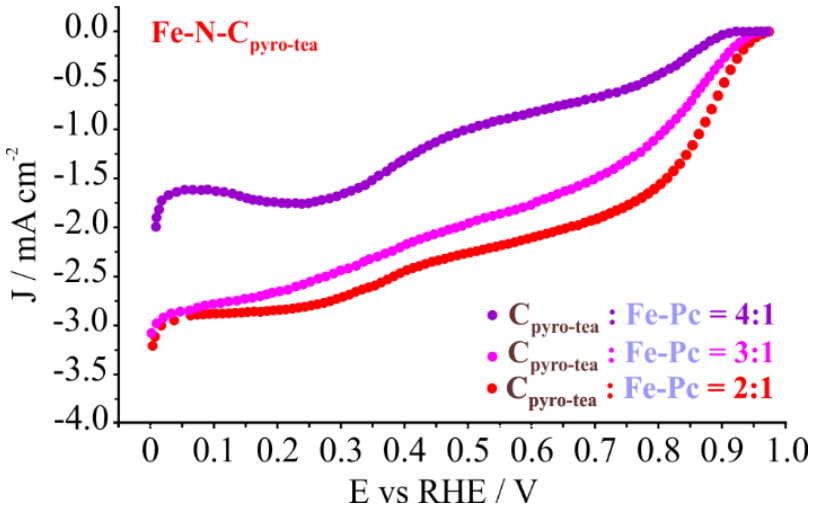

Figure 23: SCV curves of different $C_{pyro\text{-}tea}$: Fe-Pc ratios (2:1 / 3:1 / 4:1) in the translational mixer for ball milling: recorded in RDE at room temperature, in N_2-saturated 0.1 M KOH solution, scan rate 10 mV s^{-1}, electrode loading 400 µg cm^{-2}. $C_{pyro\text{-}tea}$ + Fe-Pc amount = 200 mg. Milling time: 99 min, rotation speed 900 rpm

We also noticed that the best performance was obtained by filling the jar with 200 mg of sample. We consider this as a consequence of the energy involved in the ball milling, different amount of sample leads to different behavior towards grinding and heating. A more complex and systematic study would be desired to confirm this hypothesis but due to time constrictions, only a general screening was possible. **(Figure 24)**

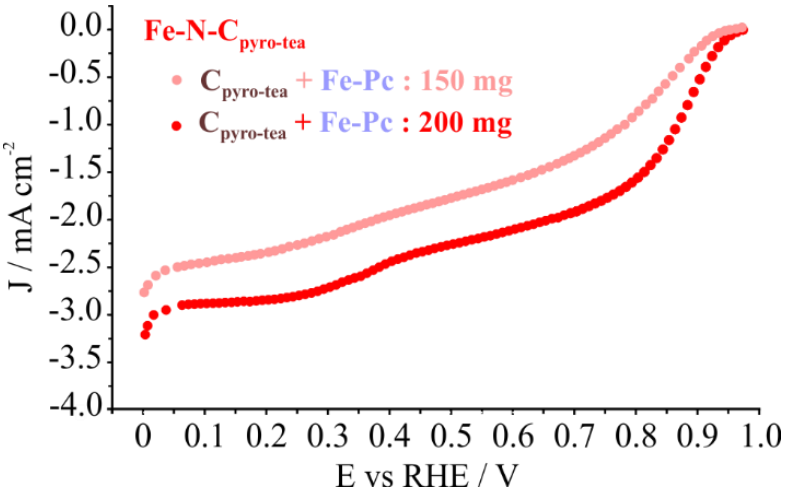

Figure 24: SCV plot of Fe-N-$C_{Pyrotea}$ Fe:C rate 1:2 with different filling of the jar, recorded in KOH 0.1 M, scan rate 1 mV s^{-1}; loading 0.400 mg cm^{-2}, rotation 900 rpm

For the ball-milling time, 99 min was selected *a priori* without optimization as it was the maximum time allowed by the translational mixer. It is considered a sufficiently long mixing time compared to other works [116–118], where optimized time is considered around 90-100 min to assure a good degree of pulverization without losing porosity. According to the literature longer milling times are not recommended because they can produce a reduction of micro-and meso-porosity, not desired in fuel cell environment. Other properties guaranteed by the ball milling are homogeneity in the final product, a high volumetric and specific capacitance, enhanced ion-transportation within the pores.

Thus, all the presented Fe-N-C catalysts were synthesized by ball-milling for 99 minutes, 200 mg precursors in the jar, in the weight ratio C:Fe-Pc = 2:1.

Before presenting the comparison between the best catalyst, a specific discussion will include the test of Fe-N-$C_{nitro\text{-}tea}$ due to the peculiar characteristics of this.

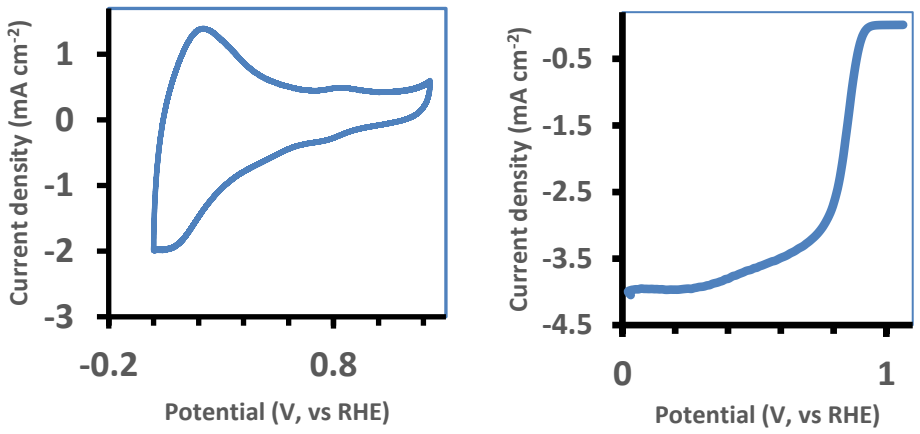

Figure 25: Fe-N-$C_{nitrotea}$: CV voltammogram (left) recorded in KOH 0,1 M; scan rate 10 mv s^{-1} SCV curve (right) recorded in KOH 0,1 M, scan rate 1 mV s^{-1}; loading 0,400 mg cm^{-2}, rotation speed 900 rpm

Figure 25 shows the CV and SCV of Fe-N-$C_{nitrotea}$, which was used as a reference for calculating electrochemical parameters. The interesting data was a worst performance compared to Fe-N-$C_{pyrotea}$ which is quite unexpected considering the treatment with nitric acid used to increase specific surface area and introduce nitrogen groups. Due to this strange behavior, we considered it aside from the

other three catalysts which will be further analyzed both in this paragraph and in the next chapters.

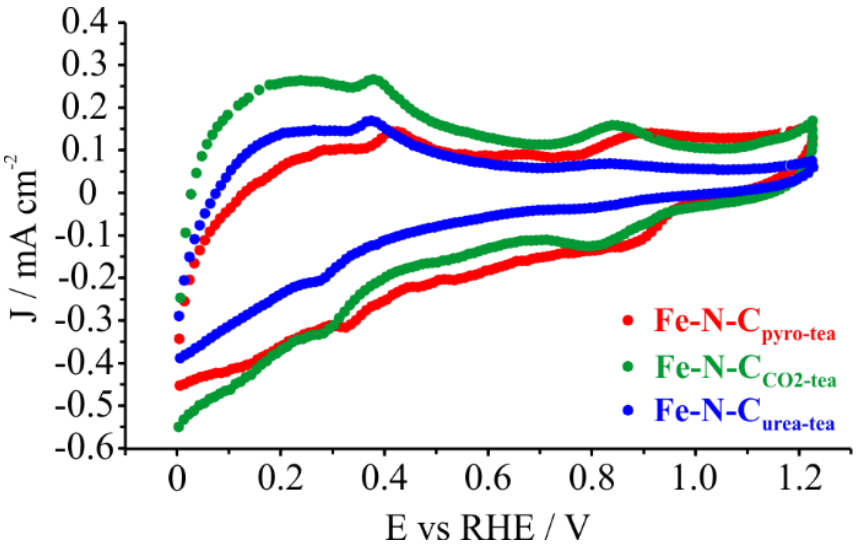

Figure 26: CV plot of best Fe-N-C catalysts. Recorded in KOH 0.1 M, scan rate 1 mV s^{-1}; loading 0.400 mg cm^{-2}

Figure 26 shows the CV of the three synthesized catalysts in N_2-saturated alkaline electrolyte. The shape of the cyclic voltammograms is quite similar for all the materials, showing very low peaks that could be attributed to the $Fe^{1+/2+}$ redox couple (0.25 V) and $Fe^{2+/3+}$ redox couple (range of 0.7 to 0.8 V) of the Fe-Pc although there is a considerable shift compared to the values from literature [39,119,120]. The peaks are located at 0.33 V vs RHE and 0.84 V vs RHE for the Fe-N-$C_{CO2\text{-}tea}$ and Fe-N-$C_{ureatea}$, while the peaks of the Fe-N-$C_{pyro\text{-}tea}$ appear to be at a slightly higher potential probably due to the environment change. Therefore, it's our hypothesis that those peaks are coming from the carbon surface redox-active moieties (like quinones-hydroquinones). In these catalysts these peaks are clearly visible because the mixture biochar Fe-Pc is only ball milled, and not pyrolyzed (as most of the Fe-N-C catalysts in the literature, which usually present

a smoother line). This testifies the analogous electrochemical properties of the catalysts, which are expected considering the similar starting materials. The shape is quite different compared to a Pt/C plot, that is because the different mechanism involved and different peaks. The specific capacitance appears to be high for all the catalysts, with the capacitive current values slightly higher for the Fe-N-$C_{CO2\text{-}tea}$. This also demonstrates one benefit of the activation of the biochar with CO_2 providing a catalyst with higher specific capacitance compared to the other three.

The calculation of specific capacitance was performed for the three catalysts leading to the values of 0.009029 Fcm^{-2} for Fe-N-$C_{pyro\text{-}tea}$, 0.01779 Fcm^{-2} for Fe-N-$C_{CO2\text{-}tea}$, 0.008794 Fcm^{-2} for Fe-N-$C_{ureatea}$ while the mass capacitance values, obtained by multiplying for electrode area and dividing by mass of catalyst at electrode interface, are 11.3 Fg^{-1} for Fe-N-$C_{pyro\text{-}tea}$, 22.3 Fg^{-1} for Fe-N-$C_{CO2\text{-}tea}$, 11.0 Fg^{-1} for Fe-N-$C_{ureatea}$, which are slightly lower but definitely comparable to other non noble metal catalysts.[121]

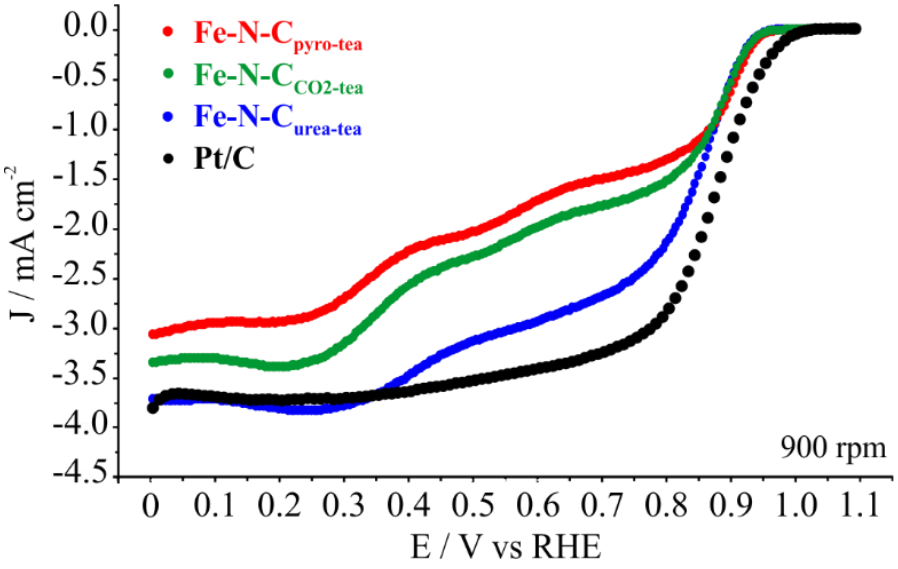

Figure 27: SCV curves of Fe-N-C catalysts Recorded in O_2-saturated KOH solution 0.1 M, rotation speed 900 rpm, scan rate 1 mV s^{-1}; loading 0.400 mg cm^{-2}

Figure 27 shows the ORR activity results for the four Fe-N-C- catalysts from the SV, comparing with a commercial Pt/C. A measure in steady-state conditions (staircase voltammetry) allows the polarization curves to avoid capacitive current contribution. Onset and halfwave potentials, as well as mass activity, are summarized in **Table 1**

Table 1: mass activity (M.A.), onset potential (E_{onset}) and half-wave potential ($E_{1/2}$) of the materials prepared related to the ORR measurements in Figure 27.

	M.A. @ 0.9 V **[A g^{-1}]**	**E_{onset}** **[V vs RHE]**	**$E_{1/2}$** **[V vs RHE]**
20 wt% Pt/C	38.36 ± 9.24	0.99 ± 0.01	0.89 ± 0.01
Fe-N-$C_{pyro\text{-}tea}$	2.32 ± 0.37	0.94 ± 0.01	0.89 ± 0.01
Fe-N-$C_{nitro\text{-}tea}$	0.5 ± 0.27	0.93 ± 0.02	0.83 ± 0.02
Fe-N-$C_{CO2\text{-}tea}$	2.98 ± 0.24	0.95 ± 0.01	0.89 ± 0.01
Fe-N-$C_{urea\text{-}tea}$	2.31 ± 1.10	0.93 ± 0.01	0.89 ± 0.01

According to these results, the best performing catalyst appear to be Fe-N-$C_{CO2\text{-}tea}$ followed by Fe-N-$C_{urea\text{-}tea}$, although the mass activity is significantly lower than Pt/C. It's worth noting the high deviation of Fe-N-$C_{urea\text{-}tea}$ which is difficult to explain and only possibility is the large time gap between different tests which may have brough the catalyst to aging. Even if mass activity is lower, E_{onset} and $E_{1/2}$ are quite similar to Pt/C, which is quite valuable considering the enormous difference in cost of the starting materials between the species. The better behavior of Fe-N-$C_{CO2\text{-}tea}$ is expected due to the high pore volume and more ordered carbon structure. It is interesting to note that both CO_2 and urea treatment that followed the starting pyrolysis of the tea leaves allowed the generation of two slightly more performant catalysts compared with the Fe-N-$C_{pyro\text{-}tea}$. Only nitrotea has worse performance than starting pyrotea support. As a comparison with other biomass derived catalysts from the literature, it is worth noting that there are a large number of reported catalyst but the vast majority of them falls in the range of 0.80-1.00 V for the onset potential and 0.70-0.95 V for the half-wave potential, in 0.1 KOH electrolyte [122–124]. Mass activity values are almost never reported in the literature. Also, acidic data are rarely presented as the activity for these materials tends to become much lower in low pH environment as is the case of our catalysts.

4.2 Specific Surface Area measurements

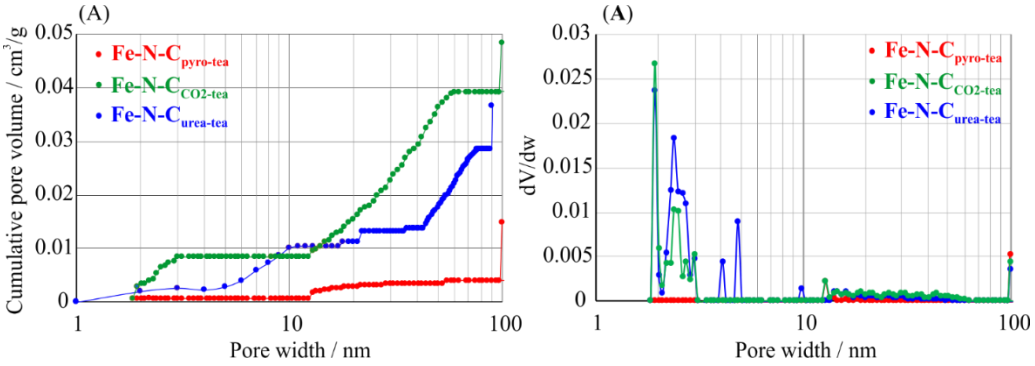

Figure 28: Cumulative pore volume (A) and dV/dw pore volume (B) for the three best Fe-N-C electrocatalysts according to the N_2 @ 77 K on Carbon Slit Pores NL-DFT model by Micromeritics software.

To verify the efficiency of the treatments, BET analysis was performed on the sample and the specific surface area test of all Fe-N-C catalyst is reported in table 2. The ball milling procedure increased the area of pristine tea derived biochar but only with the CO_2 treatment it reaches values above 50 m^2/g. with pore volume that are not significantly different compared to pristine tea derived biochar. It is interesting to note that the Fe-N-$C_{nitrotea}$ has a SSA even lower than starting Fe-N-$C_{Pyrotea}$, meaning something in the process of HNO_3 treatment failed and pore formed with the acid treatment tend to collapse instead of remaining stable. This was one of the reason that lead us to exclude the nitrotea synthetic route from further tests.

Table 2: Specific surface area and pore volume of pristine tea derived biochar, and different Fe-N-C catalysts.

Support	Specific surface area (m^2/g)	Pore Volume (cm^3/g)
Pristine tea derived biochar	<1	0.0369
Fe-N-$C_{pyro\text{-}tea}$	4.50	0.0098
Fe-N-$C_{nitro\text{-}tea}$	<1	0.0040
Fe-N-$C_{CO2\text{-}tea}$	51.1	0.0383
Fe-N-$C_{urea\text{-}tea}$	31.7	0.0542

4.3 Observations

Testing of both tea derived and coffee derived material showed very quickly that only one of them was worth analyzing. The difference in starting tests prompted us to focus only on tea leaves derived materials and trying to functionalize them with three different procedures. Again, the electrochemical tests allowed us to rule out one of the processes because of the low value of the produced materials. The fact that Fe-N-$C_{nitrotea}$ was outclassed even by Fe-N-$C_{pyrotea}$ was a proof for us of a underperforming material and a not optimal procedure. Our hypothesis was that it was a consequence of pore collapse after nitric acid treatment but even, so it was our choice to not continue the testing on that material and rule it out as a failed try. The remaining Fe-N-C catalysts, namely Fe-N-$C_{pyrotea}$ Fe-N-C_{CO2tea} and Fe-N-$C_{ureatea}$ were instead deemed worthy of subsequent analysis, which include more specific physical characterization and electrochemical measurements of peroxide production, stability, and durability. It's worth to mention that these further analyses take time and were sometimes carried out by different group, that was another reason for us to focus only on the best performing materials instead of

wasting time (and money) in further analyzing dead ends. More specifically, we are interested in the confrontation between Fe-N-C_{CO2tea} and Fe-N-$C_{ureatea}$ while Fe-N-$C_{pyrotea}$ will be used as a mean of confrontation, just like Pt-C commercial catalyst, but will be kept out of certain analysis due to time and quantity of material constrictions.

Chapter 5

Characterization and discussion

5.1 Physical Characterization

Biochar obtained from pristine tea leaves is treated at high temperature in order to increase the conductivity as shown by several works [125–128]. Biochar goes through a reorganization process for temperature up to 1000 °C, as reported by Tagliaferro et al.[129], displaying good size in graphitic domains and crystallinity after an annealing at 1500 °C. It was also observed that high temperature treatments lead to a drastically reduction of both surface area, surface functionalities as well as pore volumes[130]. For this reason, we employed two different procedures in order to enhance specific surface area and nitrogen functionalities on biochar. The first treatment involves the pyrolysis of the biochar with CO_2 promoting both physical activation and introduction of oxygenated functionalities[131]. The other treatment was based on thermal decomposition of urea resulting in both nitrogen doping and increase of specific surface area as a consequence of the chemical activation[132].

A preliminary investigation of morphology and composition of the catalyst and of the biochar precursors was run through FESEM and EDX analysis as shown in figure 29 and table 3 respectively.

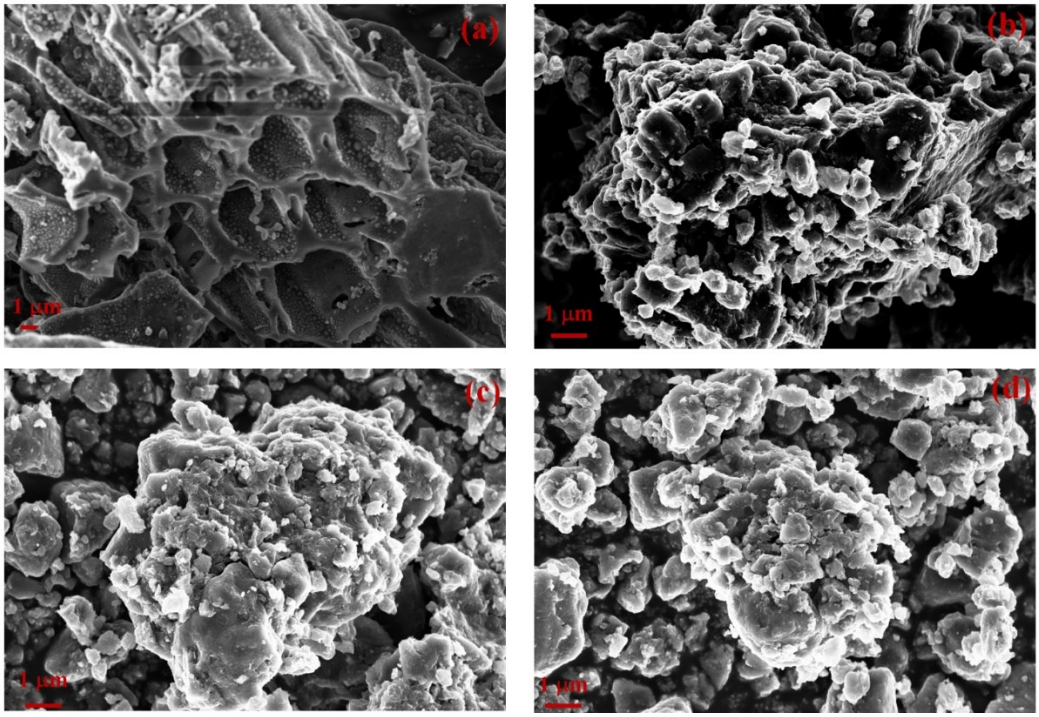

Figure 29: FESEM captures of a) pristine tea derived biochar, b) Fe-N-$C_{pyrotea}$, c) Fe-N-C_{CO2tea} and Fe-N-$C_{ureatea}$

FESEM image of pristine tea derived biochar describes a material retaining in a certain way the original biomass structure albeit deformed. The ball milling process induced a general homogenization of the morphology with the complete loss of the channeled structure[133]. This was probably due to the mechanical disruption induced by ball-milling. This procedure was able to insert the iron into the carbonaceous skeleton as shown later by EDX analysis. Iron content rise up to over 8 wt.% in the Fe-pyro tea while in both Fe-N-C_{CO2tea} and Fe-N-$C_{ureatea}$ it is close to 5 wt.%. Fe-N-$C_{ureatea}$ showed the higher carbon content among the catalyst prepared can suggest that urea decomposition removed other nitrogen heteroatomic doping elements.

Table 3: Elemental composition by weight obtained by EDX analysis of pristine tea derived biochar, Fe-N-$C_{pyrotea}$, Fe-N-C_{CO2tea} and Fe-N-$C_{ureatea}$. ICP-OES used to determine the iron content on Fe-N-C catalysts (last raw).

Element	**Sample**			
[wt.%]	$C_{pyro-tea}$	Fe-N-$C_{pyro-tea}$	Fe-N-$C_{CO2-tea}$	Fe-N-$C_{urea-tea}$
C	83.5	67.8	69.4	74.3
O	6.2	17.9	21.8	17.7
Al	0.6	0.6	0.4	0.6
Si	0.2	0.5	0.3	0.3
P	0.5	0.4	1.3	n.d.
K	6.1	2.7	0.8	1.3
Ca	2.0	1.8	0.8	0.9
Na	0.6	0.	0.4	n.d.
Fe	n.d.	8.3	5.3	4.9
Fe*	-	3.59	3.81	2.59

*Fe measured by ICP-OES

XPS analysis give further insight into the chemical structure of the catalysts prepared was provide by the XPS analysis reported in the figure 30 and figure 31. From the analysis of C1s, we can observe the presence of sp^3 carbon (around 284.2 eV) in Fe-N-$C_{pyrotea}$ and Fe-N-$C_{ureatea}$ while it is not present in the Fe-N-C_{CO2tea}. This is coherent with the predicted reaction pathway involved in the physical activation promoted by CO_2 [134] which depletes the non-graphitic carbon. Insertion of carbonyl

residues into graphitic carbon structure is confirmed by the increase of the peak at around 285.6 eV. As for nitrogen, there are two displayed signals that can be attributed to pyridinic (around 398.7 eV) and pyrrolic (around 400.1 eV) species. Fe-N-$C_{pyrotea}$ and Fe-N-C_{CO2tea} show a ratio of pyridinic/pyrrolic nitrogen of 0.6 and 0.3 respectively while Fe-N-$C_{ureatea}$ is characterized by a higher value close to 1.1. This was reasonably due to amine group inserted during the process that evolved into high stable aromatic nitrogen such as pyridinic species. It is interesting to note that even if the catalyst was prepared using Iron (II) phthalocyanine, in the products iron appears as both Fe(II) and Fe(III), which is reasonably as a consequence of a partial oxidation of original iron material. Fe-N-$C_{pyrotea}$ has the lowest oxygen content up to 55 % while Fe-N-C_{CO2tea} showed a much higher one with a Fe(II) amount of up to 78 % and Fe-N-$C_{ureatea}$ showed a value up to 68%. This suggest a lower stabilization of Fe(II) in Fe-N-$C_{ureatea}$ compared with Fe-N-C_{CO2tea}, which we can explain due to the random distribution of pyridinic nitrogen insert during the urea decomposition that probably does not reach the correct geometry for the stabilization of iron center while carbonyl residues in Fe-N-C_{CO2tea} could be create more stable complexes.

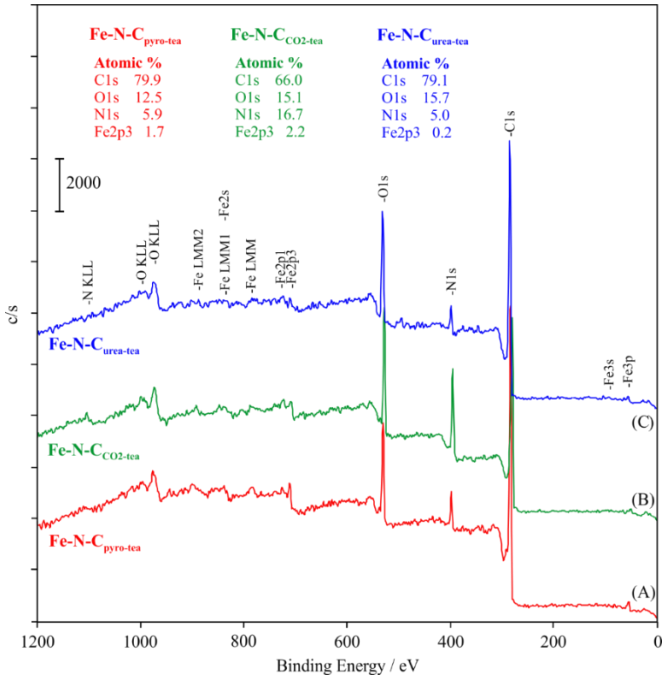

Figure 30: XPS survey spectra of Fe-N-$C_{pyro\text{-}tea}$ (a); Fe-N-$C_{CO2\text{-}tea}$ (b), and Fe-N-$C_{urea\text{-}tea}$ (c).

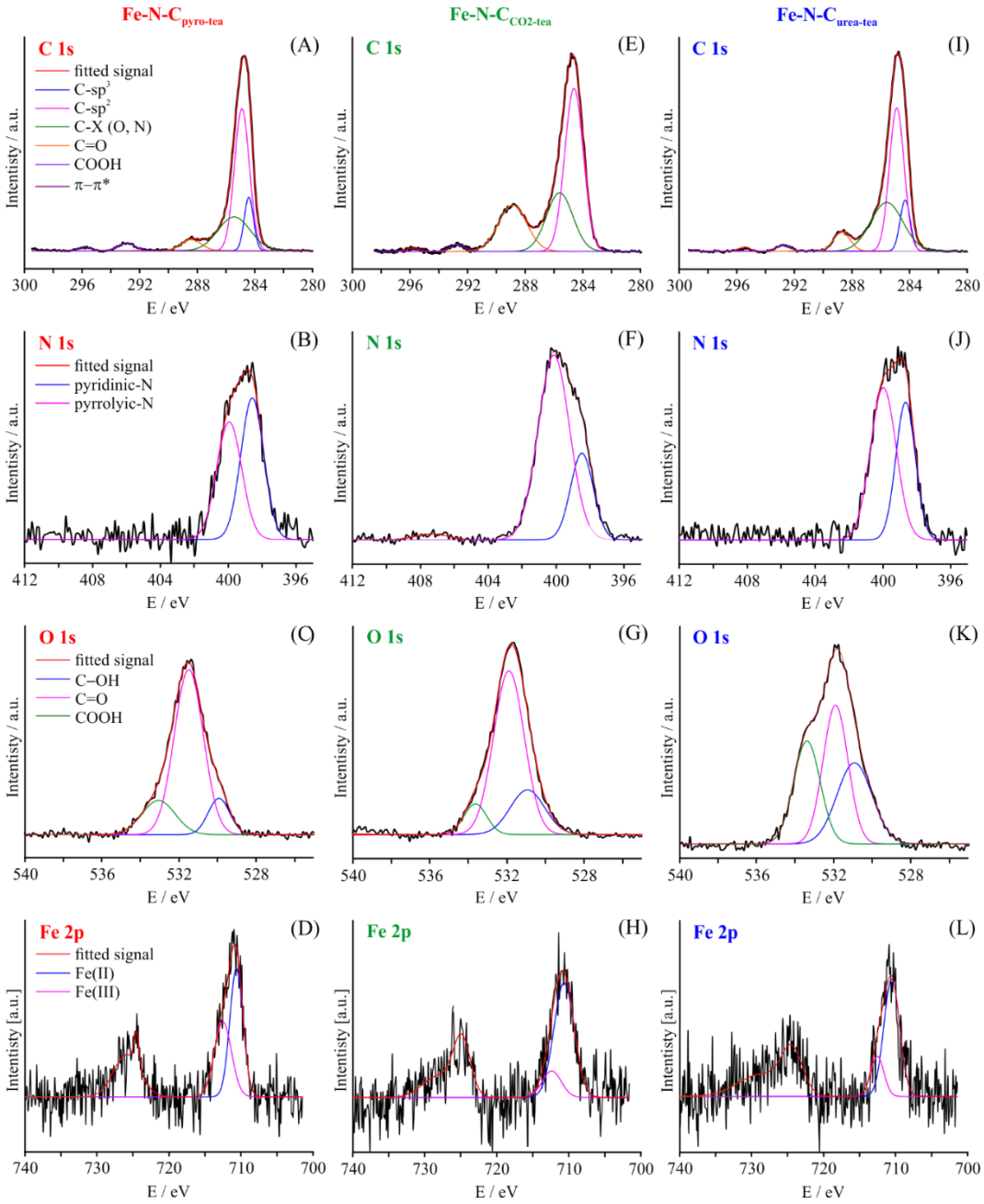

Figure 31: XPS spectra of a-d) Fe-N-$C_{pyrotea}$, e-h) Fe-N-C_{CO2tea} and j-l) Fe-N-$C_{ureatea}$. In picture are reported the signals of carbon, nitrogen, oxygen and iron

Raman spectra reported confirms the disorganization of the materials after ball milling with exception of the urea treated one. Fe-N-$C_{ureatea}$ shows an I_D/I_G value of up to 0.9 while the pristine tea derived biochar show a very close value of up to 0.8. This is reasonably due to the radical rich environment promoted by urea decomposition that induced a further enlargement of crystalline domains.

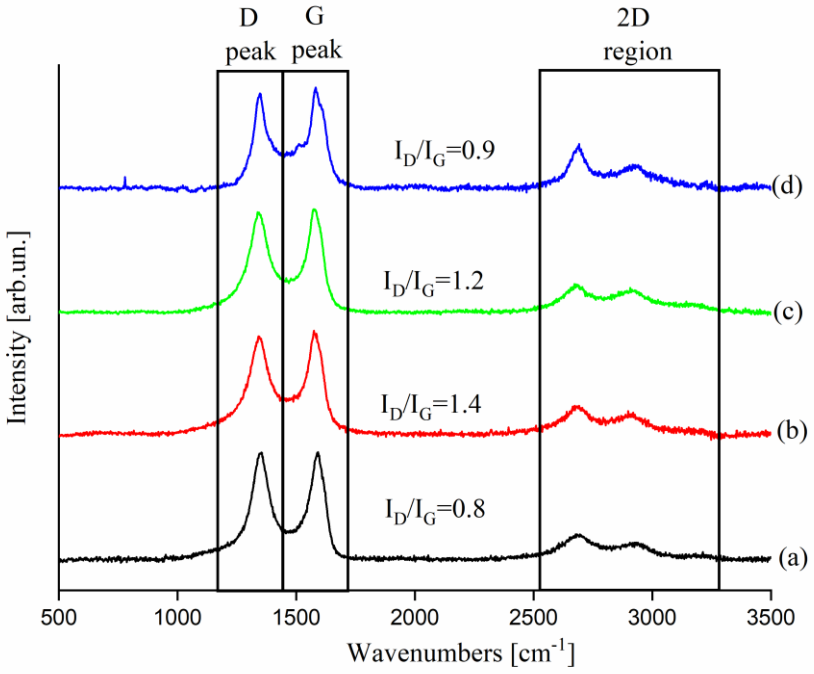

Figure 32: Raman spectra of a) pristine tea derived biochar, b) Fe-N-$C_{pyro\text{-}tea}$ c)Fe-N-$C_{CO2\text{-}tea}$, and d) Fe-N-$C_{urea\text{-}tea}$

5.2 XRD Tests

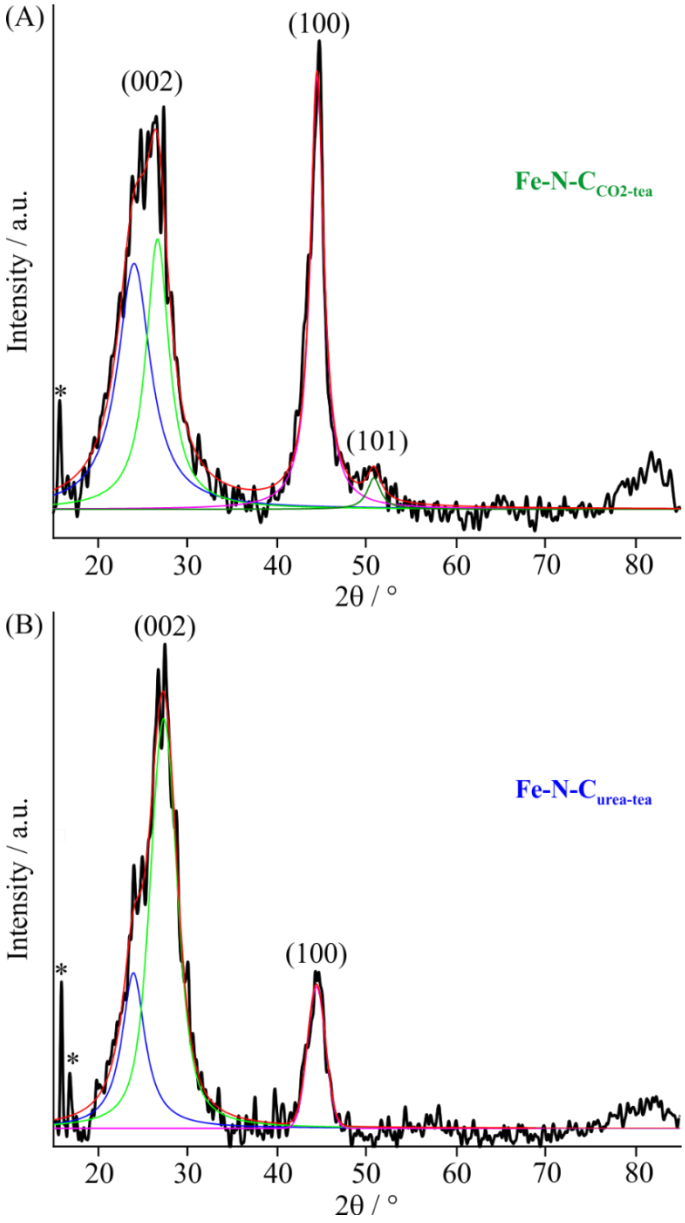

Figure 33: XRD spectra of Fe-N-$C_{CO2-tea}$ (A) and Fe-N-$C_{urea-tea}$ (B) from 15 up to 85 2θ. Peaks attributed to Fe_3O_4 are marked with *.

Both Fe-N-$C_{CO2-tea}$ (figure 33 a) and Fe-N-$C_{urea-tea}$ (figure 33 b) have been analyzed with XRD technique and plots are both showing a peak from 19° up to

30° θ with a also a peak centred at 44.2°, indicating the presence of disorganized carbon. Accordingly to literature[135,136] deconvolution and fitting of the broad peak was made to distinguish two different contributions and avoid overestimation of crystallites. The peak is composed by two components, one is a band centered at 24.8° which is due to the sp^2 domains while the other is centered at 26.5° and is related to 002 reflection of graphite. The main component is the first one confirming the presence of graphitic domains. Fe-N-$C_{CO2\text{-}tea}$ shows a percentage of 44 % of graphitic component while Fe-N-$C_{urea\text{-}tea}$ shows a value up to 66%. Both samples present an intense 100 reflection due to a three dimensional crystal structure of the samples [137] and which is far more intense for Fe-N-$C_{CO2\text{-}tea}$ (figure 33 a) and far lower for Fe-N-$C_{urea\text{-}tea}$ (figure 33 b) indicating that Fe-N-$C_{urea\text{-}tea}$ present a more graphitic-like structure.

Furthermore, both the samples has small peaks centered at 15.5° and 16.7° that are attributed to the presence of Fe_3O_4 formed during ball milling of Fe-Pc, similarly to what has been reported by Goya et al.[138] It is interesting to note that Fe-N-$C_{CO2\text{-}tea}$ showed only the band 15.5°, probably because the other was too low in intensity to be appreciable considering the noise of the spectra. It's worth mentioning that the spectra was subjected to smoothing to reduce the noise therefore it's likely that information on very low peaks such as Fe_3O_4 are lost in the process. It also need to be considered that the iron phtalocyanine was added only after the pyrolysis and only ball milling process was performed, for this reason it's highly unlikely the formation of iron carbide (which needs temperatures over 800°C), while it's possible to see formation of Fe (III) considering the atmosphere in the ball milling not completely inert.

Anyhow, the proper assignation of the phase is not possible due to the super imposition of iron species signals with those of carbon. Nevertheless, it is reasonably supposing that the iron particles are formed by a combination of ferrites and iron (Fe (II) and (Fe(III) oxides, as also evident from XPS analysis (**Table 3**). The complexity of the species and the simultaneous presence of carbon matrix prevents a unique assignation.

5.3 TEM Analysis

To better discern the assignation, HR-TEM and STEM-EDX analyses were performed on these two electrocatalysts. **Figure 34** shows HR-TEM images acquired in bright-field mode of the Fe-based nanoparticles in the graphitic matrix

for the sample Fe-N-$C_{urea\text{-}tea}$. It's shown that the particles exhibit high degrees of crystallinity as evidenced by the well-defined atomic plane structure. As shown in **Figures 34 b-f**, it is possible to estimate a lattice plane distance of 0.34 nm, in agreement with the lattice parameter along the (211) direction of the Fe_3O_4 lattice. Other values possible for this lattice plane distance are Fe_3C, but it's extremely unlikely considering the type of synthesis, or graphitic nanodomains, excluded by next TEM analysis. This appears to be consistent with XRD and XPS data, which showed the presence of sharp peaks at 15.5° associated with a Fe_3O_4 phase.

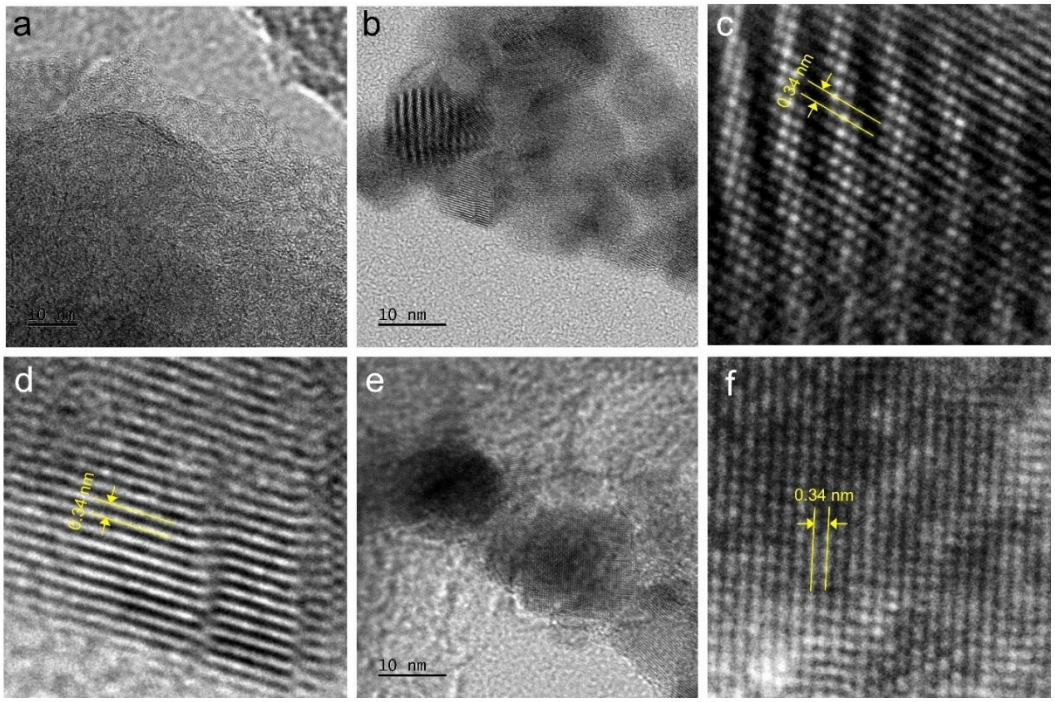

Figure 34 HR-TEM images acquired on sample Fe-N-$C_{urea\text{-}tea}$. (a): graphitic matrix; (b) and (e): Fe-based nanoparticles immersed in the graphitic matrix. (c) and (d): high magnification portion of the particles shown in panel (b). (f): high magnification portion of the particle shown in panel (e).

Figure 35 show HR-TEM images acquired in bright-field mode of the Fe-based nanoparticles in the graphitic matrix for the sample Fe-N-$C_{CO2\text{-}tea}$. In this case, the particles seem to be much further incorporated into the graphitic matrix. Nevertheless, a certain degree of crystallinity is still visible (**Fig. 35 c-d**) with a

periodic atomic separation of 0.61 nm. The HR-TEM results are once again consistent with XRD and XPS data, which now observe a weaker contribution from the Fe_3O_4 phase. It's worth mentioning the huge interlayer value could also be coming from impurities from metal ions in tea leaves, for example potassium[139].

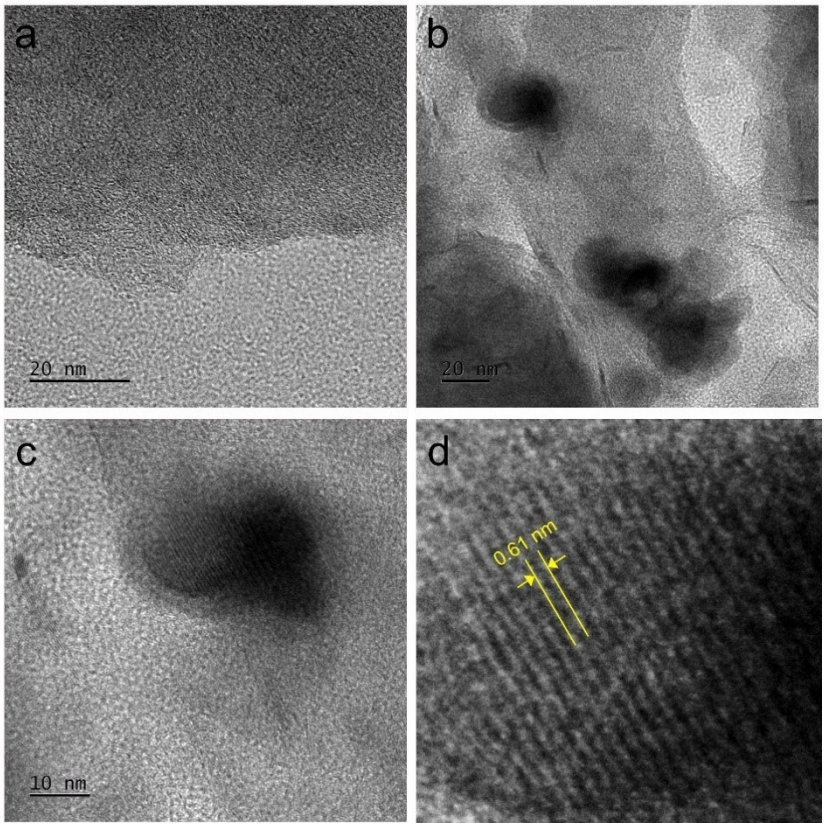

Figure 35 HR-TEM images acquired on sample Fe-N-$C_{CO2\text{-}tea}$. (a) graphitic matrix; (b and c) Fe-based nanoparticles immersed in the graphitic matrix;(d): high magnification portion of the particle shown in panel (c).

Figures 36 and **37** show STEM analysis of the investigated samples, together with EDX spectroscopy results for chemical mapping. In both cases of Fe-N-$C_{urea\text{-}tea}$ sample (**Fig. 36)** and Fe-N-$C_{CO2\text{-}tea}$ (**Fig. 37**) sample the nanoparticles appear darker in the BF-STEM images (**Figs. 36a** and **37a**), whereas they appear brighter in the DF-STEM images (**Figs. 36b and 37b**). This is consistent with a higher atomic number with respect to the surrounding carbon matrix. As visible from the EDX chemical analysis (**Figs. 36d-f and 37d-f)**, accumulation of iron is observed at the nanoparticle sites, while carbon and oxygen are more homogeneously dispersed.

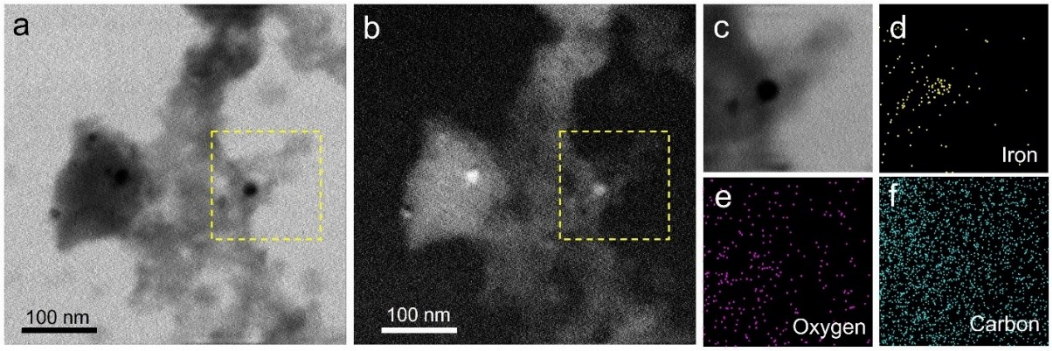

Figure 36 STEM-EDX analysis performed on the sample Fe-N-$C_{urea-tea}$. (a) BF-STEM image. (b) DF-STEM image. (c) BF-STEM image of the portion in panels a and b defined by the yellow square. (d)-(f) elemental area maps for iron (d), oxygen (e), and carbon (f).

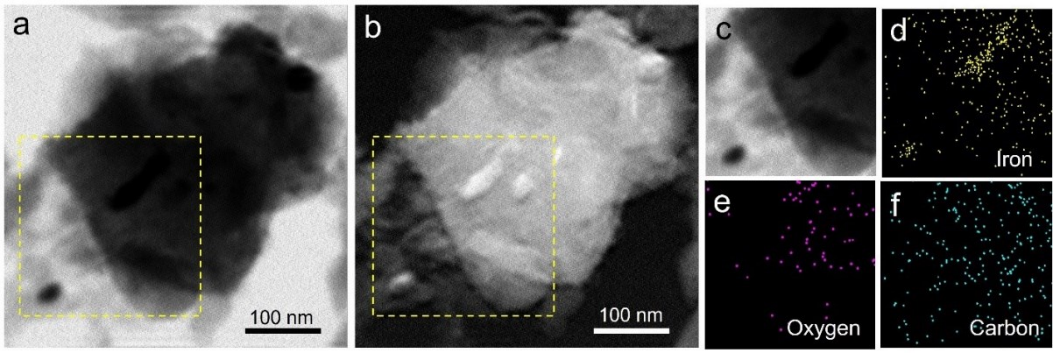

Figure 37 STEM-EDX analysis performed on the sample Fe-N-$C_{CO2-tea}$. (a) BF-STEM image. (b) DF-STEM image. (c) BF-STEM image of the portion in panels a and b defined by the yellow square. (d)-(f) elemental area maps for iron (d), oxygen (e), and carbon (f).

In summary, by combining the set of the various morphological characterization (XPS, XRD, TEM and ICP-OES), we can definitely rule out iron carbides and nitrides, and consider the main state of iron to be oxides. To further prove our hypothesis, we point out the distribution of oxygen in fig. 37 F: instead of being equally distributed within the carbon phase as would be expected in case of absence of iron oxides, it's more abundant in the region with the most iron sites, therefore it's reasonable to think part of the iron is in the form of oxide.The slightly higher mass activity of Fe-N-$C_{CO2-tea}$ sample is consistent with the higher

amount of Fe determined by ICP-OES (**Table 3**). Moreover, the higher incorporation level of Fe nanoparticles in the Fe-N-$C_{CO2\text{-}tea}$ sample appreciable by TEM (**Fig. 34 E/F**) can explain the better durability and stability of this catalyst when subjected to the two potential cycling protocols and chronoamperometry, as the iron sites are protected by the carbon scaffold, as also shown in the literature [140,141].

5.4 RRDE tests

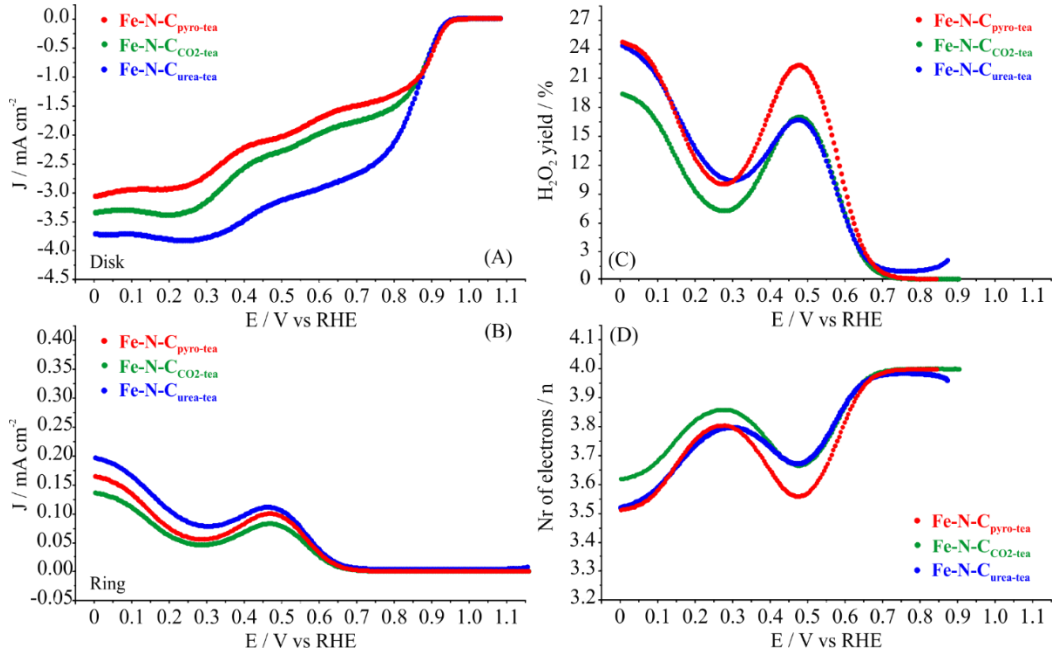

Figure 38: RRDE measurements at 900 rpm of Fe-N-$C_{pyro\text{-}tea}$, Fe-N-$C_{CO2\text{-}tea}$, and Fe-N-$C_{urea\text{-}tea}$, recorded at room temperature, in O_2-saturated 0.1 M KOH solution (scan rate 1 mV s^{-1}, electrode loading 400 µg cm^{-2}). (A) Disk current density. (B) Ring current density. (C) Calculated hydrogen peroxide, ring potential fixed at 1.2 V vs RHE. (D) Calculated number of electrons transferred.

We already showed the results of first screening ORR tests in RDE, which identified Fe-N-$C_{CO2\text{-}tea}$ as the most promising catalyst material while Fe-N-$C_{urea\text{-}tea}$ appears to be close in terms of performance although more difficult to replicate and Fe-N-$C_{pyro\text{-}tea}$ is set as a base standard to testify the effective improvements of the treatment and rule out eventual bad results like it was the case for Fe-N-$C_{nitrotea}$.

To further understand ORR pathway and selectivity of the reaction towards the production of H_2O_2 (partial 2 e^- reduction), RRDE measurements at 900 rpm were performed on the three Fe-N-C catalysts. Figure 35 reports the SCV data already presented and add more tests aimed at measurements of peroxide produced and electron trasferred. Again, the best performance belongs to Fe-N-$C_{CO2\text{-}tea}$, producing less amount of H_2O_2 (not higher than 18%) compared to Fe-N-$C_{urea\text{-}tea}$ and Fe-N-$C_{pyro\text{-}tea}$ (**Fig 38C**). Clearly, the functionalization of the starting $C_{pyro\text{-}tea}$ with urea or CO_2 helps improving the selectivity of the catalyst, even if the treatment with CO_2 seems to provide a slightly more selective catalyst (average values of electron transferred for Fe-N-$C_{CO2\text{-}tea}$: 3.82), transferring a higher number of electrons compared to Fe-N-$C_{urea\text{-}tea}$ (average values of electron transferred: 3.77) and Fe-N-$C_{pyro\text{-}tea}$ (average values of electron transferred: 3.74, **Fig 38D**).

All of these considerations make the catalyst Fe-N-$C_{CO2\text{-}tea}$ to be a good candidate for further investigation on methanol tolerance and durability tests. For a better understanding, also Fe-N-$C_{urea\text{-}tea}$ catalysts is considered for further analyses.

5.5 Methanol Tolerance tests

The ORR performance of Fe-N-$C_{urea\text{-}tea}$ and Fe-N-$C_{CO2\text{-}tea}$, namely the two best catalysts, was tested for methanol tolerance in order to evaluate the possible application of these catalysts in DMFC. As reported also in the literature, usually the methanol tolerance of this class of Fe-N-C catalysts is very good [109,142]. Thus, they have the chance to become good candidates to replace Pt as cathodic catalyst for DMFC. **Figure** 39 shows the polarization curves (LSV) of Fe-N-$C_{urea\text{-}tea}$ and Fe-N-$C_{CO2\text{-}tea}$ before and after the addition of increasing concentrations of MeOH up to 2 M to the solution. ORR activity is practically unaffected by the presence of MeOH, with a limited shift of less than 10 mV of the onset potential for both the catalysts. As a consequence, the biomass derived catalysts do not show a relevant change in the shape and the loss of activity is negligible, especially if compared to the activity of Pt/C. In fact, as a comparison, the commercial Pt/C catalyst was also tested with the same procedure, showing a collateral peak that starts to appear at concentrations of 0.1 M, and a shift of the onset potential of more than 200 mV at concentration of 1 M, correlated with the preference of the noble catalyst for the methanol oxidation reaction. In the case of our potentiostat, the curve just goes up and interrupts the recording, but in literature there is observation of a well-defined peak going up and down and finish the curve

similarly the one without methanol. Thus, the biomass derived catalysts can be considered a valid alternative to mitigate the methanol crossover effect in DMFC.

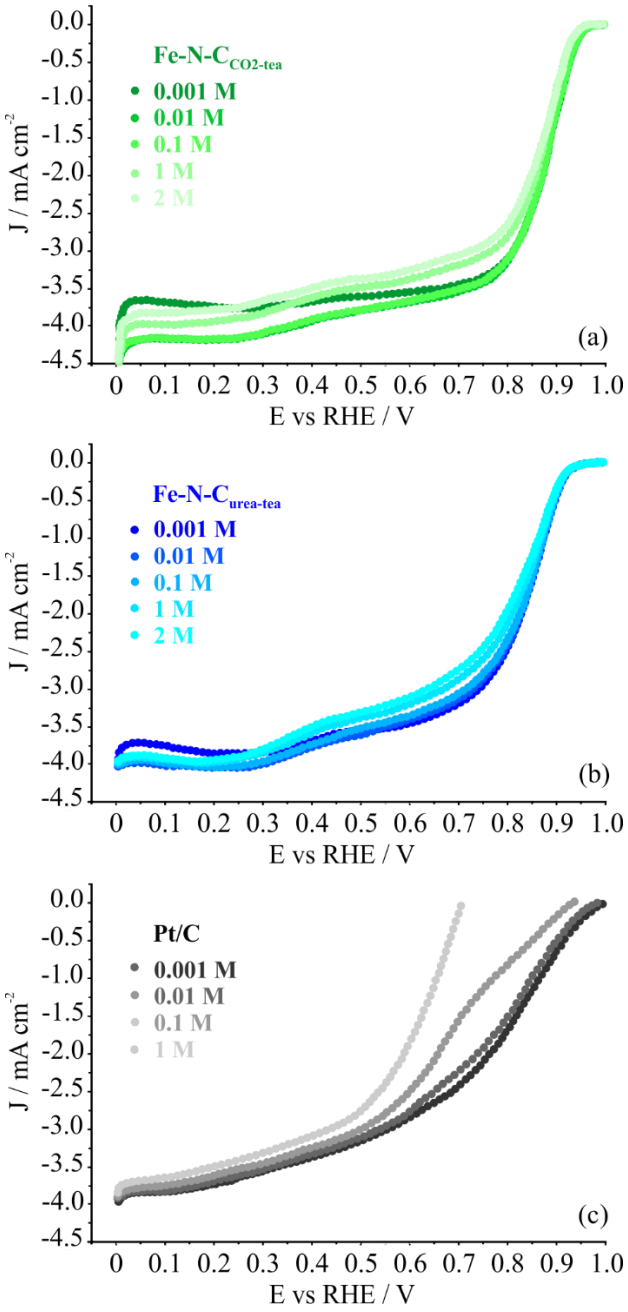

Figure 39: Methanol tolerance test: LSV plots at different methanol concentrations for Fe-N-C$_{CO2-tea}$ (A), Fe-N-C$_{urea-tea}$ (B), and Pt/C (C), in 0.1 KOH solution, saturated with O_2. Rotation speed 900 rpm, scan rate 5 mV s^{-1}, electrode loading 400 µg cm^{-2} (30 µg cm^{-2} for Pt/C).

5.6 Durability tests

The best catalyst was tested for durability performance in RDE. Two different protocols were used, both derived from a test proposed during the Fuel Cell Commercialization Conference of Japan (FCCCJ) in 2011 [114] , as depicted in **Figure 40.** The second protocol, with a faster scan rate and a 3 s hold at the border potentials, is supposed to stress the material more, simulating the effective type of workload of a fuel cell and trying to evaluate the stress of months of usage with a test lasting a few hours. For sake of comparison, also the commercial Pt/C catalyst was subjected to the same durability protocols.

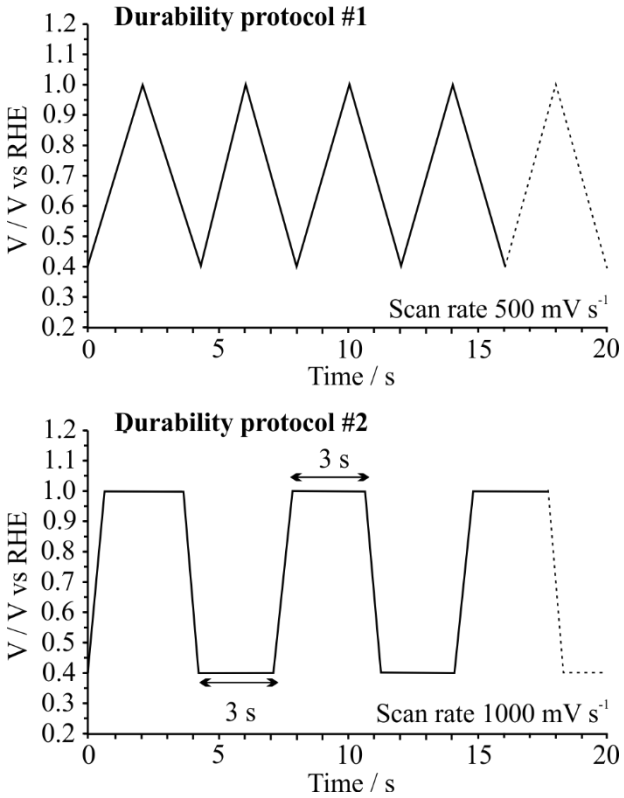

Figure 40: Schematic representation of the applied potential over time in the two durability protocols, performed in O_2-saturated 0.1 KOH electrolyte

Figure 41 and **Table 4** show the results of the potential cycling according to the two testing protocols. In terms of onset and half wave potential, there is practically no visible difference comparing the ORR activity at the beginning and end of the two durability protocols for Fe-N-$C_{urea\text{-}tea}$ and Fe-N-$C_{CO2\text{-}tea}$, while Pt/C lose almost 50 mV for both values. In terms of mass activity at 0.9 V vs RHE, Fe-N-$C_{urea\text{-}tea}$ displays no loss at all for both the protocols, while Fe-N-$C_{CO2\text{-}tea}$ lose only 10% of mass activity after 4,500 cycles in the second protocol, while retaining its original activity without potential hold. These values indicate a good resistance to wide potential cycling for our biomass derived catalysts under a challenging O_2-containing environment, making the durability of this catalyst interesting to be tested also in fuel cell in future works. Notably, for Pt/C the activity loss can reach over 80% in the most stressing condition, demonstrating the well-known low durability of these catalysts because of the carbon corrosion and Pt aggregation phenomena. It is out hypothesis that continuing the cycling, for example by doubling the number of cycles, would lead Pt-C catalyst to lose even more while our biomass-derived would likely keep the loss under 20% in both protocols. For these reasons, these biochar-derived Fe-N-C catalysts can be considered a valid alternative to Pt/C based catalysts, in particular for DMFC applications, thanks to their good stability, as also shown in the literature [140,143]. We consider this work a starting point for a series of syntheses which could lead to useful catalysts. In fact, thanks to the zero cost of the starting carbon material, the pyrolysis of biomass could lead to low-cost catalysts' synthesis, with benefits in terms of recycling of materials and circular economy [144].

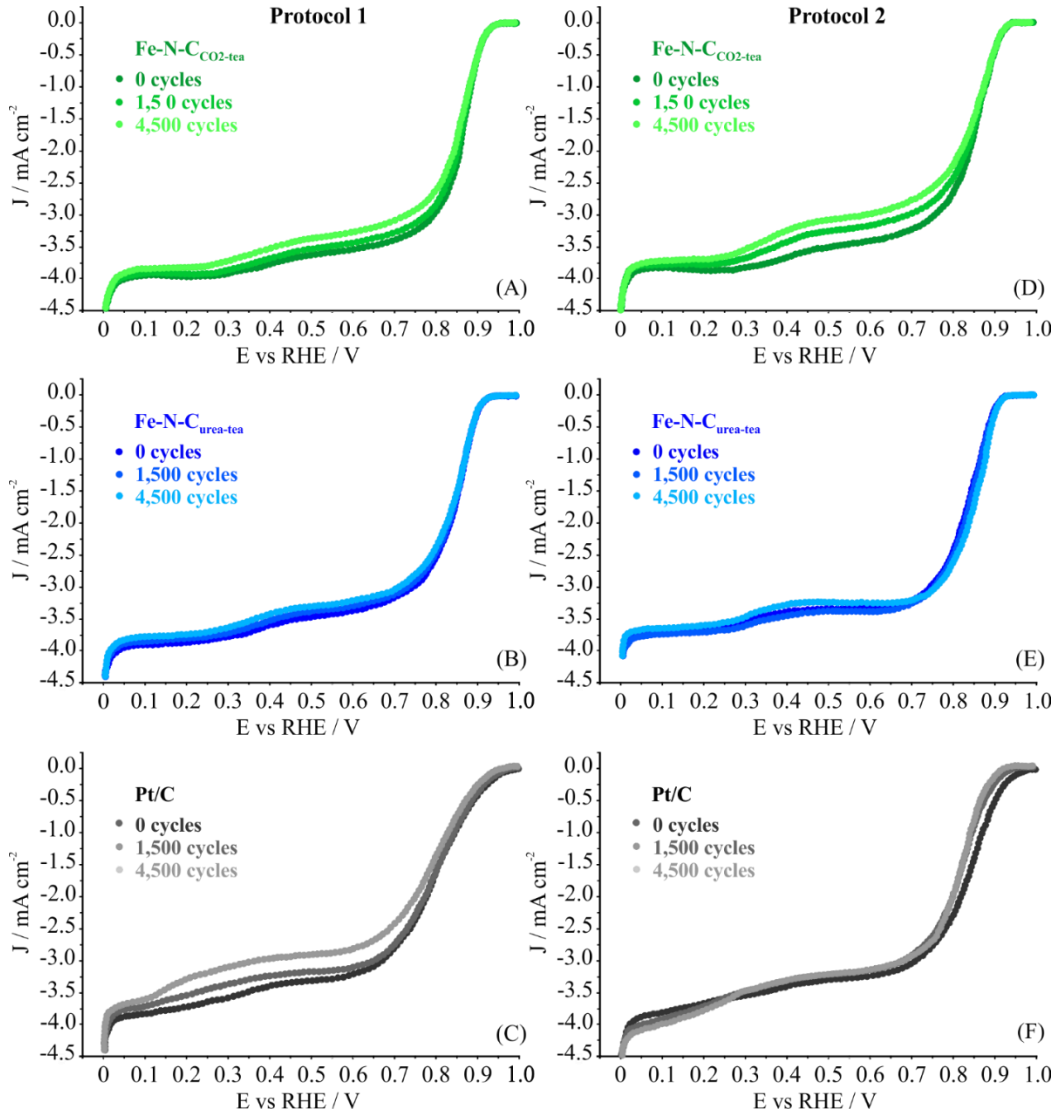

Figure 41: Durability protocols 1 (A/B/C) and 2 (E/F/G): LSV plots at different cycles for Fe-N-C$_{CO2-tea}$ (A/D), Fe-N-C$_{urea-tea}$ (B/E), and Pt/C (C/F), in 0.1 KOH solution, saturated with O_2. Rotation speed 900 rpm, scan rate 5 mV s^{-1}, electrode loading 400 µg cm^{-2} (30 µg cm^{-2} for Pt/C).

Chronoamperometric measurements were also employed to verify the stability of the catalysts. **Figure 42** shows the results in terms of relative current density decay during 5,000 s at a constant potential of 0.60 V vs RHE in O_2-saturated 0.1 M KOH solution at room temperature. Considering the chronoamperometric tests Fe-N-C$_{CO2-tea}$ resulted the most stable catalyst, far more than the commercial Pt/C, by retaining almost 94% of the current density. The high loss for Fe-N-C$_{urea-tea}$ is unexpected considering the good performance in the former stress protocol. We

can't rule out aging of the sample or problem in the measurement. This result could also be explained considering the higher specific capacitance of this catalyst compared to that of Fe-N-$C_{urea-tea}$.

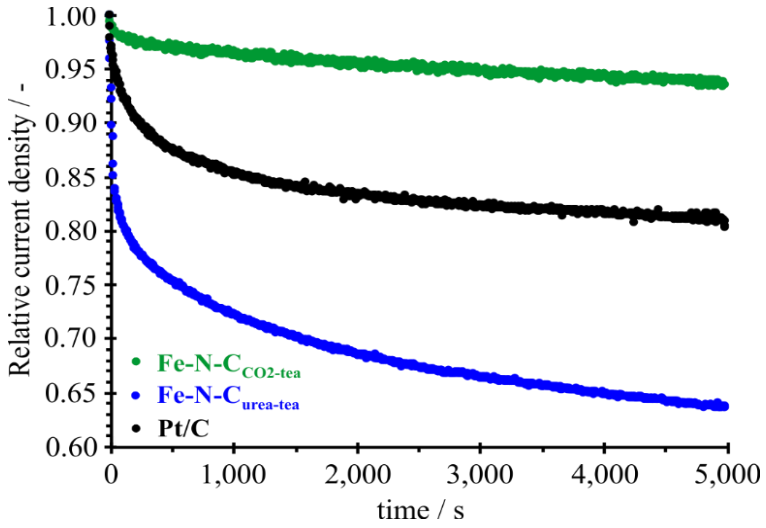

Figure 42: Chronoamperometric curves performed at 0.6 V vs RHE for 5,000 s, on Fe-N-$C_{CO2-tea}$, Fe-N-$C_{urea-tea}$, and Pt/C, in 0.1 KOH solution, saturated with O_2, rotation speed 900 rpm (electrode loading 400 μg cm^{-2}, 30 μg_{Pt} cm^{-2} for Pt/C).

Table 4: Mass activity loss calculated at 0.9 V vs RHE at the end of the two durability protocols and current density loss evaluated at the end of chronoamperometry at 0.6 V vs RHE.

	20 wt% Pt/C	Fe-N-$C_{CO2-tea}$	Fe-N-$C_{urea-tea}$
M.A. loss @ 0.9 V [A g^{-1}] Protocol #1	40%	0	0
M.A. loss @ 0.9 V [A g^{-1}] Protocol #2	80%	10%	0
C.D. loss @ 0.6 V [mA cm^{-2}] Chronoamperometry	19%	6%	36%

Conclusions and future perspectives

Our work started with considerations about circular economy, aiming at synthesis of useful chemical materials starting from biowastes. We considered the spread and abundance of biomass wastes and the need of disposal for these, which means not only the cost of providing them is close to zero but also that their recycling is desired and there is value in starting from discarded residues. With this in mind, we chose the type of biomass to focus on, developed a strategy, and therefore a series of catalyst is synthetized and characterized with different techniques and methods. The development of the project was similar to the grow of the branches of a tree: different approaches were adopted and materials which were demonstrated as not effective were ruled out after preliminary study. We started with tea and coffee as interesting biomass to be converted to carbon source for an ORR electrocatalyst. But very quickly we had to exclude one of the two species because of the low performance. Nonetheless, all the data are presented as a mean of comparison and to prove that even if there is a large number of published papers and biomass analyzed, not all waste material has the potential to be further studied and a precise screening is needed. For tea-derived materials the results were far better, and it was possible to proceed to a direct comparison with a commercial catalyst based on platinum. As a general consideration we can confirm that the materials are all active towards ORR (even the discarded nitro tea pathway was in fact active towards the reaction, just not enough to justify the prosecution of tests), as well as being methanol tolerant and highly stable. It was important to further develop the original starting material in order to evaluate the effect of different treatments and also note that not all of them was interesting to go into detail. The performance of the materials testifies the quality of both Fe-N-C catalysts in alkaline environment and the ball milling procedure as an efficient pathway to replace or go side by side with pyrolysis and other heat treatments. We want to point out that the best catalysts were those where pyrolysis was only used for the starting biomass, not after iron introduction, as the heat treatment performed after the ball milling was shown to be deleterious to the activity of the material, even after acid washing.

In terms of economic advantages, it’s worth mentioning the only expensive starting material was Fe(II) phthalocyanine while biochar has negligible cost of purchase and acceptable cost of treatment. It’s also to consider that our choice to

pyrolyze at 1500 °C, a temperature not usually employed in literature, and following by an activation with CO_2 or urea was all in the purpose of obtaining high value material, and in general to develop a procedure that could in the future be tested with different starting biomass. In terms of onset and half wave potential, the values in alkaline environment are really close to commercially available catalysts. The Fe-N-C catalysts showed promising ORR activity in RDE, albeit not equal to platinum but considering the premise of waste recycling, the performance was acceptable. As already noted, the materials present high methanol tolerance and very good stability under potential cycling protocols, losing no more than 10% of the starting activity with the most stressing protocol, while a commercial 20% Pt/C catalyst lost 80% of its starting activity under potential cycling. The introduction of iron in the carbon structure forms active sites explaining the activity, and with the physical characterization available we can formulate a quite accurate hypothesis on what type of sites are available in our samples and what are advantages and disadvantages of both tested protocols. The presence of both iron nanoparticles and N_4 moieties is a good explanation of both the ORR mechanism and performance.

In particular, CO_2-activated biochar-derived Fe-N-C demonstrated to be very stable thanks to a higher degree of Fe oxides encapsulation into the graphitic carbon matrix as speculated after XPS, XRD and TEM analysis. It is our hypothesis that the environment protects the iron site allowing long cycling potential. In fact, this was the only catalyst performing well in both chronoamperometric tests and repeated cycling. Thus, the Fe-N-$C_{CO2\text{-}tea}$ catalyst can be considered a valid alternative to Pt/C based catalysts, in particular for DMFC applications. C-$_{ureatea}$ has its advantages but at the moment considering the difficult replicability of the measures, it's slightly behind in the hierarchy, almost at the level of the starting $C_{pyrotea}$. The results presented in this work demonstrate that the use of biochar-derived materials in the synthesis of PGM-free Fe-N-C based catalysts for ORR opens up possibilities in the design of alternative catalysts.

By concluding, the CO_2-activated biochar-derived Fe-N-C catalyst can be considered a valid alternative to Pt/C based catalysts, in particular for DMFC applications, thanks to the good stability and very good methanol tolerance, as also shown in the literature [140,143]. Activation of the biochar with CO_2 is necessary to enhance the selectivity of the final catalyst towards the ORR via the 4-electrons pathway. This work can be a starting point for a series of syntheses which could lead to useful catalysts. In fact, the proposed syntheses are quite straightforward

and also easy to scale up or to be applied to other waste biomass materials, thanks to the zero cost of the starting carbon material, the pyrolysis of biomass could lead to low-cost catalysts' synthesis, with benefits in terms of recycling of materials and circular economy [144]. The micro-porosity of the materials synthesized and the nitrogen content, to favor the formation of Fe-N_x active sites should be improved with further activation treatments and N-based doping of the biochar, to expect an enhanced ORR activity [145].

It's also interesting to keep analyzing this type of materials, namely the tea derived Fe-N-C catalyst, due to the number of analyses still possible to perform. Due to both time constrictions and lack of instrumentation, lots of physical analyses were not possible to be performed, especially in-situ techniques which could help to evaluate the physical properties of the sample while it is performing and not in stasis condition. And of course, the most important test still to be conducted is fuel cell implementation. The best catalyst should be deposited as a cathode and tested in a functional fuel cell station to evaluate the performance and the durability in a real working environment, which usually proves to be different from RDE environment because of different mechanism involved.

To sum up, this work, albeit with difficulties due to time and the world pandemic, is supposed to build the foundation of a more systematic study of different types of biomass with different and optimized synthetic routes, which will lead to the selection of the best catalyst overall and its implementation for PEM fuel cells and DMFC testing and following applications. Although it's possible that platinum performance may not be reached and maybe expect applications in field like transportation is too bold because of the high requirements, it would still be a nice goal to employ waste recycling to obtain low cost catalyst which may find applications in smaller scale devices.

Table 5: Comparison of different performances from biomass derived material published in literature. All data are measured in 0.1 M KOH solution

Biomass source	Doped atoms	Surface area (m^2g^{-1})	Eonset (V, vs RHE)	$E_{1/2}$ (V, vs RHE)	Transf. Electrons	Ref.
Cellulose nanofibrils	N: 3.3 S: 0.6 P: 2.5	682	0.94	0.76	3.6-3.9	[79]
Starch	N: 6.08 Fe: 0.35	1088	0.95	0.84	3.78	[80]
Coconut shells	N: 1.1 P: 2.3	1071	0.94	0.75	3.7	[81]
Bamboo Fungus	N: 2.43	1896	1.05	0.89	3.6	[84]
Tea Residue	N:2.8 F: 2.2	855	0.81	0.66	3.8	[85]
Seaweed	N<0.1	1377	1.01	0.83	3.87-3.98	[86]
Eggplant	N: 1.04	1969	0.88	0.78	3.87	[87]
Spent Coffee	N: 3.11	1018	0.94	0.78	3.98	[88]
Sheep Horn	N: 3.14 S: 0.22	320	0.904	0.73	3.68	[89]
Bamboo	N: 6.32 S: 1.26	349.1	0.9	0.85	3.56	[91]
Lettuce	N:7.76	823	1.0	0.88	3.95	[93]
TEA RESIDUE	**N: 5 - 16 Fe: 2.59-3.59**	**4.5-51.1**	**0.93-0.95**	**0.89**	**3.74-3.82**	**THIS WORK** [146]

References

1. Wang, Y., Chen, K. S., Mishler, J., Cho, S. C. & Adroher, X. C. A review of polymer electrolyte membrane fuel cells: Technology, applications, and needs on fundamental research. *Appl. Energy* **88**, 981–1007 (2011).

2. Pollet, B. G., Kocha, S. S. & Staffell, I. Current status of automotive fuel cells for sustainable transport. *Curr. Opin. Electrochem.* **16**, 90–95 (2019).

3. Debe, M. K. Electrocatalyst approaches and challenges for automotive fuel cells. *Nature* **486**, 43–51 (2012).

4. Sealy, C. The problem with platinum. *Mater. Today* **11**, 65–68 (2008).

5. Wang, Y., Chen, K. S., Mishler, J., Cho, S. C. & Adroher, X. C. A review of polymer electrolyte membrane fuel cells: Technology, applications, and needs on fundamental research. *Appl. Energy* **88**, 981–1007 (2011).

6. Gottesfeld, S. *et al.* Anion exchange membrane fuel cells: Current status and remaining challenges. *J. Power Sources* **375**, 170–184 (2018).

7. Ferrero, G. A., Preuss, K., Fuertes, A. B., Sevilla, M. & Titirici, M. M. The influence of pore size distribution on the oxygen reduction reaction performance in nitrogen doped carbon microspheres. *J. Mater. Chem. A* **4**, 2581–2589 (2016).

8. Ong, B. C., Kamarudin, S. K. & Basri, S. Direct liquid fuel cells: A review. *Int. J. Hydrogen Energy* **42**, 10142–10157 (2017).

9. Kamarudin, S. K., Achmad, F. & Daud, W. R. W. Overview on the application of direct methanol fuel cell (DMFC) for portable electronic devices. *Int. J. Hydrogen Energy* **34**, 6902–6916 (2009).

10. Shaari, N., Kamarudin, S. K., Bahru, R., Osman, S. H. & Md Ishak, N. A. I. Progress and challenges: Review for direct liquid fuel cell. *Int. J. Energy Res.* **45**, 6644–6688 (2021).

11. Kimiaie, N. *et al.* Results of a 20 000 h lifetime test of a 7 kW direct methanol fuel cell (DMFC) hybrid system-degradation of the DMFC stack and the energy storage. *Energy Environ. Sci.* **7**, 3013–3025 (2014).

12. Wroblowa, H. S. & Qaderi, S. B. Mechanism and kinetics of oxygen

reduction on steel. *J. Electroanal. Chem.Electroanal Chem* **279**, 231–242 (1990).

13. Anastasijević, N. A., Vesović, V. & Adžić, R. R. Determination of the kinetic parameters of the oxygen reduction reaction using the rotating ring-disk electrode. *J. Electroanal. Chem. Interfacial Electrochem.* **229**, 305–316 (1987).

14. Vesovic, V., Anastasijevic, N. & Adzic, R. R. Rotating disk electrode: A re-examination of some kinetic criteria with a special reference to oxygen reduction. *J. Electroanal. Chem. Interfacial Electrochem.* **218**, 53–63 (1987).

15. Ma, R. *et al.* A review of oxygen reduction mechanisms for metal-free carbon-based electrocatalysts. *npj Computational Materials* vol. 5 (2019).

16. Ramaswamy, N. & Mukerjee, S. Fundamental mechanistic understanding of electrocatalysis of oxygen reduction on Pt and non-Pt surfaces: Acid versus alkaline media. *Adv. Phys. Chem.* **2012**, (2012).

17. Strelko, V. V. *et al.* Mechanism of reductive oxygen adsorption on active carbons with various surface chemistry. *Surf. Sci.* **548**, 281–290 (2004).

18. Jasinski, R. NATURE March 21, 1964. *Nature* **201**, 1963–1964 (1964).

19. Gong, K., Du, F., Xia, Z., Durstock, M. & Dai, L. Nitrogen-Doped Carbon Nanotube. *Science (80-.).* **323**, 760–764 (2009).

20. Ge, X. *et al.* Oxygen Reduction in Alkaline Media: From Mechanisms to Recent Advances of Catalysts. *ACS Catal.* **5**, 4643–4667 (2015).

21. Wang, W., Jia, Q., Mukerjee, S. & Chen, S. Recent Insights into the Oxygen-Reduction Electrocatalysis of Fe/N/C Materials. *ACS Catal.* **9**, 10126–10141 (2019).

22. Jaouen, F. O2 reduction mechanism on non-noble metal catalysts for PEM fuel cells. Part II: A porous-electrode model to predict the quantity of H 2O2 detected by rotating ring-diskelectrode. *J. Phys. Chem. C* **113**, 15433–15443 (2009).

23. Choi, C. H. *et al.* Unraveling the Nature of Sites Active toward Hydrogen Peroxide Reduction in Fe-N-C Catalysts. *Angew. Chemie - Int. Ed.* **56**, 8809–8812 (2017).

24. Liu, G., Li, X., Lee, J. W. & Popov, B. N. A review of the development of

nitrogen-modified carbon-based catalysts for oxygen reduction at USC. *Catal. Sci. Technol.* **1**, 207–217 (2011).

25. Srivastava, D., Susi, T., Borghei, M. & Kari, L. Dissociation of oxygen on pristine and nitrogen-doped carbon nanotubes: A spin-polarized density functional study. *RSC Adv.* **4**, 15225–15235 (2014).

26. Wu, G. *et al.* Carbon nanocomposite catalysts for oxygen reduction and evolution reactions: From nitrogen doping to transition-metal addition. *Nano Energy* **29**, 83–110 (2016).

27. Oh, H. S., Oh, J. G., Lee, W. H., Kim, H. J. & Kim, H. The influence of the structural properties of carbon on the oxygen reduction reaction of nitrogen modified carbon based catalysts. *Int. J. Hydrogen Energy* **36**, 8181–8186 (2011).

28. Wang, Z. *et al.* Nitrogen-promoted self-assembly of N-doped carbon nanotubes and their intrinsic catalysis for oxygen reduction in fuel cells. *ACS Nano* **5**, 1677–1684 (2011).

29. Hoon, C. *et al.* Heat-Treated Non-precious Metal Catalysts for Oxygen Reduction. in *Electrochemistry of N4 Macrocyclic Metal Complexes* (eds. Zagal, J. H. & Bedioui, F.) 41–68 (Springer International Publishing Switzerland, 2016). doi:10.1007/978-3-319-31172-2.

30. Jin, C. *et al.* Metal-free and electrocatalytically active nitrogen-doped carbon nanotubes synthesized by coating with polyaniline. *Nanoscale* **2**, 981–987 (2010).

31. Liu, J., Song, P., Ning, Z. & Xu, W. Recent Advances in Heteroatom-Doped Metal-Free Electrocatalysts for Highly Efficient Oxygen Reduction Reaction. *Electrocatalysis* **6**, 132–147 (2015).

32. Wu, Y. J. *et al.* Three-Dimensional Networks of S-Doped Fe/N/C with Hierarchical Porosity for Efficient Oxygen Reduction in Polymer Electrolyte Membrane Fuel Cells. *ACS Appl. Mater. Interfaces* **10**, 14602–14613 (2018).

33. Matanovic, I., Artyushkova, K. & Atanassov, P. Understanding PGM-free catalysts by linking density functional theory calculations and structural analysis: Perspectives and challenges. *Curr. Opin. Electrochem.* **9**, 137–144 (2018).

34. Osmieri, L., Pezzolato, L. & Specchia, S. Recent trends on the application of PGM-free catalysts at the cathode of anion exchange membrane fuel cells. *Curr. Opin. Electrochem.* **9**, 240–256 (2018).

35. Escobar, B. *et al.* Research progress on biomass-derived carbon electrode materials for electrochemical energy storage and conversion technologies. *Int. J. Hydrogen Energy* **46**, 26053–26073 (2021).

36. Tabac, S. & Eisenberg, D. Pyrolyze this paper: Can biomass become a source for precise carbon electrodes? *Curr. Opin. Electrochem.* **25**, 100638 (2021).

37. Li, Y. *et al.* Sustainable and Atomically Dispersed Iron Electrocatalysts Derived from Nitrogen- and Phosphorus-Modified Woody Biomass for Efficient Oxygen Reduction. *Adv. Mater. Interfaces* **6**, 1801623 (2019).

38. Artyushkova, K., Serov, A., Rojas-Carbonell, S. & Atanassov, P. Chemistry of Multitudinous Active Sites for Oxygen Reduction Reaction in Transition Metal-Nitrogen-Carbon Electrocatalysts. *J. Phys. Chem. C* **119**, 25917–25928 (2015).

39. Osmieri, L. *et al.* Elucidation of Fe-N-C electrocatalyst active site functionality via in-situ X-ray absorption and operando determination of oxygen reduction reaction kinetics in a PEFC. *Appl. Catal. B Environ.* **257**, 117929 (2019).

40. Xiao, M. *et al.* Microporous Framework Induced Synthesis of Single-Atom Dispersed Fe-N-C Acidic ORR Catalyst and Its in Situ Reduced Fe-N4 Active Site Identification Revealed by X-ray Absorption Spectroscopy. *ACS Catal.* **8**, 2824–2832 (2018).

41. Kumar, K. *et al.* Fe-N-C Electrocatalysts' Durability: Effects of Single Atoms' Mobility and Clustering. *ACS Catal.* **11**, 484–494 (2021).

42. Tylus, U. *et al.* Elucidating oxygen reduction active sites in pyrolyzed metal-nitrogen coordinated non-precious-metal electrocatalyst systems. *J. Phys. Chem. C* **118**, 8999–9008 (2014).

43. EU Commission. *COMMUNICATION FROM THE COMMISSION TO THE EUROPEAN PARLIAMENT, THE COUNCIL, THE EUROPEAN ECONOMIC AND SOCIAL COMMITTEE AND THE COMMITTEE OF THE REGIONS. A new Circular Economy Action Plan For a cleaner and more competitive Europe* https://eur-lex.europa.eu/legal-content/EN/TXT/PDF/?uri=CELEX:52020DC0098&from=EN (2020).

44. Sherwood, J. The significance of biomass in a circular economy. *Bioresour. Technol.* **300**, (2020).

45. Scharff, C. THE EU CIRCULAR ECONOMY PACKAGE AND THE CIRCULAR ECONOMY COALITION FOR EUROPE. 1–18.

46. Camacho-Otero, J., Boks, C. & Pettersen, I. N. Consumption in the circular economy: A literature review. *Sustain.* **10**, (2018).

47. Slootweg, J. C. Using waste as resource to realize a circular economy: Circular use of C, N and P. *Curr. Opin. Green Sustain. Chem.* **23**, 61–66 (2020).

48. Lacy, P. & Rutqvist, J. *Waste to Wealth the Circular Economy Advantage*. *1st edition* vol. 1 (2015).

49. Muhyuddin, M., Mustarelli, P. & Santoro, C. Recent Advances in Waste Plastic Transformation into Valuable Platinum-Group Metal-Free Electrocatalysts for Oxygen Reduction Reaction. *ChemSusChem* **14**, 3785–3800 (2021).

50. Muhyuddin, M. *et al.* Waste Face Surgical Mask Transformation into Crude Oil and Nanostructured Electrocatalysts for Fuel Cells and Electrolyzers. *ChemSusChem* 1–15 (2021) doi:10.1002/cssc.202102351.

51. Bar-On, Y. M., Phillips, R. & Milo, R. The biomass distribution on Earth. *Proc. Natl. Acad. Sci.* **115**, 6506–6511 (2018).

52. Lv, W. *et al.* Peanut shell derived hard carbon as ultralong cycling anodes for lithium and sodium batteries. *Electrochim. Acta* **176**, 533–541 (2015).

53. Du, L. *et al.* Electrocatalytic valorisation of biomass derived chemicals. *Catal. Sci. Technol.* **8**, 3216–3232 (2018).

54. Kalyani, P. & Anitha, A. Biomass carbon & its prospects in electrochemical energy systems. *Int. J. Hydrogen Energy* **38**, 4034–4045 (2013).

55. Du, L. *et al.* Biomass-derived nonprecious metal catalysts for oxygen reduction reaction: The demand-oriented engineering of active sites and structures. *Carbon Energy* **2**, 561–581 (2020).

56. Lin, G. *et al.* KOH activation of biomass-derived nitrogen-doped carbons for supercapacitor and electrocatalytic oxygen reduction. *Electrochim. Acta* **261**, 49–57 (2018).

57. Jiang, L., Sheng, L. & Fan, Z. Biomass-derived carbon materials with structural diversities and their applications in energy storage. *Sci. China Mater.* **61**, 133–158 (2018).

58. Tang, W. *et al.* Natural biomass-derived carbons for electrochemical energy storage. *Mater. Res. Bull.* **88**, 234–241 (2017).

59. Yan, L., Yu, J., Houston, J., Flores, N. & Luo, H. Biomass derived porous nitrogen doped carbon for electrochemical devices. *Green Energy Environ.* **2**, 84–99 (2017).

60. Tripathi, N., Hills, C. D., Singh, R. S. & Atkinson, C. J. Biomass waste utilisation in low-carbon products: harnessing a major potential resource. *npj Clim. Atmos. Sci.* **2**, (2019).

61. Yang, M. *et al.* Highly cost-effective nitrogen-doped porous coconut shell-based CO2 sorbent synthesized by combining ammoxidation with KOH activation. *Environ. Sci. Technol.* **49**, 7063–7070 (2015).

62. Borghei, M., Lehtonen, J., Liu, L. & Rojas, O. J. Advanced Biomass-Derived Electrocatalysts for the Oxygen Reduction Reaction. *Adv. Mater.* **30**, 1–27 (2018).

63. Klemm, D., B, Heinze, T., Heinze, U. & Wagenknecht, W. *Comprehensive Cellulose Chemistry; Volume I: Fundamentals and Analytical Methods*. vol. I (Wiley, 1998).

64. Habibi, Y., Lucia, L. A. & Rojas, O. J. Cellulose nanocrystals: Chemistry, self-assembly, and applications. *Chem. Rev.* **110**, 3479–3500 (2010).

65. Wu, Z. Y., Liang, H. W., Chen, L. F., Hu, B. C. & Yu, S. H. Bacterial Cellulose: A Robust Platform for Design of Three Dimensional Carbon-Based Functional Nanomaterials. *Acc. Chem. Res.* **49**, 96–105 (2016).

66. Ago, M. *et al.* Supramolecular assemblies of lignin into nano- and microparticles. *MRS Bull.* **42**, 371–378 (2017).

67. Dutta, P., Dutta, J. & Tripathi, V. Chitin and chitosan: Properties and applications. *J. Sci. Ind. Res.* **63**, 20–31 (2004).

68. Pillai, C. K. S., Paul, W. & Sharma, C. P. Chitin and chitosan polymers: Chemistry, solubility and fiber formation. *Prog. Polym. Sci.* **34**, 641–678 (2009).

69. Kaushik, A., Singh, M. & Verma, G. Green nanocomposites based on thermoplastic starch and steam exploded cellulose nanofibrils from wheat straw. *Carbohydr. Polym.* **82**, 337–345 (2010).

70. Alipour Moghadam Esfahani, R. *et al.* H2-rich syngas production through mixed residual biomass and HDPE waste via integrated catalytic gasification and tar cracking plus bio-char upgrading. *Chem. Eng. J.* **308**, 578–587 (2017).

71. Bazargan, A., Yan, Y., Hui, C. W. & McKay, G. A review: Synthesis of carbon-based nano and micro materials by high temperature and high pressure. *Ind. Eng. Chem. Res.* **52**, 12689–12702 (2013).

72. Titirici, M. M., White, R. J., Falco, C. & Sevilla, M. Black perspectives for a green future: Hydrothermal carbons for environment protection and energy storage. *Energy Environ. Sci.* **5**, 6796–6822 (2012).

73. Zhang, P. *et al.* Updating biomass into functional carbon material in ionothermal manner. *ACS Appl. Mater. Interfaces* **6**, 12515–12522 (2014).

74. Pereira, R. G. *et al.* Preparation of activated carbons from cocoa shells and siriguela seeds using H3PO4 and ZnCL2 as activating agents for BSA and α-lactalbumin adsorption. *Fuel Process. Technol.* **126**, 476–486 (2014).

75. Mi, J., Wang, X. R., Fan, R. J., Qu, W. H. & Li, W. C. Coconut-shell-based porous carbons with a tunable micro/mesopore ratio for high-performance supercapacitors. *Energy and Fuels* **26**, 5321–5329 (2012).

76. Shen, W. & Fan, W. Nitrogen-containing porous carbons: Synthesis and application. *J. Mater. Chem. A* **1**, 999–1013 (2013).

77. De, S., Balu, A. M., Van Der Waal, J. C. & Luque, R. Biomass-derived porous carbon materials: Synthesis and catalytic applications. *ChemCatChem* **7**, 1608–1629 (2015).

78. Deng, J., Li, M. & Wang, Y. Biomass-derived carbon: Synthesis and applications in energy storage and conversion. *Green Chem.* **18**, 4824–4854 (2016).

79. Mulyadi, A., Zhang, Z., Dutzer, M., Liu, W. & Deng, Y. Facile approach for synthesis of doped carbon electrocatalyst from cellulose nanofibrils toward high-performance metal-free oxygen reduction and hydrogen evolution. *Nano Energy* **32**, 336–346 (2017).

80. Yao, W. T. *et al.* Bulk Production of Nonprecious Metal Catalysts from Cheap Starch as Precursor and Their Excellent Electrochemical Activity. *ACS Sustain. Chem. Eng.* **4**, 3235–3244 (2016).

81. Borghei, M. *et al.* Porous N,P-doped carbon from coconut shells with high electrocatalytic activity for oxygen reduction: Alternative to Pt-C for alkaline fuel cells. *Appl. Catal. B Environ.* **204**, 394–402 (2017).

82. Borghei, M. *et al.* Porous N,P-doped carbon from coconut shells with high electrocatalytic activity for oxygen reduction: Alternative to Pt-C for alkaline

fuel cells. *Appl. Catal. B Environ.* **204**, 394–402 (2017).

83. Schonvogel, D. *et al.* Hydrothermal Carbonization-Derived Carbon from Waste Biomass as Renewable Pt Support for Fuel Cell Applications: Role of Carbon Activation. *Energy Technol.* **7**, (2019).

84. Gao, S., Fan, H. & Zhang, S. Nitrogen-enriched carbon from bamboo fungus with superior oxygen reduction reaction activity. *J. Mater. Chem. A* **2**, 18263–18270 (2014).

85. Wu, D. *et al.* Tea-leaf-residual derived electrocatalyst: Hierarchical pore structure and self nitrogen and fluorine co-doping for efficient oxygen reduction reaction. *Int. J. Hydrogen Energy* **43**, 19492–19499 (2018).

86. Hao, Y. *et al.* Highly porous defective carbons derived from seaweed biomass as efficient electrocatalysts for oxygen reduction in both alkaline and acidic media. *Carbon N. Y.* **137**, 93–103 (2018).

87. Zhou, H. *et al.* A self-template and KOH activation co-coupling strategy to synthesize ultrahigh surface area nitrogen-doped porous graphene for oxygen reduction. *RSC Adv.* **6**, 73292–73300 (2016).

88. Srinu, A., Peera, S. G., Parthiban, V., Bhuvaneshwari, B. & Sahu, A. K. Heteroatom Engineering and Co–Doping of N and P to Porous Carbon Derived from Spent Coffee Grounds as an Efficient Electrocatalyst for Oxygen Reduction Reactions in Alkaline Medium. *ChemistrySelect* **3**, 690–702 (2018).

89. Amiinu, I. S. *et al.* Self-Organized 3D Porous Graphene Dual-Doped with Biomass-Sponsored Nitrogen and Sulfur for Oxygen Reduction and Evolution. *ACS Appl. Mater. Interfaces* **8**, 29408–29418 (2016).

90. Amiinu, I. S. *et al.* Self-Organized 3D Porous Graphene Dual-Doped with Biomass-Sponsored Nitrogen and Sulfur for Oxygen Reduction and Evolution. *ACS Appl. Mater. Interfaces* **8**, 15181–15190 (2016).

91. Kim, M. J. *et al.* Biomass-Derived Air Cathode Materials: Pore-Controlled S,N-Co-doped Carbon for Fuel Cells and Metal-Air Batteries. *ACS Catal.* **9**, 3389–3398 (2019).

92. Jäger, R. *et al.* Synthesis and characterization of cobalt and nitrogen co-doped peat-derived carbon catalysts for oxygen reduction in acidic media. *Catalysts* **11**, (2021).

93. Liu, L. *et al.* N-doped porous carbon nanosheets as pH-universal ORR

electrocatalyst in various fuel cell devices. *Nano Energy* **49**, 393–402 (2018).

94. Xing, T. *et al.* Ball milling: A green mechanochemical approach for synthesis of nitrogen doped carbon nanoparticles. *Nanoscale* **5**, 7970–7976 (2013).

95. Takacs, L. & McHenry, J. S. Temperature of the milling balls in shaker and planetary mills. *J. Mater. Sci.* **41**, 5246–5249 (2006).

96. Zhang, E. *et al.* Nanocasting in ball mills - Combining ultra-hydrophilicity and ordered mesoporosity in carbon materials. *J. Mater. Chem. A* **6**, 859–865 (2018).

97. Song, Q. S., Chiu, C. H. & Chan, S. L. I. Effects of ball milling on the physical and electrochemical characteristics of nickel hydroxide powder. *J. Appl. Electrochem.* **36**, 97–103 (2006).

98. Zhang, S., Zhang, H., Hua, X. & Chen, S. Tailoring molecular architectures of Fe phthalocyanine on nanocarbon supports for high oxygen reduction performance. *J. Mater. Chem. A* **3**, 10013–10019 (2015).

99. Rajendiran, R. *et al.* Mechanochemical assisted synthesis of heteroatoms inherited highly porous carbon from biomass for electrochemical capacitor and oxygen reduction reaction electrocatalysis. *Electrochim. Acta* **317**, 1–9 (2019).

100. Costa de Oliveira, M. A., Machado Pico, P. P., Freitas, W. da S., D'Epifanio, A. & Mecheri, B. Iron-based electrocatalysts for energy conversion: Effect of ball milling on oxygen reduction activity. *Appl. Sci.* **10**, (2020).

101. Ratso, S. *et al.* Effect of ball-milling on the oxygen reduction reaction activity of iron and nitrogen co-doped carbide-derived carbon catalysts in acid media. *ACS Appl. Energy Mater.* **2**, 7952–7962 (2019).

102. Proietti, E. & Dodelet, J.-P. Ballmilling of Carbon Supports to Enhance the Performance of Fe-based Electrocatalysts for Oxygen Reduction in PEM Fuel Cells. *ECS Trans.* **16**, 393–404 (2008).

103. Noori, A. *et al.* Development of pressure-responsive polypropylene and biochar-based materials. *Micromachines* **11**, 1–12 (2020).

104. Giorcelli, M. *et al.* High-Temperature Annealed Biochar as a Conductive Filler for the Production of Piezoresistive Materials for Energy Conversion Application. *ACS Appl. Electron. Mater.* **3**, 838–844 (2021).

105. Tagliaferro, A., Rovere, M., Padovano, E., Bartoli, M. & Giorcelli, M. Introducing the novel mixed gaussian-lorentzian lineshape in the analysis of the raman signal of biochar. *Nanomaterials* **10**, 1–19 (2020).

106. Elgrishi, N. *et al.* A Practical Beginner's Guide to Cyclic Voltammetry. *J. Chem. Educ.* **95**, 197–206 (2018).

107. Mayall, R. M. & Birss, V. I. in a Mass Transport Controlled System. 53–56 (2018).

108. Wu, G., More, K. L., Johnston, C. M. & Zelenay, P. High-Performance Electrocatalysts for Oxygen Reduction Derived from Polyaniline, Iron, and Cobalt. 443–448 (2011).

109. Osmieri, L., Escudero-Cid, R., Monteverde Videla, A. H. A., Ocón, P. & Specchia, S. Performance of a Fe-N-C catalyst for the oxygen reduction reaction in direct methanol fuel cell: Cathode formulation optimization and short-term durability. *Appl. Catal. B Environ.* **201**, 253–265 (2017).

110. Osmieri, L. *et al.* Effects of using two transition metals in the synthesis of non-noble electrocatalysts for oxygen reduction reaction in direct methanol fuel cell. *Electrochim. Acta* **266**, 220–232 (2018).

111. Garsany, Y., Baturina, O. A., Swider-Lyons, K. E. & Kocha, S. S. Experimental methods for quantifying the activity of platinum electrocatalysts for the oxygen reduction reaction. *Anal. Chem.* **82**, 6321–6328 (2010).

112. Guerrini, E., Grattieri, M., Faggianelli, A., Cristiani, P. & Trasatti, S. PTFE effect on the electrocatalysis of the oxygen reduction reaction in membraneless microbial fuel cells. *Bioelectrochemistry* **106**, 240–247 (2015).

113. Wu, Y. C., Feng, D. & Koch, W. F. Evaluation of liquid junction potentials and determination of pH values of strong acids at moderate ionic strengths. *J. Solution Chem.* **18**, 641–649 (1989).

114. Ohma, A., Shinohara, K., Iiyama, A., Yoshida, T. & Daimaru, A. Membrane and Catalyst Performance Targets for Automotive Fuel Cells by FCCJ Membrane, Catalyst, MEA WG. *ECS Trans.* **41**, 775–784 (2019).

115. Martinaiou, I. *et al.* Activity and degradation study of an Fe-N-C catalyst for ORR in Direct Methanol Fuel Cell (DMFC). *Appl. Catal. B Environ.* **262**, 118217 (2020).

116. Hermann, H., Schubert, T., Gruner, W. & Mattern, N. Structure and chemical reactivity of ball-milled graphite. *Nanostructured Mater.* **8**, 215–229 (1997).

117. Liu, Z. Y. *et al.* Effect of ball-milling time on mechanical properties of carbon nanotubes reinforced aluminum matrix composites. *Compos. Part A Appl. Sci. Manuf.* **43**, 2161–2168 (2012).

118. Eguchi, T., Kanamoto, Y., Tomioka, M., Tashima, D. & Kumagai, S. Effect of ball milling on the electrochemical performance of activated carbon with a very high specific surface area. *Batteries* **6**, (2020).

119. Zagal, J. H. *et al.* Towards a unified way of comparing the electrocatalytic activity MN4 macrocyclic metal catalysts for O2 reduction on the basis of the reversible potential of the reaction. *Electrochem. commun.* **41**, 24–26 (2014).

120. Alsudairi, A. *et al.* Resolving the Iron Phthalocyanine Redox Transitions for ORR Catalysis in Aqueous Media. *J. Phys. Chem. Lett.* **8**, 2881–2886 (2017).

121. Osmieri, L., Monteverde Videla, A. H. A. & Specchia, S. Activity of Co-N multi walled carbon nanotubes electrocatalysts for oxygen reduction reaction in acid conditions. *J. Power Sources* **278**, 296–307 (2015).

122. Kaur, P., Verma, G. & Sekhon, S. S. Biomass derived hierarchical porous carbon materials as oxygen reduction reaction electrocatalysts in fuel cells. *Prog. Mater. Sci.* **102**, 1–71 (2019).

123. Borghei, M., Lehtonen, J., Liu, L. & Rojas, O. J. Advanced Biomass-Derived Electrocatalysts for the Oxygen Reduction Reaction. *Adv. Mater.* **30**, 1–27 (2018).

124. Deng, J., Li, M. & Wang, Y. Biomass-derived carbon: Synthesis and applications in energy storage and conversion. *Green Chem.* **18**, 4824–4854 (2016).

125. Torsello, D. *et al.* Tuning the microwave electromagnetic properties of biochar-based composites by annealing. *Carbon Trends* **4**, 100062 (2021).

126. Savi, P., Yasir, M., Bartoli, M., Giorcelli, M. & Longo, M. Electrical and microwave characterization of thermal annealed sewage sludge derived biochar composites. *Appl. Sci.* **10**, (2020).

127. Bartoli, M. *et al.* Influence of pyrolytic thermal history on olive pruning biochar and related epoxy composites mechanical properties. *J. Compos. Mater.* **54**, 1863–1873 (2020).

128. Bartoli, M. *et al.* Shape tunability of carbonized cellulose nanocrystals. *SN Appl. Sci.* **1**, 1–15 (2019).

129. Tagliaferro, A., Rovere, M., Padovano, E., Bartoli, M. & Giorcelli, M. Introducing the novel mixed gaussian-lorentzian lineshape in the analysis of the raman signal of biochar. *Nanomaterials* **10**, 1–19 (2020).

130. Coleman, M., Gesch, R., Jaradat, A., Mitchell, R. & Reicosky, D. Biomass-Bioenergy Crops in the United States: A Changing Paradigm. *Am. J. Plant Sci. Biotechnol.* **1**, (2007).

131. Gao, Y., Yue, Q., Gao, B. & Li, A. Insight into activated carbon from different kinds of chemical activating agents: A review. *Sci. Total Environ.* **746**, 141094 (2020).

132. Bashkova, S. & Bandosz, T. J. The effects of urea modification and heat treatment on the process of NO2 removal by wood-based activated carbon. *J. Colloid Interface Sci.* **333**, 97–103 (2009).

133. Yang, X. *et al.* Ball-milled, solvent-free Sn-functionalisation of wood waste biochar for sugar conversion in food waste valorisation. *J. Clean. Prod.* **268**, 122300 (2020).

134. Sekirifa, M. L. *et al.* Preparation and characterization of an activated carbon from a date stones variety by physical activation with carbon dioxide. *J. Anal. Appl. Pyrolysis* **99**, 155–160 (2013).

135. Manoj, B. Investigation of nanocrystalline structure in selected carbonaceous materials. *Int. J. Miner. Metall. Mater.* **21**, 940–946 (2014).

136. Takagi, H., Maruyama, K., Yoshizawa, N., Yamada, Y. & Sato, Y. XRD analysis of carbon stacking structure in coal during heat treatment. *Fuel* **83**, 2427–2433 (2004).

137. Barnakov, C. N., Khokhlova, G. P., Popova, A. N., Sozinov, S. A. & Ismagilov, Z. R. XRD characterization of the structure of graphites and carbon materials obtained by the low-temperature graphitization of coal tar pitch. *Eurasian Chem. J.* **17**, 87–93 (2015).

138. Goya, G. F. Handling the particle size and distribution of Fe3O4 nanoparticles through ball milling. *Solid State Commun.* **130**, 783–787 (2004).

139. Guo, D. *et al.* Observation of Landau levels in potassium-intercalated graphite under a zero magnetic field. *Nat. Commun.* **3**, (2012).

140. Weiss, J., Zhang, H. & Zelenay, P. Recent progress in the durability of Fe-N-C oxygen reduction electrocatalysts for polymer electrolyte fuel cells. *J. Electroanal. Chem.* **875**, 114696 (2020).

141. Kumar, K. *et al.* Physical and Chemical Considerations for Improving Catalytic Activity and Stability of Non-Precious-Metal Oxygen Reduction Reaction Catalysts. *ACS Catal.* **8**, 11264–11276 (2018).

142. Sebastián, D. *et al.* Performance, methanol tolerance and stability of Fe-aminobenzimidazole derived catalyst for direct methanol fuel cells. *J. Power Sources* **319**, 235–246 (2016).

143. Osmieri, L. *et al.* Status and challenges for the application of platinum group metal-free catalysts in proton-exchange membrane fuel cells. *Curr. Opin. Electrochem.* **25**, 100627 (2021).

144. James Sherwood. The significance of biomass in a circular economy. *Bioresour. Technol.* **300**, 122755 (2020).

145. Specchia, S., Atanassov, P. & Zagal, J. H. Mapping transition metal–nitrogen–carbon catalyst performance on the critical descriptor diagram. *Curr. Opin. Electrochem.* **27**, 100687 (2021).

146. Zago, S. *et al.* Engineered biochar derived from pyrolyzed waste tea as a carbon support for Fe-N-C electrocatalysts for the oxygen reduction reaction. *Electrochim. Acta* 140128 (2022) doi:10.1016/j.electacta.2022.140128.